Doctral Thesis

Effects of diffractive dissociation on ultra-high energy cosmic rays and measurements of diffractive dissociation using ATLAS and LHCf detectors

Ken Ohashi

Graduate School of Science, Nagoya University

February, 2022

Abstract

Cosmic rays above 10^{18} eV, ultra-high energy cosmic rays or UHECRs, have been observed for more than 50 years. The origin of UHECRs, however, is still unknown. The species of UHECRs, the mass composition, as well as the energy spectrum are important information to understand the origin of UHECRs. These UHECRs are measured by observing particles produced in an air shower, cascade interaction caused by these UHECRs in the atmosphere. The mass composition is estimated by comparing measured mass-sensitive observable and predictions of these observable by simulations. For mass-sensitive observable, the depth of maximum of shower development, $X_{\rm max}$, and the number of muons at the ground, N_μ, are widely adopted. In measurements of mean of $X_{\rm max}$ by the Pierre Auger Observatory, systematic uncertainty in measurements for 10^{19} eV UHECRs is $^{+8.0}_{-7.6}$ g/cm^2. Meanwhile, predictions of the mean of $X_{\rm max}$ are different in approximate ± 14 g/cm^2 at the energy due to the difference among the hadronic interaction models adopted in the simulation. Thus, interpretation of mass composition is challenging due to uncertainty in hadronic interactions. Furthermore, uncertainty in hadronic interactions may be underestimated if it is estimated from the difference in predictions among hadronic interaction models.

Diffractive dissociation is one of the sources of uncertainty in hadronic interactions. To reduce uncertainty in diffractive dissociation, measurements by accelerator experiments are needed. There are several types of diffractive dissociation, *e.g.* single-diffractive dissociation (SD) and double-diffractive dissociation (DD). Diffractive dissociation is characterized by diffractive mass. Cross-sections of SD and DD were measured by many experiments, *e.g.* by the ALICE and CMS experiments at the Large Hadron Collider (LHC) at CERN. These cross-section measurements were performed for middle diffractive-mass events. Cross-sections for low diffractive-mass events were extrapolated using hadronic interaction models. Large experimental uncertainty was reported due to these extrapolations for low diffractive-mass events. Large effects of diffractive dissociation on $X_{\rm max}$ or N_μ were pointed out in several previous studies. However, the effects of SD, DD, and diffractive mass have been yet not separately estimated, whereas particles from SD and DD behave differently in air shower development. Moreover, definitions of SD and DD are not consistent between these estimations and experiments. It was challenging to consider uncertainty in $X_{\rm max}$ or N_μ propagated from the experimental uncertainty in measurements.

In this thesis, the effects of SD, DD, and diffractive mass for air shower development were estimated comprehensively. We found that only the fraction of diffractive dissociation in inelastic cross-sections shows a substantially large effect on the mean of $X_{\rm max}$, whereas fractions between SD and DD or diffractive mass show minor or negligible effects on $X_{\rm max}$ and N_μ. The sizes of uncertainty in the mean of $X_{\rm max}$ caused by experimental uncertainty in measurements of cross-sections of SD and DD by the ALICE and CMS experiments are found to be $^{+4.0}_{-5.6}$ g/cm^2 and $^{+1.7}_{-1.2}$ g/cm^2, respectively. The uncertainty from measurements

by the ALICE experiment is comparable to the dominant source of systematic uncertainty in X_{max} by the Pierre Auger Observatory. Therefore, the experimental uncertainty in cross-section measurements of diffractive dissociation is one of the dominant sources of the uncertainties in interpretations of mass composition. The uncertainty caused by these experimental uncertainties should be reduced to less than $\pm 3.0\ \mathrm{g/cm^2}$ to avoid effects on interpretations of mass composition.

The direct measurements of low diffractive-mass events are required to reduce these experimental uncertainties since this low diffractive-mass region could not be measured but extrapolated by hadronic interaction models. In particular, in measurements of the CMS experiment, this low diffractive-mass region was extrapolated using only one hadronic interaction model. In this thesis, energy spectra of very forward photons produced in SD were measured using detectors of the ATLAS and LHCf experiments. The validation of the hadronic interaction model adopted in the CMS experiment was performed. The validation using the measured photon spectra suggests that the systematic uncertainty quoted by the CMS experiment may be underestimated. Future measurements with much higher statistics by the ATLAS and LHCf experiments will reduce uncertainty in cross-section measurements of diffractive dissociation and interpretations of the mass composition.

Contents

Acknowledgments

I express my sincere thanks to my supervisor, Prof. Yoshitaka Itow, for giving me a chance to research this subject and for useful suggestions. I also express my sincere thanks to Prof. Hiroaki Menjo for discussions and suggestions on all aspects of my research. Without supports from Prof. Itow and Prof. Menjo, it would be impossible to complete my research.

I am grateful to all my collaborators. I am grateful to Prof. Takashi Sako and Dr. Katsuaki Kasahara for their discussions and helpful comments on my research, especially to studies using air shower simulations. I am grateful to members of the ATLAS-LHCf joint analysis team. In particular, I am grateful to Dr. Leszek Adamczyk for his contributions to analyses of data taken by detectors of the ATLAS experiment. His analyses were essential to complete the analysis in the analysis team. I would like to thank all members of the LHCf collaboration for discussions and comments.

I would like to thank Felix Riehn for his useful comments and discussions. The comments given during his stay in Nagoya, in the conferences, and via e-mails helped me to understand hadronic interactions. I would like to thank all members of the Cosmic-ray laboratory for discussions and comments in the daily life in the laboratory. Finally, I would like to express my sincere thanks to my family for their supports and encouragement in all aspects of my life.

Chapter 1

Introduction

1.1 Ultra-high energy cosmic rays

1.1.1 Ultra-high energy cosmic rays and their origin

Cosmic-rays with energy above 10^{18} eV, ultra-high energy cosmic-rays or UHECRs, have been observed for more than 50 years since the Volcano Ranch experiment was reported a cosmic-ray with energy more than 10^{20} eV [1, 2]. However, the origin of UHECRs is still unknown. Measurements of the energy spectrum and the particle type, mass composition, of UHECRs have been performed to understand the origin.

The energy spectrum of these cosmic rays has been observed as illustrated in Fig. 1.1 [3, 4, 5, 6]. Since the spectrum of cosmic rays decreases with energy steeply, the spectrum was multiplied by E^3 for a better understanding of the structure in the spectrum. Several features in the spectrum were found; the spectrum becomes harder around $10^{18.7}$ eV and steeply decreases above $10^{19.5}$ eV. The feature at $10^{19.5}$ eV can be caused by the maximum energy of the acceleration at one source. The feature at $10^{18.7}$ eV can be caused by the change of the source of UHECRs at that energy. Other interpretations are, however, possible by considering interactions during propagations from the source to the Earth affect the spectrum. In propagations from the source to the Earth, a UHECR proton interacts with cosmic-microwave background photons, $\gamma_{\rm CMB}$, via pair creations, $p + \gamma_{\rm CMB} \to e^+ + e^- + p$, and pion productions, $p + \gamma_{\rm CMB} \to \pi^0 + p$. A UHECR nucleus also interacts with $\gamma_{\rm CMB}$ and consequently, disintegration occurs; nucleons are produced in the nucleus-photon interaction. This effect known as Greisen-Zatsepin-Kuzmin effects [7, 8] can explain the structure above $10^{19.5}$ eV in the spectrum by assuming all UHECRs as protons. The mass composition is important to understand the structure of the spectrum due to the acceleration mechanism at the source or propagations.

Several scenarios for the origin of UHECRs are proposed to explain the spectrum and the mass composition. Figure 1.2 illustrates predictions of the mean of $\ln A$, $\langle \ln A \rangle$, where A is the mass number of UHECRs nucleus, by several theoretical scenarios as discussed in Ref. [9] and its references. The mixed large $E_{\rm max}$ scenario [10] illustrated in dashed line in Fig. 1.2 considers mixed composition with protons and nuclei. The maximum energy at the source is assumed as $E_{\rm max} = Z \times 10^{20.5}$ eV, where Z is the charge of cosmic-ray particles. By considering propagations, $\langle \ln A \rangle$ becomes smaller as energy becomes larger to explain the energy spectrum. In interactions between a proton and $\gamma_{\rm CMB}$, secondary protons with

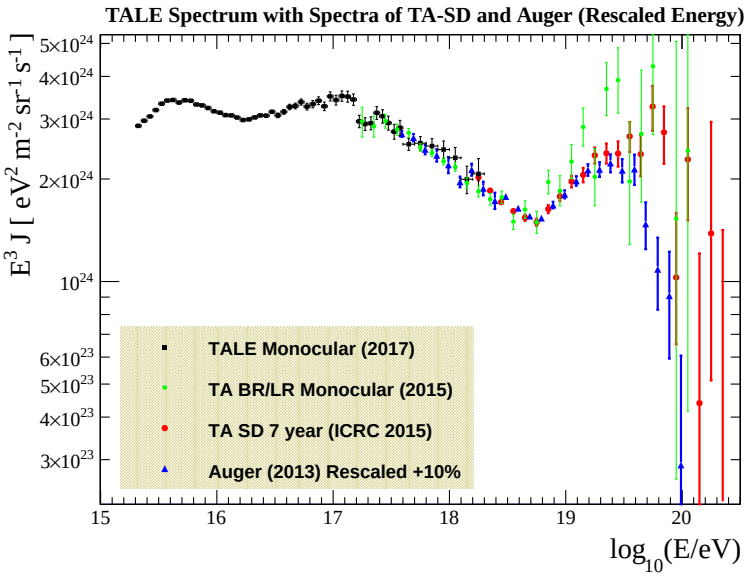

Fig. 1.1: The energy spectrum of cosmic rays above $10^{15.3}$ eV measured by TALE [3], surface and fluorescence detectors of the Telescope Array experiment [4, 5], and Pierre Auger Observatory [6]. The figure reproduced by permission of the AAS from Ref. [3].

smaller energy are produced. The structure of the spectrum around $10^{19.5}$ eV is explained by these protons. The mixed small $E_{\rm max}$ scenario [11] illustrated in blue open circles in Fig. 1.2 considers the mixed composition and the maximum energy $E_{\rm max} = Z \times 4 \times 10^{18}$ eV at the source. Since the maximum proton energy is smaller than 10^{19} eV, $\langle \ln A \rangle$ becomes larger as energy becomes larger. The structure of the spectrum around $10^{19.5}$ eV is explained by the maximum energy at the source. Several scenarios consider particular astronomical objects. For example, in Ref. [12], the spectrum and the composition are predicted by assuming two sources: galactic supernova remnants (SNR) as sources of cosmic-rays up to 10^{17} eV and active galactic nuclei (AGN) as sources of UHRCRs. The prediction is illustrated by black open squares in Fig. 1.2. The mixed composition with $E_{\rm max} \approx Z \times 10^{20}$ eV is considered, whereas the composition at the source depends on the position of the shock front, where cosmic-rays are accelerated. The mass composition can constrain scenarios for the origin of UHECRs.

1.1.2 Measurements of ultra-high energy cosmic rays

The flux of these UHECRs is by far smaller than one per m^2 per year. It is difficult to measure them directly by satellites. Instead, these UHECRs have been measured using a particle cascade shower induced by UHECRs, air shower, to increase the effective area of measurements. In the atmosphere, a cosmic-ray particle interacts with an air nucleus. For high energy cosmic-rays, nucleons, neutral pions, and charged pions are produced in the collision. A neutral pion decays into two gamma-rays, and produces two electromagnetic cascade showers; an electron and a positron are produced via pair creation from a gamma-ray. The electron or the positron emits gamma-ray(s) via bremsstrahlung. These interactions happen repeatedly. Many electrons and positrons are produced. The development of the electromagnetic cascade showers stops when the energy of electrons and positrons becomes small and the

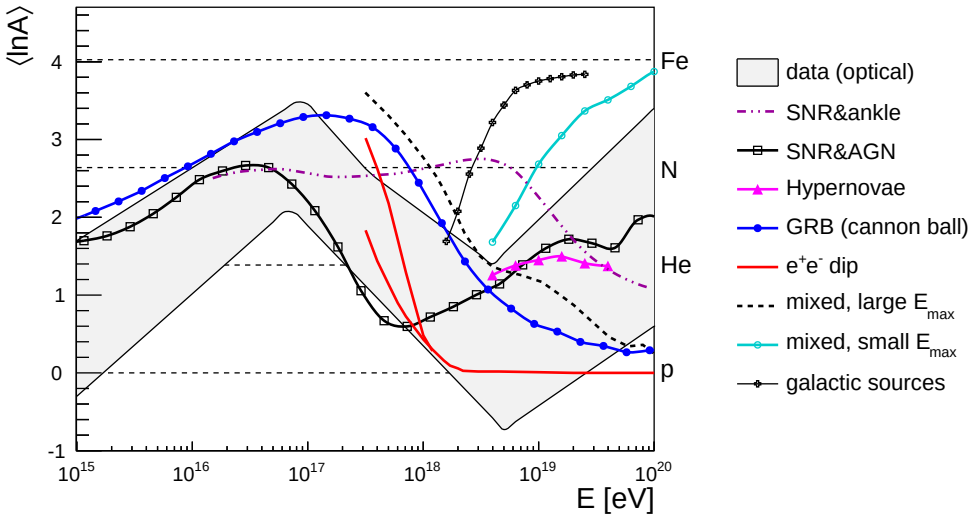

Fig. 1.2: Predictions of $\langle \ln A \rangle$ for some scenarios [9]. Mixed large $E_{\max}$ scenario [10], mixed small $E_{\max}$ [11] scenario, and SNR and AGN [12] scenario are illustrated in dashed line, blue open circles, and black open squares. Reprinted from [9], with permission from Elsevier.

ionization loss becomes dominant than bremsstrahlung. The number of particles in the cascade shower becomes maximum when development stops. Meanwhile, charged pions and nucleons make interactions with air nuclei repeatedly and produce nucleons, neutral pions, and charged pions. A neutral pion decays into two gamma-rays and another electromagnetic cascade shower starts. Charged pions and nucleons make interactions repeatedly. After these cascade interactions, many low-energy charged pions are produced and decay into muons. This cascade shower induced by a cosmic-ray is called an extensive air shower or an air shower. Electrons, positrons, and gamma-rays are dominant components of an air shower. On the ground, particles produced in an air shower spread in the wide area. We can measure UHECRs by detecting part of these particles or the fluorescence lights emitted from charged particles in an air shower.

These UHECRs have been observed by the Telescope Array (TA) experiment [13, 14] at the northern hemisphere since 2007 and by the Pierre Auger Observatory (PAO) [15] at the southern hemisphere since 2004 using the air shower method. These experiments employ two detection methods: surface detector arrays, which measure particles produced in an air shower at the ground, and fluorescence telescopes, which measure fluorescence lights emitted from charged particles in an air shower. In PAO, 24 fluorescence telescopes and 1660 particle detectors with a 3.6 m diameter were installed, each of which covers approximately 3000 km^2. Energy, arrival directions, and mass-sensitive observables of UHECRs are measured using these detectors. For mass-sensitive observables, the depth of maximum of air shower development, $X_{\max}$, and the number of muons on the ground, N_μ, are widely adopted. $X_{\max}$ and N_μ depend on the mass number of the primary cosmic-rays. $X_{\max}$ is defined by the depth along the initial cosmic-ray direction that the number of particles in an air shower becomes maximum.

Mass composition is interpreted by comparing $X_{\max}$ or N_μ measured by experiments and those predicted by the air shower simulations. Figure 1.3 shows mean and fluctuations of $X_{\max}$, $\langle X_{\max} \rangle$ and $\sigma(X_{\max})$, measured by Pierre Auger Observatory [16]. Red lines and blue lines represent predictions of simulations with proton and iron for primary cosmic-

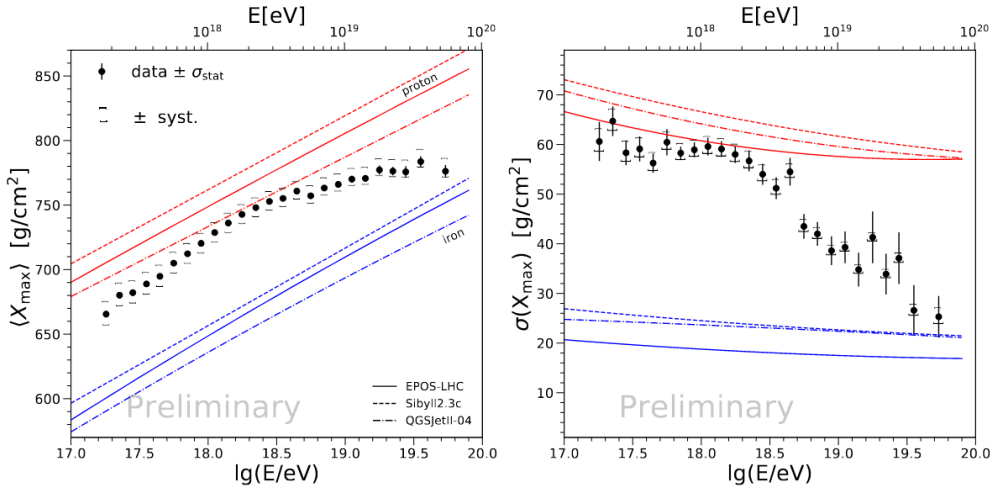

Fig. 1.3: Mean and fluctuations of depth of maximum of air shower development measured by Pierre Auger Observatory [16] and its predictions for proton primary (red lines) and iron primary (blue lines) by three post-LHC hadronic interaction models: EPOS-LHC [17] (solid line), QGSJET II-04 [18] (dashed line), and SIBYLL 2.3c [19] (dotted line). The figure is taken from Ref. [16].

rays, respectively. Predictions with iron primaries show much larger $\langle X_{\rm max} \rangle$ and smaller $\sigma(X_{\rm max})$ than those with proton primaries. This feature means that we can understand the mass composition if $\langle X_{\rm max} \rangle$ and $\sigma(X_{\rm max})$ are measured by experiments and predicted by simulations with good precision. Predictions by the simulation, however, depend on calculations of hadronic interactions by hadronic interaction models adopted in the simulation. In Fig. 1.3, solid, dashed, and dotted lines corresponds to predictions by three hadronic interaction models, EPOS-LHC [17], QGSJET II-04 [18], and SIBYLL 2.3c [19], respectively. Differences due to hadronic interaction models are 20-30 $\mathrm{g/cm^2}$ and 30-40 $\mathrm{g/cm^2}$ in $\langle X_{\rm max} \rangle$ for 10^{17} eV and 10^{19} eV proton primaries, respectively. These sizes of differences approximately correspond to 1.0 in the mean of $\ln A$, $\langle \ln A \rangle$. Meanwhile, systematic uncertainty in the measurements by PAO is $^{+8.0}_{-7.6}$ $\mathrm{g/cm^2}$ [20] and much smaller than the differences in predictions among hadronic interaction models. The dominant sources of the systematic uncertainty in measurements by PAO are the reconstruction of $X_{\rm max}$ and the effects of propagations of fluorescence lights in the atmosphere. They can be improved in the future. In consequence, it is challenging to interpret the mass composition of primary cosmic-rays even after improvements of measurements due to uncertainty of hadronic interactions.

Interpretations of mass composition from N_μ have another problem. Figure 1.4 illustrates the average muon number measured by PAO [22]. The results are larger than predictions of the iron primary, which suggests heavier composition than iron. However, a nucleus heavier than iron is very rare in the Universe. Moreover, interpretations of mass composition from $X_{\rm max}$ and N_μ should be consistent since UHECRs from the same sky are measured for both cases. Therefore, this result suggests that N_μ calculated in the simulation is too small. This problem is called the muon deficit problem and is confirmed by many experiments [23].

Even though differences in predictions of $X_{\rm max}$ or N_μ among hadronic interaction models are considered in interpretations of mass compositions, the uncertainty of hadronic interac-

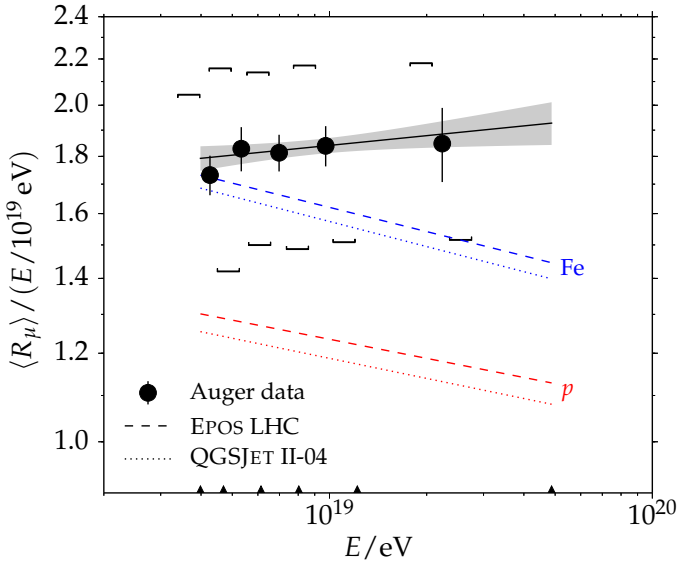

Fig. 1.4: The average muon number relative to QGSJET II-03 [21] predictions of the proton-induced air shower measured by Pierre Auger Observatory [22]. Predictions for the proton and the iron primary are shown in red and blue lines, respectively. Dotted and dashed lines correspond to predictions by QGSJET II-04 [18] and EPOS-LHC [17], respectively. Reprinted figure with permission from [A. Aab *et al.* (Pierre Auger Collaboration), Phys. Rev. D 91, 031003, 2015.] Copyright 2015 by the American Physical Society. [22].

tions can be larger than the differences. Since hadronic interaction models are based on phenomenological models and tuned using the results of accelerator experiments as discussed below, it is difficult to calculate the uncertainty of hadronic interactions theoretically. Therefore, the uncertainty of hadronic interactions should be considered based on uncertainty in measurements of accelerator experiments.

1.2 Interpretations of mass-composition and hadronic interaction models

The hadronic interactions are dominant sources of uncertainty in predictions of X_{max} or N_μ in simulation, and therefore, dominant sources of the uncertainty in interpretations of the mass composition. Calculations of interactions for gamma-rays, electrons, and positrons are well established in Quantum Electrodynamics. By contrast, calculations for hadrons are difficult; Quantum Chromodynamics (QCD) is the theory for hadronic interactions, whereas it is difficult to calculate hadronic interactions with low momentum transfer cases from the first principle in the theory. In the simulation, we utilize hadronic interaction models based on phenomenological models tuned by results in accelerator experiments. Although hadronic interaction models are tuned by available experimental results, large uncertainty exists in the calculation using these models.

Calculations in hadronic interaction models can be divided into several parts based on collision types. One is the calculation for the collision with (an) interaction(s) with high momentum transfers between a constituent of each colliding hadron. Calculations based on

perturbative QCD work well for the interaction between constituents, even though it is difficult to calculate all the collisions. Phenomenological models are also adopted for part of the calculation. The other is the calculation for the collision without interaction with high momentum transfers. In the collision, we cannot apply perturbative QCD for the calculation. Phenomenological models based on the Regge Theory are widely adopted for the collision. Diffractive scattering is one of the collision types calculated in this way. Diffractive dissociation, a collision type similar to diffractive scattering but with particle productions from the breakup of (a) scattered particle(s), is the other collision type. Since each type is calculated by different phenomenological models in the hadronic interaction models, it is important to improve calculations for each collision type separately.

Improvements in predictions of hadronic interactions using accelerator experiments are necessary since phenomenological models should be tuned using the results of accelerator experiments. Following things are needed for improvements of hadronic interactions: (i) clear understandings of effects of each collision type in hadronic interactions on $X_{\rm max}$ or N_μ and (ii) measurements of each collision type using accelerator experiments. An effect of each collision type on $X_{\rm max}$ or N_μ varies. Some features in a collision type may show large effects on $X_{\rm max}$ or N_μ, whereas the other features in a collision type may show small or negligible effects. All features in each collision type that show large effects are needed to be measured by accelerator experiments. Thus, quantitative estimations of effects are necessary to understand what should be measured.

The center-of-mass energy of a collision between a UHRCR particle and an air nucleus is much larger than the energy of accelerators on the Earth. Therefore, measurements at the highest energy collider, the Large Hadron Collider (LHC) at CERN, is important. The energy of LHC corresponds to the energy of a collision between a 10^{17} eV cosmic-ray proton and an air nucleus. Since large uncertainty in predictions of $X_{\rm max}$ and N_μ are found even for 10^{17} eV cosmic rays, measurements at LHC are highly important.

The challenge of the improvements of hadronic interaction models is owing to the following reasons;

a) Effects of particular processes in the hadronic interaction on $X_{\rm max}$ or N_μ are not simple. To understand the effect of each particular process, a careful study using air shower simulations is necessary. The understanding of effects tells us what particular process should be measured by accelerator experiments.

b) It is known that particles produced in regions with very small scattering angles in collider experiments, forward regions, are important for air shower predictions, whereas it is challenging to measure all particles produced in these regions in collider experiments. As discussed in Ref. [24], by considering the interaction between an initial cosmic-ray and an air nucleus, the forward particles, particles produced in forward regions, of the interaction and cascade showers initiated from these forward particles produces most particles in an air shower. Predictions of the forward particles are important. To measure these forward particles in the experiment, forward detectors in the collider experiments are important. However, due to configurations of beam pipes at colliding points and magnets in each collider, measurements using these detectors are limited.

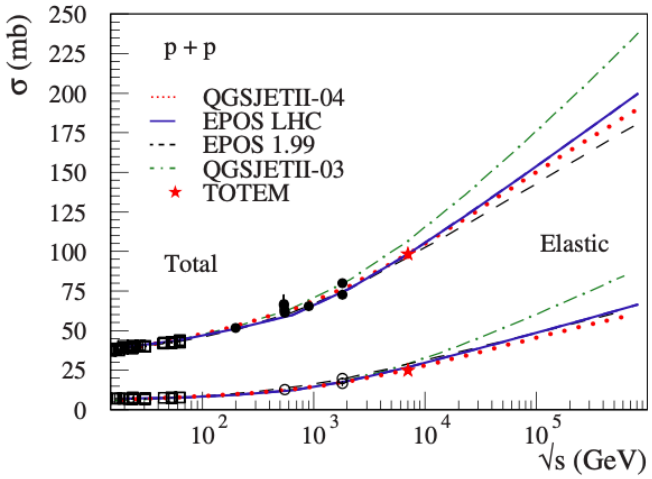

Fig. 1.5: Predictions of total and elastic cross-sections and experimental data for proton-proton collisions [25]. The figure is taken from Ref. [25]

1.3 Improvements of hadronic interaction models and diffractive dissociation

1.3.1 Improvements of hadronic interaction models using the early results at LHC

Improvements of hadronic interaction models were performed using the early results at LHC as discussed in Ref. [25]. Figure 1.5 illustrates total and elastic cross-sections measured by the TOTEM experiment [26] at LHC (red star) and its predictions by EPOS 1.99 (gray dashed) [27], EPOS-LHC (blue solid) [17], QGSJET II-03 (green dash-dotted) [21], and QGSJET II-04 (red dotted) [18]. Here, QGSJET II-03 and EPOS 1.99 are models before tuning (pre-LHC models) and QGSJET II-04 and EPOS-LHC are models after tuning (post-LHC models). Post-LHC models were tuned using measurements at LHC, thus differences of predictions between post-LHC models were much smaller than those between pre-LHC models. The tuning was also performed for the number of charged particles using the number density of charged particles measured by the CMS experiment [28]. The tuning focusing on the number of charged particles mainly affected inelastic collisions except for diffractive dissociation.

Tuning of diffractive dissociation was performed using measurements of cross-sections for these collisions by the ALICE and the CMS experiments [29, 30]. For example, a hadronic interaction model, SIBYLL 2.3 [31], was tuned to show agreements with the ALICE results. Figure 1.6 illustrates calculations by SIBYLL 2.3 and experimental results used for tuning. Solid, dashed, dot-dashed lines were calculated results by SIBYLL 2.3 with three different criteria in calculations. The solid line was the same criteria with experimental results shown in the plot. (Details are given in Sec. 3.2.) The results of the ALICE experiment were illustrated in red open squares and circles [30]. The other markers correspond to relatively low energy results for proton-proton and proton-antiproton collisions. Large errors were found for these experimental results. For diffractive dissociation, tuning was performed even though very large experimental uncertainty exists in experimental results.

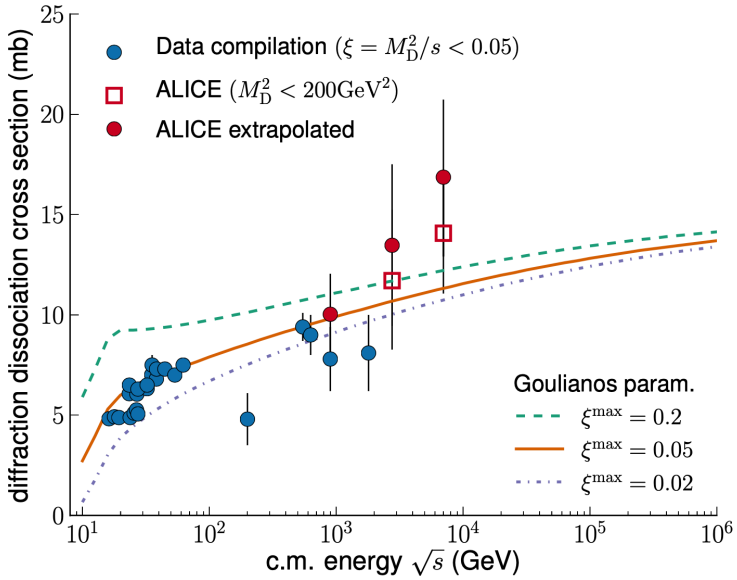

Fig. 1.6: The single-diffractive cross-section calculated by SIBYLL 2.3. Three different criteria in calculations are shown in dash, solid, and dot-dashed lines. Experimental results are also shown in Markers [30, 32]. The figure is taken from Ref. [31] with permission by the author.

The tuning using measurements at LHC reduced uncertainty in hadronic interaction models. Large differences in $X_{\max}$ were, however, observed even for post-LHC models as illustrated in Fig. 1.3.

1.3.2 Prospects of improvements

For future improvements of hadronic interaction models, the following three things are important: tuning of these models using the latest data from the experiments, new measurements for cases where no data is available, and improvements of measurements with large experimental uncertainty. Recently, several measurements have been performed for forward regions, *e.g.* by the LHC forward (LHCf) experiment [33, 34]. Moreover, measurements of collisions between a proton and an Oxygen ion are planned at LHC [35]. The proton-Oxygen collisions exactly correspond to the collisions in the air shower. Improvements in hadronic interaction models are expected because of these latest results and future results. However, large experimental uncertainty in measurements exists in the results for diffractive dissociation. The large uncertainty in measurements can cause large uncertainty in predictions of $X_{\max}$ or N_μ.

1.3.3 Diffractive dissociation

Diffractive dissociation is the collision with diffractive scattering and the breakup of (a) scattered particle(s) after the scattering. In the collision, the scattered particle dissociates, *i.e.* the scattered particle becomes excited and then dissociates into several particles. In diffractive dissociation, two hadrons interact with each other with low momentum transfer. Diffractive dissociation has several types; one is that one of the colliding particles dissociates. The other is that both of the colliding particles dissociate. In an air shower, a projectile

cosmic-ray is sometimes intact after diffractive dissociation, whereas particles are produced from the dissociation of an air nucleus. Since most particles produced in the forward regions in diffractive dissociation, it shows large effects on the air shower.

The previous studies discussed the effects of diffractive dissociation. In Ref. [36], effects of uncertainty in experiments were discussed using two additional tunes of QGSJET II-04, where the model was tuned to have better agreements with results by the ATLAS [37] and the CMS [29] experiments or with that by the TOTEM [38] experiment. From differences of two tunes, effects of different tuning for diffractive dissociation were estimated to be $10\,\mathrm{g/cm^2}$ on $\langle X_{\mathrm{max}} \rangle$. Effects of diffractive dissociation were also discussed in Ref. [39] with an extreme assumption, turning all the diffractive dissociation off in air shower simulations. The effect on $\langle X_{\mathrm{max}} \rangle$ for 10^{20} eV proton primary was estimated to be $15\,\mathrm{g/cm^2}$. Effects of diffractive dissociation on muon density on the ground were also pointed out.

Although these studies showed large effects of diffractive dissociation on X_{max} or N_μ and measurements of diffractive dissociation were performed, there are several problems. The first one is that the effects of each type in diffractive dissociation are unclear. For example, in the study in Ref. [36], effects were studied by several additional tunes of QGSJET II-04. The tuning, however, affects both diffractive dissociation and inelastic cross-sections. Therefore, the size of effects for each feature in diffractive dissociation is unclear in the previous studies. The second one is that the effects of large experimental uncertainty in diffractive dissociation on X_{max} or N_μ is unclear despite discussions in previous studies. Definitions for diffractive dissociation were based on the hadronic interaction models in these simulation studies. Meanwhile, definitions in experimental results depend on the configurations of detectors in each experiment. Due to the differences in definitions, it is impossible to calculate the effects of large experimental uncertainty on X_{max} or N_μ. The third one is that measurements of particular cases of diffractive dissociation, *i.e.* low diffractive-mass cases as discussed in Sec. 3.3.5, are very hard. That makes experimental uncertainty large.

1.4 Aim and structure of this thesis

In this thesis, we aim for solving the problem in interpretations of the mass composition of UHECRs. As the important step for solving the problem, we focus on one of the important sources of uncertainty in X_{max} or N_μ, diffractive dissociation. To solve three problems of diffractive dissociation discussed in the previous section, we discuss the effects of collision types and characteristics of diffractive dissociation on X_{max} or N_μ comprehensively. Moreover, uncertainty in predictions of X_{max} or N_μ is estimated from the uncertainty in cross-section measurements of diffractive dissociation. Additionally, the measurements using ATLAS and LHCf detectors are discussed to reduce experimental uncertainty in measurements.

The structure of this thesis is as follows; the air shower and hadronic interactions are introduced in Chapters 2 and 3, respectively. Effects of diffractive dissociation on X_{max} and N_μ are discussed comprehensively in Chapter 4. Uncertainty of $\langle X_{\mathrm{max}} \rangle$ from experimental uncertainty is discussed in Chapter 5. Measurements of diffractive dissociation with detectors of ATLAS and LHCf experiments are discussed in Chapters 6 and 7. We conclude in Chapter 8.

Chapter 2

Air shower

2.1 Simplified air shower model: Heitler model

Since an air shower consists of electromagnetic and hadronic cascade interactions, $X_{\max}$ or N_μ depends on the characteristics of each interaction. The understanding of the effects of an interaction on $X_{\max}$ or N_μ is important to understand what should be measured in accelerator experiments for the improvements of hadronic interaction models. In this section, we introduce a very simplified model for the air shower, developed by Heitler as reviewed in Ref. [40, 41] and extended by Matthews [42]. This model works well for qualitative understanding of the relation. Discussion based on simulations in previous studies follows after this section.

First, we focus on an electromagnetic shower initiated by a gamma-ray with energy E_0. In this simplified model, a gamma-ray makes an interaction after running a radiation length λ_e, which is the length that the energy of high energy electrons decreases to $1/e$ of the initial energy, and produces an electron and a positron by the pair creation. The electron and the positron make interactions after running λ_e and produce a gamma-ray by bremsstrahlung as illustrated in the left plot of Fig. 2.1. The number of particles after n-th interactions is $N = 2^n$. If we assume the same energy for each produced particle for simplicity, the energy of each particle is $E = E_0/2^n$. The development of electromagnetic shower stops when the energy of each particle becomes smaller than the critical energy $E^c_{e.m.}$, the energy that ionization loss of electrons and positrons becomes dominant than bremsstrahlung. The critical energy $E^c_{e.m.}$ of the air is roughly equal to 80 MeV [41]. The number of particles in electromagnetic showers becomes maximum after $n^{\rm MAX}$-th interactions, where $E^c_{e.m.} = E_0/2^{n^{\rm MAX}}$. Thus, $n^{\rm MAX} = \log_2 E_0/E^c_{e.m.}$. The depth of maximum of particles in electromagnetic showers, $X^{\rm EM}_{\max}$, corresponds to the depth at the $n^{\rm MAX}$-th interaction calculated as

$$X^{\rm EM}_{\max} = \lambda_e \log_2 E_0/E^c_{e.m.}. \tag{2.1}$$

Second, we focus on a cascade shower initiated by a hadron as illustrated in the right plot of Fig. 2.1. In a hadronic interaction, many charged pions and neutral pions are produced. A neutral pion decays into two gamma rays and produces electromagnetic cascade showers. Charged pions make interactions after running one interaction length λ_I, the mean length that a hadron travels before it makes an inelastic collision. As the energy of a charged pion becomes smaller, decay length λ_{decay}, the mean length that the particle travels before it decays, becomes smaller. Once λ_{decay} becomes comparable with λ_I, decay of a charged pion

becomes dominant. Note that this λ_I depends on the inelastic cross-section of the collisions. This dependency is, however, ignored in this model. For simplicity, we assume all the particles produced in a collision are either charged or neutral pions, having the same energy. In this case, the energy and the number of gamma-rays produced in the first interaction are

$$E_\gamma = \frac{E_0}{2n_{\rm mult}}, \tag{2.2}$$

and

$$N_\gamma = rn_{\rm mult}, \tag{2.3}$$

where r is the fraction of neutral pions in produced particles, E_0 is the energy of the primary cosmic ray, and $n_{\rm mult}$ is multiplicity, the number of particles produced in the interaction. Charged pions produced in the interaction make hadronic interactions with air nuclei repeatedly. After n-times of hadronic interactions, the number of charged pions and its energy are calculated as,

$$N_{\pi^\pm} = ((1-r)n_{\rm mult})^n, \tag{2.4}$$

$$E_{\pi^\pm} = \frac{E_0}{n_{\rm mult}^n}. \tag{2.5}$$

Development of hadronic showers stops at the critical energy E_π^c, the energy where $\lambda_{decay} = \lambda_I$. When development stops, muons are produced by the decays of charged pions. These muons are detected on the ground. The number of interaction when development stops, $n_{had}^{\rm MAX}$, is

$$n_{had}^{\rm MAX} = \frac{\ln E_0/E_\pi^c}{\ln n_{\rm mult}}, \tag{2.6}$$

and the number of muons is

$$N_\mu = (\frac{E_0}{E_{had}^c})^\beta, \tag{2.7}$$

where $\beta = \frac{\ln rn_{\rm mult}}{\ln n_{\rm mult}}$. If electromagnetic showers produced from the first interaction are only considered, the depth of maximum of air shower development, $X_{\rm max}$, is calculated as,

$$X_{\rm max} = \lambda_I + \lambda_e \log_2 \frac{E_0}{2n_{\rm mult}E_{e.m.}^c}. \tag{2.8}$$

For simplicity, we have assumed the same energy for each produced particle. However, the particle produced from the remnant of a projectile particle typically carries a large portion of energy in hadronic interactions. The effect is considered in an extended model developed in Ref. [42]. Hereafter, we consider the case that one particle, a leading particle, carries a large part of the energy, $K_{\rm el}E_0$, where "elasticity" $K_{\rm el}$ is the ratio of the energy of the leading particle to the projectile cosmic ray. If we assume that all other particles produced in the interaction share the same portion of energy, the energy of gamma rays produced in the first interaction is calculated as,

$$E_\gamma = \frac{(1-K_{\rm el})E_0}{2n_{\rm mult}}. \tag{2.9}$$

$X_{\rm max}$ for these gamma rays is calculated as,

$$X_{\rm max} = \lambda_I + \lambda_e \log_2 \frac{(1-K_{\rm el})E_0}{2n_{\rm mult}E_{e.m.}^c}. \tag{2.10}$$

If we consider the gamma rays produced in the interaction caused by the leading particle produced in the first interaction, the energy of the incident leading particle is

$$E_{\rm leading} = K_{\rm el} E_0. \tag{2.11}$$

$X_{\rm max}$ for this case is calculated using $2\lambda_I$ and $E_{\rm leading}$ instead of λ and E_0, respectively in Eq. (2.10).

$$X_{\rm max} = 2\lambda_I + \lambda_e \log_2 \frac{K_{\rm el}(1-K_{\rm el})E_0}{2n_{\rm mult}E^c_{e.m.}}. \tag{2.12}$$

The total energy of gamma rays produced in the first interaction and the interaction by the leading particle are $r(1-K_{\rm el})E_0$ and $rK_{\rm el}(1-K_{\rm el})E_0$, respectively. From Eqs. (2.10) and (2.12), $X_{\rm max}$ from each interaction becomes smaller when $K_{\rm el}$ becomes larger. However, $K_{\rm el}$ dependency of $X_{\rm max}$ is not simple; the total energy of gamma rays produced in the first interaction decrease as $K_{\rm el}$ becomes larger. Thus, the gamma-rays produced in the interaction of the leading particle or interactions after that interaction become more important. Actually, $X_{\rm max}$ becomes larger when $K_{\rm el}$ becomes larger.

2.1.1 Mass number dependency

$X_{\rm max}$ or N_μ depends on the mass of UHECRs. The mass dependency is explained by assuming the superposition of the nucleon in UHECRs. If a UHECR nucleus with the mass number A and the energy E_0 enters the atmosphere, we assume that the interaction between the UHECR nucleus and an air nucleus can be considered as A-times interactions between a nucleon and an air shower nucleus. In this case, A-times air showers induced by a nucleon with E_0/A are produced after the interaction. In the Heitler model without considering elasticity, $X_{\rm max}$ for the mass number A, $X^{\rm A}_{\rm max}$, is calculated from Eq. (2.8) as

$$X^{\rm A}_{\rm max} = \lambda^A_I + \lambda_e \log_2 \frac{E_0}{2An_{\rm mult}E^c_{e.m.}}. \tag{2.13}$$

Here, λ^A_I is the interaction length for the UHECR nucleus. λ^A_I is smaller than λ_I for protons since the cross-section for the UHECR nucleus is much larger than that for protons. Therefore, $X^{\rm A}_{\rm max}$ becomes smaller than $X_{\rm max}$ for protons.

N_μ for the mass number A, $N^{\rm A}_\mu$, is calculated from Eq. (2.7) as

$$N^{\rm A}_\mu = A^{1-\beta}(\frac{E_0}{E^c_{had}})^\beta. \tag{2.14}$$

Here, $\beta = \frac{\ln rn_{\rm mult}}{\ln n_{\rm mult}}$ is smaller than 1. Therefore, because of $A^{1-\beta} > 1$, $N^{\rm A}_\mu$ becomes larger than N_μ for a UHECR proton.

2.2 The relation between hadronic interactions and air shower development

The Heitler model and its extension tell us the relations between air shower development and characteristics of hadronic interactions. For example, small multiplicity and small inelastic

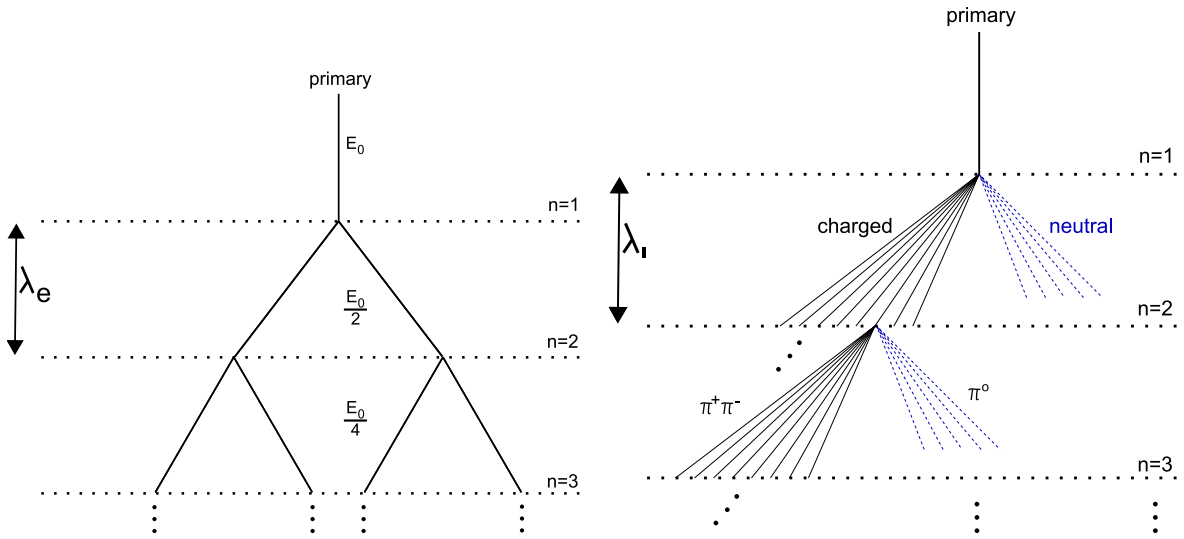

Fig. 2.1: Simplified schematic view of electromagnetic (left) and hadronic (right) cascade in the air shower [40, 41]. Reprinted figures with permission from [Ralf Ulrich, Ralph Engel, and Michael Unger, Phys. Rev. D 83, 054026, 2011.] Copyright 2011 by the American Physical Society. [41].

cross-section make $X_{\max}$ larger. However, this simple model is not true, because the energy of each particle does not necessarily share the same portion of energy. Moreover, the effect of elasticity is unclear in the simplified model. It is necessary to confirm these relations in the simulation.

The relation between each characteristic of hadronic interactions and $X_{\max}$ or N_μ were studied quantitatively using simulations in Ref. [41]. Figures 2.2 and 2.3 illustrated the impact of modification in characteristics of hadronic interactions on $X_{\max}$ and N_μ, respectively. In the study, cross-section, multiplicity, the ratio of charged particles in produced particles (charge ratio), and elasticity were focused as characteristics of hadronic interactions. The mean value of each characteristic was modified with the f_{19} parameter. If f_{19} is 1.5, the characteristic was modified to the 1.5 times larger value at 10^{19} eV. At the energy E, the characteristic was modified to $f(E, f_{19})$ times larger value. $f(E, f_{19})$ was defined as

$$f(E, f_{19}) = 1 + (f_{19} - 1)F(E). \tag{2.15}$$

Here, $F(E)$ was defined as

$$F(E) = \begin{cases} 0 & E \leq 1\mathrm{PeV} \\ \dfrac{\log_{10}(E/1\mathrm{PeV})}{\log_{10}(10\mathrm{EeV}/1\mathrm{PeV})} & E > 1\mathrm{PeV} \end{cases} \tag{2.16}$$

For $\langle X_{\max} \rangle$, cross-section, multiplicity, and elasticity show large effects as illustrated in Fig. 2.2. Large cross-section, large multiplicity, and small elasticity make $\langle X_{\max} \rangle$ smaller. Only the cross-section shows a large effect on $\sigma(X_{\max})$. Small multiplicity and large charge ratio make N_μ larger as illustrated in Fig. 2.3. For improvements of predictions of $\langle X_{\max} \rangle$ and N_μ, phenomenological models which affect these characteristics in hadronic interaction models should be validated and improved by accelerator experiments.

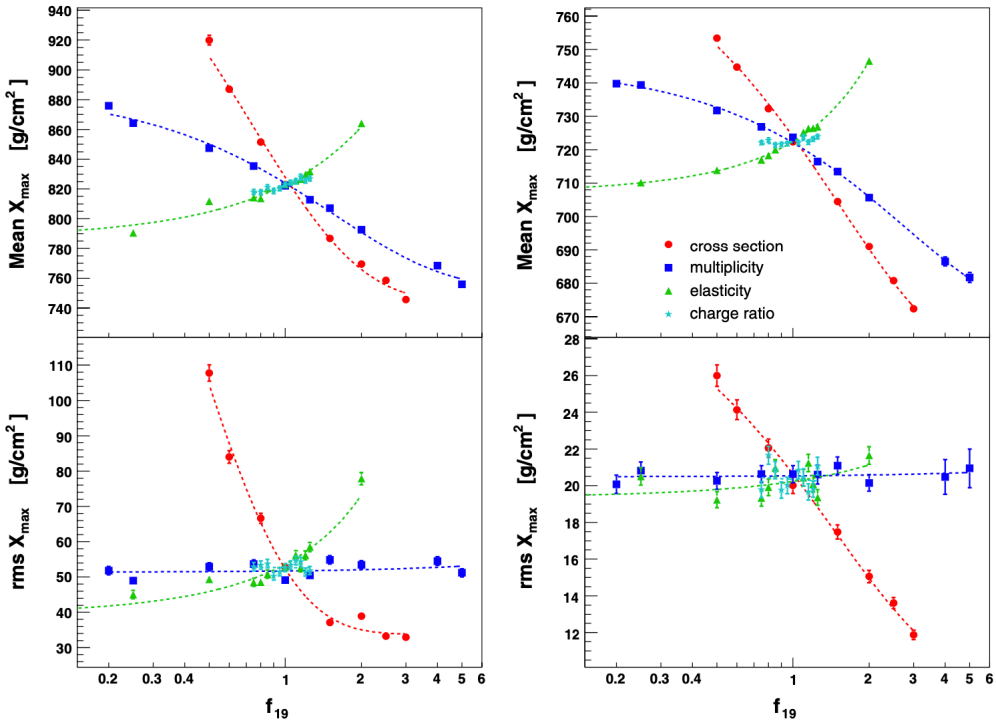

Fig. 2.2: The impact of modification of hadronic interactions on mean of $X_{\max}$ (top panel) and standard deviation of $X_{\max}$ (bottom panel) for proton primary (left) and iron primary (right) [41]. Reprinted figures with permission from [Ralf Ulrich, Ralph Engel, and Michael Unger, Phys. Rev. D 83, 054026, 2011.] Copyright 2011 by the American Physical Society. [41].

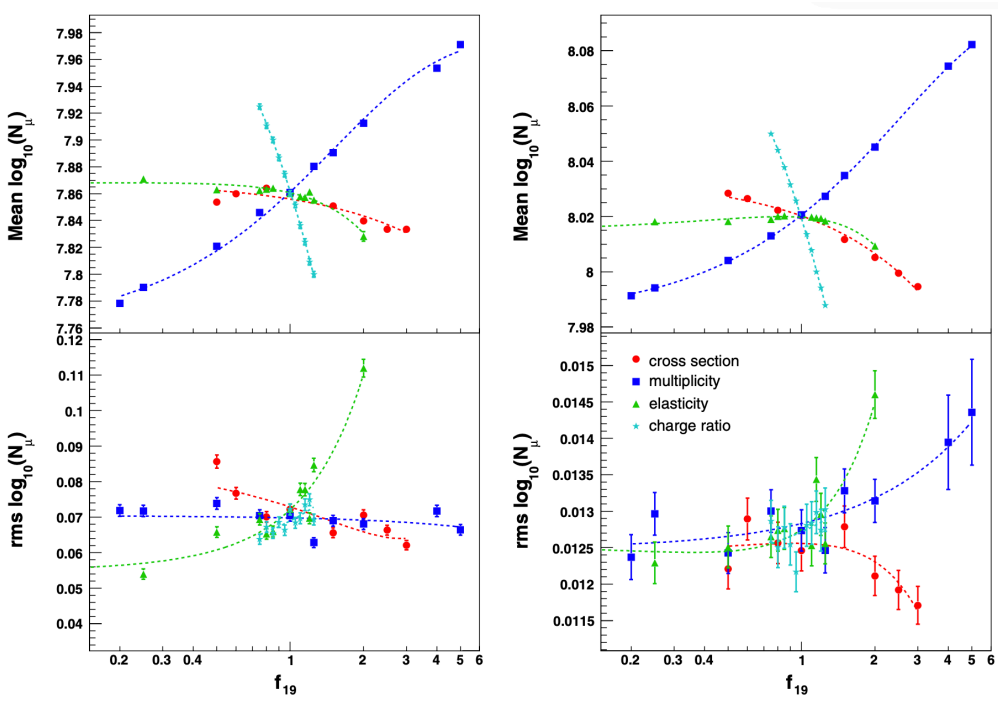

Fig. 2.3: The impact of modification of hadronic interactions on mean of $\log_{10}(N_\mu)$ (top panel) and standard deviation of $\log_{10}(N_\mu)$ (bottom panel) for proton primary (left) and iron primary (right) [41]. Reprinted figures with permission from [Ralf Ulrich, Ralph Engel, and Michael Unger, Phys. Rev. D 83, 054026, 2011.] Copyright 2011 by the American Physical Society. [41].

2.3 Particles produced in the forward regions and the air shower

The relations between interaction in an air shower and $X_{\max}$ or N_μ were discussed in the previous sections based on several characteristics: cross-sections, charge ratio, multiplicity, and elasticity. Meanwhile, a discussion for the relation was given in Ref. [24] by focusing on another aspect of the interaction, *i.e.* the scattering angles of produced particles.

In the study in Ref. [24], the longitudinal profile of the number of electrons and positrons and the muon density on the ground were simulated with the information of the mother particles of these particles, which were produced at the first interaction. The profile and the muon density were discussed with the scattering angle of the ancestor particles at the first interaction. Here, instead of the scattering angle, pseudo-rapidity η, which is defined as

$$\eta = -\ln(\tan\frac{\theta}{2}), \tag{2.17}$$

where θ is the scattering angle of the produced particle, was adopted. The primary particle of the air shower was a 10^{17} eV proton. Note that the η was calculated in the center-of-mass frame of the interaction between a proton and an air nucleus.

Figures 2.4 illustrate the longitudinal profile and the muon density with pseudo-rapidity of mother particles at the first inelastic interaction [24]. Most particles in the longitudinal profile and the muon density are produced from the particle in $|\eta| > 5.0$ at the first interaction. Therefore, particles produced in the large $|\eta|$ regions in the hadronic interaction are important.

In collider experiments, most detectors cover $|\eta| \leq 5.0$, whereas only several detectors cover $|\eta| > 5.0$. At LHC, the regions with $|\eta| > 5.0$ are called forward regions. In the forward regions, equipment to control colliding beams, *e.g.* magnets and beam pipes, exists. Thus, detectors cannot measure all particles produced in forward regions. At LHC, neutral particles in $|\eta| > 8.4$ are measured by zero-degree calorimeters of experiments, forward particles in $\eta \approx 6$ are measured by the CASTOR detector of the CMS experiment and T2 detector of the TOTEM experiment. Scattered beam protons are measured by the detectors inserted in the beam pipe, Roman Pot detectors, utilized by the ATLAS and the TOTEM experiments.

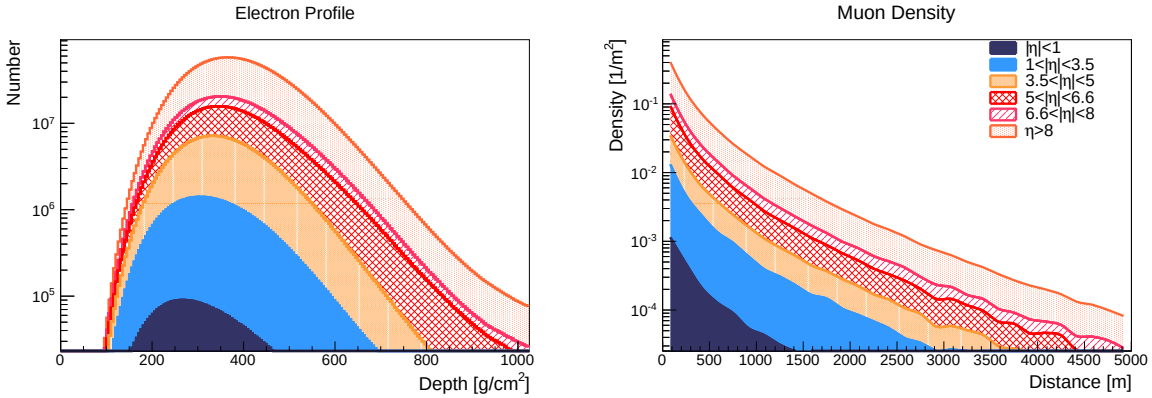

Fig. 2.4: Longitudinal electron profiles (left) and lateral distributions of muons (right) for air showers induced by a 10^{17} eV proton [24]. Histograms are stacked separately for different pseudo-rapidity regions. Pseudo-rapidity is calculated in center-of-mass frame for the first interaction.

Chapter 3

Hadronic interactions and diffractive dissociation

3.1 Hadornic interactions

3.1.1 Overview

A hadron consists of quarks. A quark is an elementary particle and has a color charge. A quark can interact with another quark by exchanging gluons. This interaction is called strong interaction and is successfully described by Quantum Chromodynamics (QCD) (for reviews, please see [43, 44].) A hadron is a color singlet; a hadron does not have a color charge. For example, a proton consists of two up quarks and one down quark. The color charges of three quarks are canceled out.

A collision between hadrons is not simple due to the important feature of QCD: asymptotic freedom. If an energy scale of momentum exchange, Q^2, is large, the coupling constant of QCD is small enough and perturbative QCD works well. Meanwhile, if Q^2 is small, it is impossible to apply perturbative QCD. For example, if Q^2 in a collision is large enough, a collision can be considered as one or several interactions between constituents of each colliding hadron. Interactions among constituents in a hadron can be ignored. Constituents of a hadron are quarks. At high energy, several additional quarks and gluons can be produced by pair creation from the vacuum and can be constituents of a hadron. Figures 3.1(a) and (b) show examples of the collisions. Constituents of colliding hadrons (a) scatter or (b) interact and produce quarks. Hadrons are produced from scattered or produced quarks (hadronization). In hadronic interaction models, the interaction between constituents is calculated by perturbative QCD. Since hadronization includes low Q^2 interactions, it is calculated by a phenomenological model.

If Q^2 is small, we cannot apply perturbative QCD. Interactions among constituents of a hadron are not negligible. Total and elastic cross-sections cannot be calculated from the first principle, since interactions with small Q^2 are important. Instead, in hadronic interaction models, these collisions are calculated by a phenomenological model based on the Regge Theory. In Sec. 3.1, we review the hadronic interaction for these collisions by focusing on proton-proton collisions.

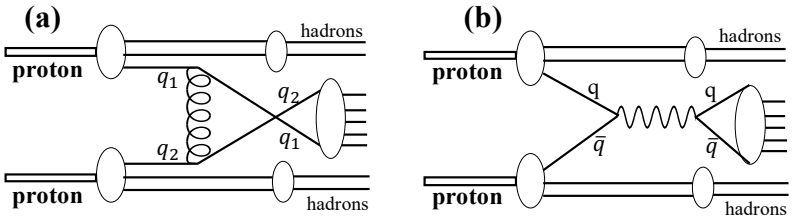

Fig. 3.1: Schematic views of interactions between constituents of colliding protons. (a) Two quarks, q_1 and q_2, in two protons are scattered by a gluon. Hadrons are produced from quarks after the scattering. Circles represent any process for the productions of quacks from proton or for productions of hadrons from quarks. (b) Quark and anti-quark in protons annihilate and produce quarks. Hadrons are produced from quarks after the interaction.

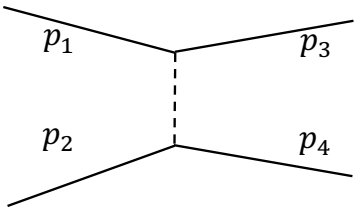

Fig. 3.2: A diagram for elastic scattering.

3.1.2 Mandelastam variables and rapidity

Figure 3.2 illustrates elastic scattering of two particles. Four momenta of incoming particles are represented by p_1 and p_2. Four momenta of outgoing particles are represented by p_3 and p_4. Mandelastam variables s and t are defined as,

$$s = (p_1 + p_2)^2, \tag{3.1}$$

and

$$t = (p_1 - p_3)^2. \tag{3.2}$$

Here, $\sqrt{s}$ corresponds to a center-of-mass energy of the collision.

Rapidity y is defined as,

$$y = \frac{1}{2}\ln(\frac{E + p_z}{E - p_z}), \tag{3.3}$$

where E and p_z are the energy and the momentum of the particle parallel to the proton beam. For mass-less particles, y is identical with pseudo-rapidity η defined in Eq. (2.17).

3.1.3 The total and elastic cross-sections and the optical theorem

Even though it is difficult to calculate total and elastic cross-sections from the first principle, these two cross-sections have an important relation, *i.e.* optical theorem. (For review, see a textbook, for example, [40].) Using an amplitude for the elastic scattering $A_{\rm ela}(s,t)$ as a function of s and t, differential elastic cross-section $d\sigma_{\rm ela}/dt$ is

$$\frac{d\sigma_{\rm ela}}{dt} = \frac{1}{64\pi s k^2}|A_{\rm ela}(s,t)|^2, \tag{3.4}$$

where $k = |\boldsymbol{p}|$ and $\boldsymbol{p}$ is the momentum of the scattered particle in the center-of-mass frame. Note that $\hbar = c = 1$ is assumed here. From the unitarity, total cross-section σ_{tot} have the following relation known as the optical theorem,

$$\sigma_{\text{tot}} = \frac{1}{2k\sqrt{s}} \operatorname{Im} A_{\text{ela}}(s, t \to 0), \tag{3.5}$$

where $A_{\text{ela}}(s, t \to 0)$ is $t \to 0$ limit of the elastic amplitude. Using the ratio of the real part to the imaginary part of the elastic amplitude, ρ, the optical theorem is also written as

$$\sigma_{\text{tot}}^2 = \frac{16\pi}{1+\rho^2} \frac{d\sigma_{\text{ela}}}{dt}\Big|_{t=0}. \tag{3.6}$$

The total cross-section is the sum of the elastic cross-section and the inelastic cross-section. Therefore, from Eq. (3.6), the elastic cross-section at $t \to 0$ limit increases when inelastic cross-section increases. The elastic cross-section at $t \to 0$ limit is called diffractive scattering since this feature in Eq. (3.6) is considered as an analogy to classical wave diffraction; in classical wave diffraction, when the incoming plane wave is absorbed by a thin and small target, diffraction is caused by absorption of the plane wave. By considering inelastic collisions as absorption of the plane wave, the increase of diffractive scattering is an analogy of diffraction. Total cross-section was measured using the optical theorem and measurements of $d\sigma_{\text{ela}}/dt$ by accelerator experiments, *e.g.* the TOTEM experiment [45].

3.1.4 The Regge Theory

Historically, hadronic interactions at low energy can be explained by the Regge Theory as reviewed in Ref. [43, 46]. Before going to proton-proton collisions, we start from $\pi^- + p \to \pi^0 + n$. Cross-sections for $\pi^- + p \to \pi^0 + n$ collisions for a fixed proton target with a π^- beam of 20-200 GeV are well explained by the exchange of families of particles with isospin 1 in the Regge Theory [47]. If we plot the square of the mass, $M^2 = t$, for the horizontal axis and the angular momentum J for the vertical axis for these particles, *e.g.* ρ and a_2, these particles are along a straight line, as illustrated in Fig. 3.3. This is the Regge trajectory. The trajectory is parameterized as,

$$\alpha_R(t) = \alpha(0) + \alpha' t, \tag{3.7}$$

where $\alpha(t) = J$ and $t = M^2$.

The Regge trajectory is extended to the families of imaginary particles with spin 0, isospin 0, and charge 0. These imaginary particles and the trajectory are called Pomeron and the Pomeron trajectory, respectively. Diffractive scatterings in proton-proton collisions are well explained by the exchange of a Pomeron. The Pomeron trajectory, α_P, can also be parametrized as,

$$\alpha_P(t) = 1 + \epsilon + \alpha' t, \tag{3.8}$$

where ϵ and α are parameters for the Pomeron trajectory.

The total and elastic cross-sections of hadronic interactions can be calculated in the Regge Theory. The total cross-section, $\sigma_{\text{total}}^{pp}$, is calculated in Ref. [46] as

$$\sigma_{\text{total}}^{pp} = \sum_k \beta_{pk}(0)^2 s^{\alpha_k(0)-1}, \tag{3.9}$$

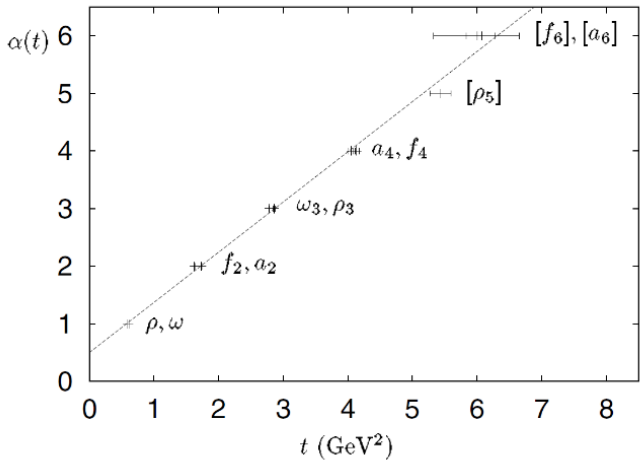

Fig. 3.3: The Regge trajectory. The square of mass and the angular momentum of several mesons are plotted in the horizontal and the vertical axis, respectively. The fitted line corresponds to the trajectory parametrized in Eq. (3.7). The figure is taken from Ref. [48].

where k runs over all possible trajectories. Here, Regge and Pomeron trajectories are considered. $\beta_{pk}(t)$ is the term related to the coupling between a proton and the k trajectory. The elastic cross-section, $\sigma_{\rm el}$, is calculated as

$$\frac{d\sigma_{\rm el}}{dt} = \sum_k \frac{\beta_{pk}(t)^4}{16\pi} s^{2(\alpha_k(t)-1)}. \tag{3.10}$$

The energy dependence of total and elastic cross-sections came from $\alpha(t) - 1$ in each trajectory. For Pomeron trajectory, $\alpha(0) - 1$ is slightly larger than 0 to reproduce the fact that total cross-sections slightly increase at high energy.

3.1.5 Diffractive dissociation

In hadronic interactions, (a) colliding hadron(s) after diffractive scattering sometimes breaks up and produces particles. These collisions are considered that the colliding hadron is excited in diffractive scattering and particles are produced from the excited hadron, and, therefore, called diffractive dissociation. Diffractive dissociation is also explained by an exchange of the Pomeron. After an exchange of the Pomeron, a colliding proton sometimes becomes an excited state and dissociates.

There are several types of diffractive dissociation as illustrated in Fig. 3.4: one of the colliding particles dissociates (single-diffractive dissociation, SD), both of the colliding particles dissociate (double-diffractive dissociation, DD). Moreover, particles are sometimes produced from the interaction between two Pomerons, whereas two colliding particles are intact. This additional type is called central-diffractive dissociation (CD). Hereafter, we focus on diffractive dissociation. Inelastic collisions other than diffractive dissociation are called non-diffractive collisions (ND) in this study.

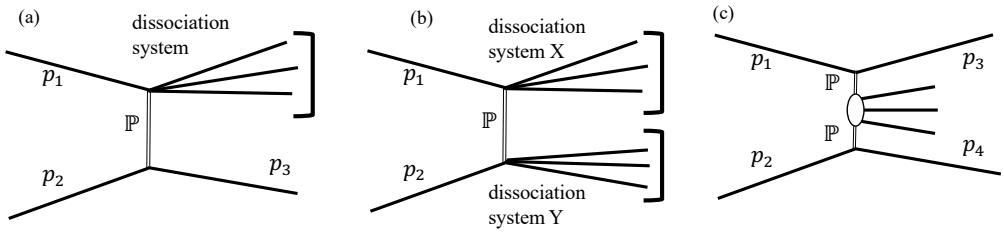

Fig. 3.4: Feynman diagrams for (a) single-, (b) double-, and (c) centeral-diffractive dissociation. These figures are reproduced from Ref. [49].

3.1.6 Diffractive mass and rapidity gaps

There are important characteristics in diffractive dissociation: diffractive mass and rapidity gaps. Diffractive mass corresponds to the mass of the excited proton in diffractive dissociation. For SD as illustrated in Fig. 3.4, the square of the diffractive mass, M_{X}^2, is defined as follows,

$$M_{\mathrm{X}}^2 = (p_1 + p_2 - p_3)^2 = \Big(\sum_i p^i\Big)^2, \tag{3.11}$$

where p_1 and p_2 are four momentum of initial particles. p_3 is four momentum of the scattered proton. i runs over all final-state particles in the dissociation system and p^i is four momentum of each particle.

Experimentally, diffractive dissociation is characterized by a large rapidity gap, a rapidity interval without produced particles. The rapidity gap depends on the diffractive mass. Figure 3.5 illustrates a schematic view of the rapidity gap. If we consider an "excited" state of proton with mass M_X and it dissociates into particles in the dissociation system, the rapidity of each particle y_i is

$$y_i = \langle y \rangle + \delta y, \tag{3.12}$$

where $\langle y \rangle$ is the mean rapidity of the particles in the dissociation system, and δy is the difference of rapidity from the mean for each particle. $\langle y \rangle$ corresponds to the rapidity of the "excited" state of proton. In the center-of-mass frame and $\sqrt{s} \gg M_X$ limit, the "excited" state of proton flying parallel to the initial proton have $p_z \approx \frac{\sqrt{s}}{2}$, then, $\langle y \rangle$ is

$$\langle y \rangle = \ln \frac{\sqrt{s}}{M_X}. \tag{3.13}$$

By assuming that particles in the dissociation system distribute in the range of $\pm \ln \frac{M_X}{m_p}$ [46], where m_p is a proton mass, the minimum rapidity in the dissociation system, y_{min}, is

$$y_{\mathrm{min}} = \ln \frac{\sqrt{s}}{M_X} - \ln \frac{M_X}{m_p} = \ln \frac{m_p \sqrt{s}}{M_X^2}. \tag{3.14}$$

Here we assume $\sqrt{s} \gg m_p$. The rapidity of the proton scattered in the opposite direction is $y_{\mathrm{proton}} = -\ln(\sqrt{s}/m_p)$. The rapidity gap is an interval in rapidity between the scattered

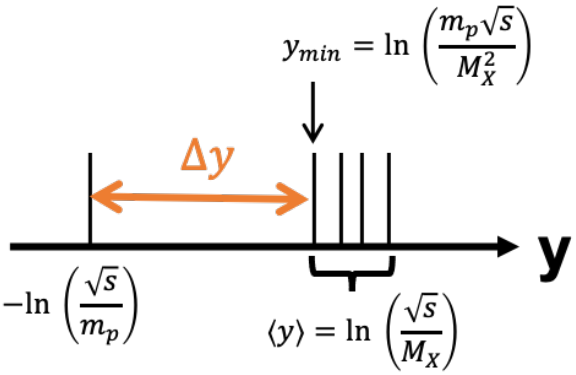

Fig. 3.5: A schematic view of the rapidity gap. Horizontal axis is the rapidity y. Each vertical line represents a particle at the rapidity.

proton and the minimum rapidity particle in the dissociation system. Therefore, the rapidity gap is

$$\Delta y = \ln \frac{s}{M_X^2} = -\ln \xi. \tag{3.15}$$

Here, $\xi \equiv M_X^2/s$. For diffractive dissociation with $M_{\rm X} = 10\,{\rm GeV/c^2}$ in proton-proton collisions with $\sqrt{s} = 13\,{\rm TeV}$, $\Delta y \sim 14.3$ and $y_{\rm min} \sim 4.8$. Thus, in diffractive dissociation, a very large rapidity gap is expected. For diffractive dissociation with higher mass, *e.g.* $M_{\rm X} = 100\,{\rm GeV/c^2}$, $\Delta y \sim 9.7$ and $y_{\rm min} \sim 0.20$.

Detectors typically need to cover the pseudo-rapidity $\eta \sim y_{\rm min}$ at least to detect particles in the dissociation system. As $M_{\rm X}$ becomes lower, $y_{\rm min}$ become larger. Thus, detections of low diffractive-mass cases, typically $M_{\rm X} < 3.4\,{\rm GeV/c^2}$ or $\log_{10}\xi < -6.6$ for proton-proton collisions with $\sqrt{s} = 13\,{\rm TeV}$, are hard since detectors need to cover very forward regions. In this thesis, we call the regions with $M_{\rm X} < 3.4\,{\rm GeV/c^2}$ or $\log_{10}\xi < -6.6$ for proton-proton collisions with $\sqrt{s} = 13\,{\rm TeV}$ as low diffractive-mass regions. We call the regions with $M_{\rm X} < 3.4\,{\rm GeV/c^2}$ and $\Delta\eta > 3.0$ as middle diffractive-mass regions. The middle diffractive-mass regions were measured by several detectors.

The rapidity gap Δy is an important parameter to measure diffractive dissociation. We can separate diffractive dissociation and the other collisions using Δy since only diffractive dissociation shows large Δy. Moreover, Δy and $y_{\rm min}$ are useful parameters to estimate diffractive mass since they depend on diffractive mass. Unfortunately, diffractive dissociation with very high diffractive mass cannot be distinguished from the other collisions since it shows small Δy.

Measurements of diffractive dissociation using the rapidity gap were performed by many experiments. Particles considered in the detection of the rapidity gap depend on detectors in each experiment. Typically, charged particles and several neutral particles, *e.g.* gamma-rays and neutral hadrons, are considered using tracking detectors and calorimeters. In $\sqrt{s} \gg m$ for particles in dissociation system, $\Delta y \approx \Delta\eta$, where $\Delta\eta$ is the gap in pseudo-rapidity. Since pseudo-rapidity is calculated only from the scattering angle of each particle, the rapidity gap in pseudo-rapidity is also used in the experiments.

3.2 Phenomenological models for diffractive dissociation

In each hadronic interaction model, diffractive dissociation is described by a phenomenological model based on the Regge Theory and tuned with experimental data. In PYTHIA8 [50], cross-sections for diffractive dissociation are modeled with the parameters for the Pomeron trajectory. There are several different versions of tune for diffractive dissociation in PYTHIA8, *e.g.* tunes by Donnachie and Landoshoff [51] (DL hereafter) and Minimum Bias Rockefeller tune [52] (MBR hereafter). Parameters ϵ and α in Eq. (3.8) are tuned by available experimental data for total cross-sections. Cross-sections for diffractive dissociation are calculated from the Regge Theory using these Pomeron trajectory parameters and coupling constants for Pomeron. For example, in MBR tune [52], the cross-section of SD is modeled as,

$$\frac{d^2\sigma_{\rm SD}}{dtd\Delta y} = \frac{1}{N_{\rm gap}(s)}\left[\frac{\beta^2(t)}{16\pi}e^{2[\alpha(t)-1]\Delta y}\right]\left(\kappa\beta^2(0)(\frac{s^{'}}{s_0})^{\epsilon}\right), \tag{3.16}$$

where Δy is the size of rapidity gap, $\beta(t)$ is the Pomeron-proton coupling. $\alpha(t)$ is the Pomeron trajectory. ϵ is a parameter in the Pomeron trajectory. κ is the ratio of triple-Pomeron coupling to $\beta(0)$. $s^{'}$ is the square of center-of-mass energy. $N_{\rm gap}(s)$ is the gap renormalization factor [53].

In SIBYLL 2.3 [31, 54], diffractive dissociation is modeled based on Good-Walker model [55]. In the model, with considering two state of proton, ground state of proton, $|p\rangle$, and diffractive state of proton, $|p^*\rangle$, and the elastic amplitude A_{ela}, the amplitude for SD A_{SD} is modeled as [31],

$$\langle p^*p|A_{SD}|pp\rangle = \lambda A_{ela}, \tag{3.17}$$

where λ is a coupling constant for diffractive dissociation and depends on s. Elastic cross-sections for proton-proton collisions, $\sigma^{\rm pp}_{\rm ela}(s)$, and SD cross-sections for lower mass cases, $\sigma^{\rm pp}_{{\rm SD},\xi<\xi^{\rm max}}(s)$, have the following relation,

$$\lambda^2(s) = \frac{\sigma^{\rm pp}_{{\rm SD},\xi<\xi^{\rm max}}(s)}{\sigma^{\rm pp}_{\rm ela}(s)}. \tag{3.18}$$

Here, SD events with $\xi < \xi^{\rm max}$, where $\xi^{\rm max}$ is the upper limit of the ξ value, are only considered. In calculations in SIBYLL 2.3, the upper limit is set to be $\xi^{\rm max} = 0.02$. The coupling constant $\lambda(s)$ is tuned from this relation and experimental data for the SD cross-section. Figure 1.6 illustrates the SD cross-section calculated by SIBYLL 2.3 with three different upper limits $\xi^{\rm max}$ in the calculations: $\xi^{\rm max} = 0.2$ (dashed line), $\xi^{\rm max} = 0.05$ (solid line), and $\xi^{\rm max} = 0.02$ (solid line). The tuning was performed with $\xi^{\rm max} = 0.05$, which corresponds to the definition in the experiments shown in the plot. The red squares in Fig. 1.6 are the ALICE results with $M_{\rm X} < 200$ GeV/c^2. The red circles are the ALICE results extrapolated to $\xi < 0.05$. Uncertainties in experimental results affect the uncertainty in the tuning of λ. Since the Good-Waler model is not valid for high mass diffractive dissociation [46], a fixed fraction of the ND events is considered as high mass diffractive dissociation for $\xi^{\rm max} > 0.02$ in SIBYLL 2.3.

Predictions for collisions between a proton and a light ion or between a light ion and a light ion are described by extending the model for proton-proton collisions. There are large differences in the extrapolation from proton-proton collisions to proton-light ion collisions among hadronic interaction models. For example in SIBYLL 2.3, DD in proton-light ion

interaction model	Fraction in inelastic collisions [%] projectile SD ($pp \to Xp$)	target SD ($pp \to pY$)	DD
EPOS-LHC	6.3	6.4	11.7
QGSJET II-04	7.1	7.2	6.4
SIBYLL 2.3c	7.5	7.4	2.1

Table 3.1: Fraction of SD and DD in inelastic collisions for proton-proton collisions predicted by EPOS-LHC, QGSJET II-04, and SIBYLL2.3c. Collisions between a proton with 10^{17} eV and a proton at rest are simulated with CMRC v1.7.

interaction model	Fraction in inelastic collisions [%] projectile SD ($pN \to XN$)	target SD ($pN \to pY$)	DD
EPOS-LHC	4.2	4.3	8.1
QGSJET II-04	5.9	3.5	3.4
SIBYLL 2.3c	6.6	3.0	0.8

Table 3.2: Fraction of SD and DD in inelastic collisions for proton-Nitrogen nucleus collisions predicted by EPOS-LHC, QGSJET II-04, and SIBYLL2.3c. Collisions between a proton with 10^{17} eV and a nitrogen nucleus at rest are simulated with CMRC v1.7.

collisions is calculated by considering completely independent interactions between a proton and a nucleon in the nucleus. If all independent interactions between nucleons are DD, the collision is treated as DD. Meanwhile, projectile SD in proton-light ion collisions is treated systematically with considering the excitation to the diffractive state caused by the nucleus [31]. Excitation and de-excitation of a projectile proton to/from the diffractive state by each nucleon in the nucleus are considered coherently. This effect enhances projectile SD in proton-light ion collisions. Tables 3.1 and 3.2 show the fraction of each type of diffractive dissociation for the collision of a 10^{17} eV proton with either a proton or a Nitrogen nucleus at rest simulated by CRMC version 1.7 [56]. The fractions of projectile SD and target SD in SIBYLL 2.3 are comparable for proton-proton collisions as shown in Tab. 3.1, whereas the fraction of projectile SD is more than twice than that of target SD as shown in Tab. 3.2. The fractions of projectile SD and target SD by EPOS-LHC are, however, comparable even for proton-Nitrogen collisions. No enhancements of projectile SD are considered in EPOS-LHC.

Differences in the modeling of diffractive dissociation affect cross-sections. Figure 3.6 illustrates SD ($pp \to Xp$) cross-sections as a function of $\log_{10}\xi$ for proton-proton collisions with $\sqrt{s} = 13$ TeV predicted by EPOS-LHC (magenta solid line), QGSJET II-04 (blue dotted line), SIBYLL 2.3 (green dashed line), PYTHIA8 DL (orange dash-dotted line), and PYTHIA8 MBR (red dash-two-dotted line). For parameters of the Pomeron trajectory in PYTHIA8, $\epsilon = 0.085$ and $\alpha' = 0.250$ GeV^{-2} are adopted for PYTHIA8 DL and $\epsilon = 0.104$ and $\alpha' = 0.250$ GeV^{-2} are adopted for PYTHIA8 MBR. Parameters were tuned using measurements of total cross-sections for (anti)proton-proton collisions for DL tune, whereas they were tuned using measurements for (anti)proton-proton, $\pi^{\pm}$-proton, and $K^{\pm}$-proton collisions for MBR tune [57]. Predictions of cross-sections become larger with $\log_{10}\xi$ become smaller except for SIBYLL 2.3, whereas large differences can be found in the slope. EPOS-LHC shows a clear peak at $\log_{10}\xi \approx -8.0$. There are very large differences of predictions of cross-sections in $\log_{10}\xi < -6.5$.

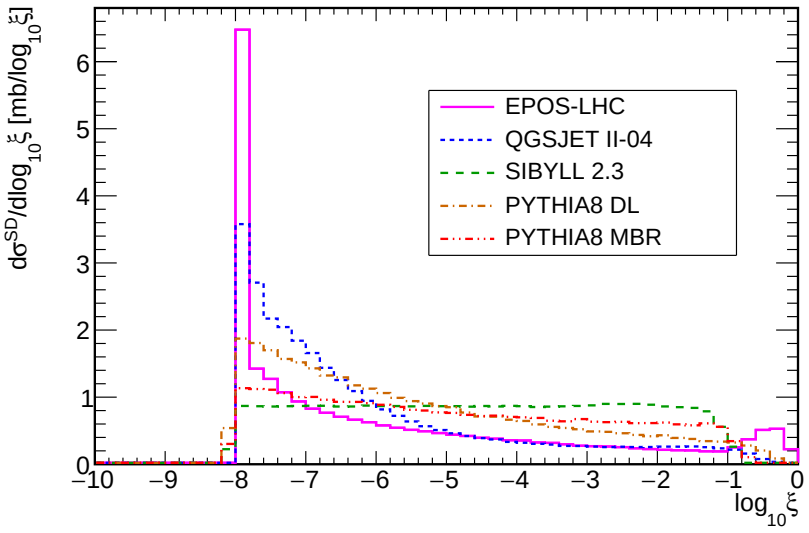

Fig. 3.6: SD ($pp \to Xp$) cross-sections predicted by EPOS-LHC (magenta solid), QGSJET II-04 (blue dotted), SIBYLL 2.3 (green dashed), PYTHIA8 DL (orange dash-dotted), and PYTHIA8 MBR (red dash-two-dotted).

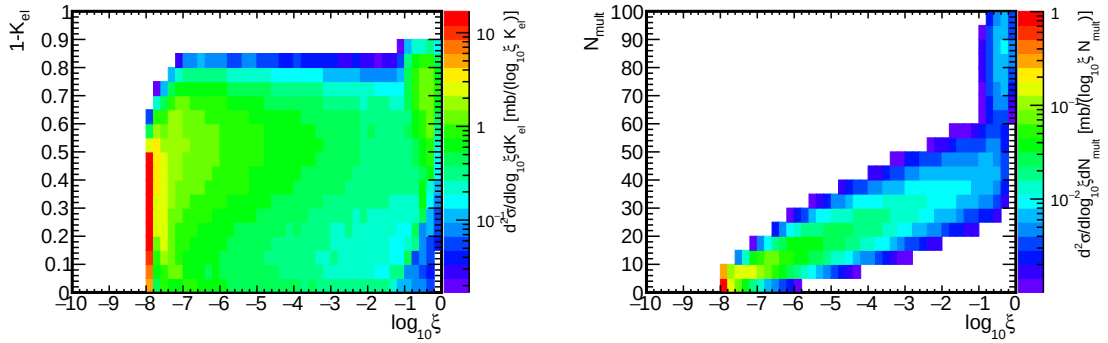

Fig. 3.7: Diffractive mass dependencies of elasticity $K_{\rm el}$ (left) and multiplicity $N_{\rm mult}$ (right) for SD ($pp \to Xp$) predicted by EPOS-LHC simulated by CRMC v1.6.

Diffractive mass affects predictions of particle productions. Figure 3.7 illustrates $\log_{10}\xi$ dependencies of elasticity (left) and multiplicity (right) for SD ($pp \to Xp$) in proton-proton collisions with $\sqrt{s} = 13$ TeV in the center-of-mass frame. Here, elasticity in the center-of-mass frame is calculated using the most energetic particle produced in proton dissociation as the following equation,

$$K_{\rm el} = E_1/E_0, \tag{3.19}$$

where E_1 is the energy of the most energetic particle. E_0 is the energy of the beam proton. Collisions with smaller diffractive mass produce a smaller number of particles and a larger elasticity. In air showers induced by cosmic rays, projectiles dissociate for projectile SD and DD cases, whereas projectiles are intact for target SD and CD cases. Thus, diffractive-mass dependencies in particle productions may affect $X_{\rm max}$ or N_μ through projectile SD and DD collisions.

3.3 Collider experiments and results for diffractive dissociation

3.3.1 Measurements of diffractive dissociation in experiments

Diffractive dissociation has been measured by detecting a large rapidity gap in many experiments. Since most of the detectors at LHC detect particles in $|\eta| < 6.5$ except for several very forward detectors, measurements of a large rapidity gap were limited. For example, for proton-proton collisions at $\sqrt{s} = 7$ TeV, most of very low diffractive-mass events with $M_X < 3.4$ GeV did not make signals in detectors covering $|\eta| < 6.5$. Other possibilities to measure cross-sections of diffractive dissociation were methods using forward detectors covering $|\eta| > 6.5$. The Roman Pot detector was one of them. Using the Roman Pot detectors, protons scattered in SD were measured by the ATLAS experiment [58]. Total and inelastic cross-sections were precisely measured with Roman Pot detectors and the optical theorem by TOTEM [45, 59] and ATLAS experiments [60].

3.3.2 Results by the CMS experiment

Measurements of cross-sections for SD and DD were performed using central detectors and the CASTOR detector of the CMS experiment, which covers $|\eta| \leq 4.7$ and $-6.5 < \eta < -5.2$, respectively, for proton-proton collisions at $\sqrt{s} = 7$ TeV [29]. $\xi_{\rm X}$ corresponds to ξ of the dissociation system in the side with the CASTOR detector. $M_{\rm Y}$ corresponds to the diffractive mass of the dissociation system on the opposite side. The events were categorized into three samples using the particle with the maximum pseudo-rapidity, $y^{\rm X}_{\rm max}$, in dissociation system for the CASTOR detector side and the particle with the minimum pseudo-rapidity, $y^{\rm Y}_{\rm min}$, in dissociation system for the opposite side. If both the particles were measured in the central detectors and a large rapidity gap was found between two particles, these events are categorized into the CG sample. If the particle with $y^{\rm Y}_{\rm min}$ was measured and the particle with $y^{\rm X}_{\rm max}$ was not measured in the central detector, the events were categorized into two samples: the sample with detection of particles in the CASTOR detector (the CASTOR sample) and the sample without detection of particles in the CASTOR detector (the no-CASTOR sample). These samples contain both SD and DD processes. Cross-sections of diffractive dissociation for these three samples were as follows.

- $\sigma_{\rm no-CASTOR} = 2.99 \pm 0.02^{+0.32}_{-0.29}$ mb for $-5.5 < \log \xi_{\rm X} < -2.5$ and $\log_{10} M_{\rm Y} < 0.5$, which are dominated by SD,
- $\sigma_{\rm CASTOR} = 1.18 \pm 0.02 \pm 0.13$ mb for $-5.5 < \log \xi_{\rm X} < -2.5$ and $0.5 < \log_{10} M_{\rm Y} < 1.1$, which are dominated by DD, and
- $\sigma_{\rm CG} = 0.58 \pm 0.01^{+0.13}_{-0.11}$ mb for $\log_{10} M_{\rm X} > 1.1$ and $\log_{10} M_{\rm Y} > 1.1$ and $\Delta\eta > 3$, where $\Delta\eta = -\log(\sqrt{M_X^2 M_Y^2/(s m_p^2)})$,

Figures 3.8 and 3.9 illustrate differential cross-sections $d\sigma/d\log_{10}\xi$ measured by the CMS experiment in Ref. [29] and predictions by hadronic interaction models. PYTHIA8 MBR with $\epsilon = 0.08$ shows good agreements with data, whereas QGSJET II-04 and EPOS-LHC underestimate the data. These results at middle diffractive-mass regions were extrapolated

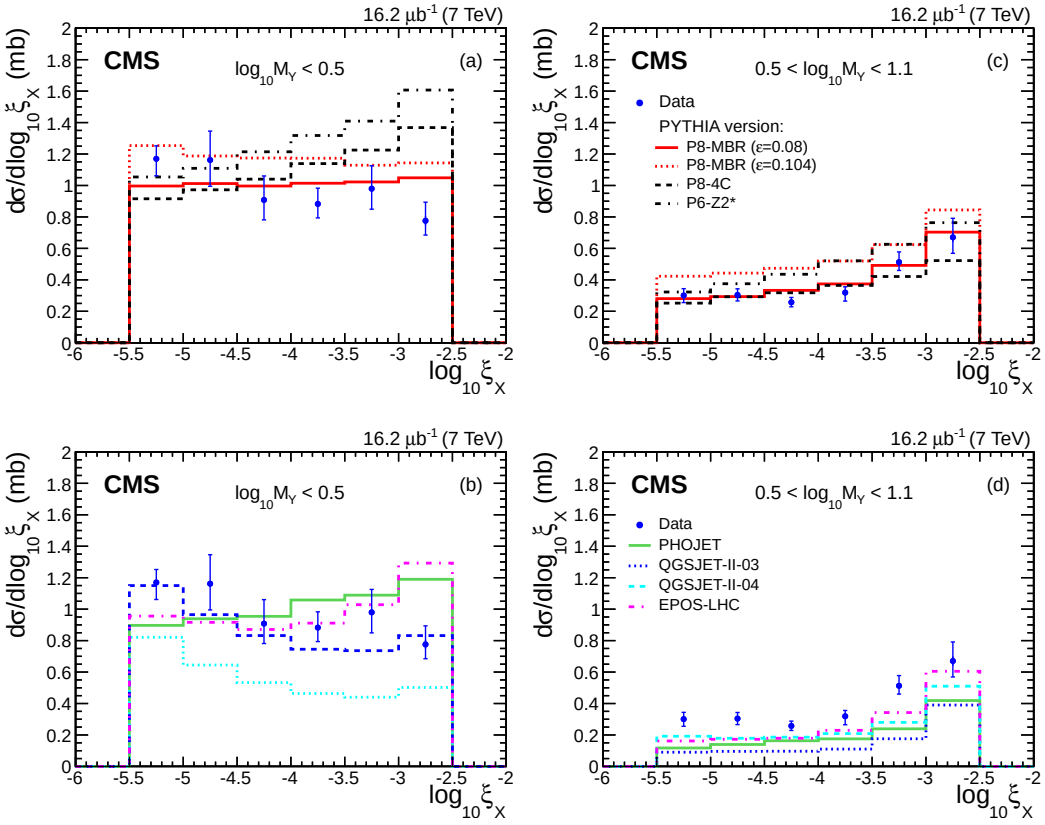

Fig. 3.8: Differential cross-sections of diffractive dissociation $d\sigma/d\log_{10}\xi$ (a, b) in $-5.5 < \log\xi_{\rm X} < -2.5$ *and* $\log_{10} M_{\rm Y} < 0.5$ and (c, d) in $-5.5 < \log\xi_{\rm X} < -2.5$ *and* $0.5 < \log_{10} M_{\rm Y} < 1.1$ for proton-proton collisions at $\sqrt{s} = 7$ TeV measured by CMS experiments [29].

using PYTHIA8 MBR, since the model well reproduced the experimental results. The results of cross-sections for SD and DD were as follows;

$$\sigma^{\rm SD} = 8.84 \pm 0.08({\rm stat.})^{+1.49}_{-1.38}({\rm syst.})^{+1.17}_{-0.37}({\rm extrapolation})\ {\rm mb}\ , \tag{3.20}$$

for SD with $\xi_X < 0.05$, and

$$\sigma^{DD} = 5.17 \pm 0.08({\rm stat.})^{+0.55}_{-0.57}({\rm syst.})^{+1.62}_{-0.51}({\rm extrapolation})\ {\rm mb} \tag{3.21}$$

for DD with $\Delta\eta > 3$. These results were extrapolated by PYTHIA 8 MBR.

The measurement of inelastic cross-section for proton-proton collisions at $\sqrt{s} = 13$ TeV was performed by the CMS experiment in Ref. [61]. Inelastic cross-sections were measured for two samples; one is the sample with either the ND events and diffractive dissociation with $\xi > 10^{-6}$. The other is the sample with either the ND events and diffractive dissociation with $\xi_X > 10^{-7}$ or $\xi_Y > 10^{-6}$. Results are illustrated in Fig. 3.10 with predictions by hadronic interaction models. In Ref. [61], they concluded that extrapolations using hadronic interaction models would underestimate the total inelastic cross-section, since no model reproduced two inelastic cross-sections.

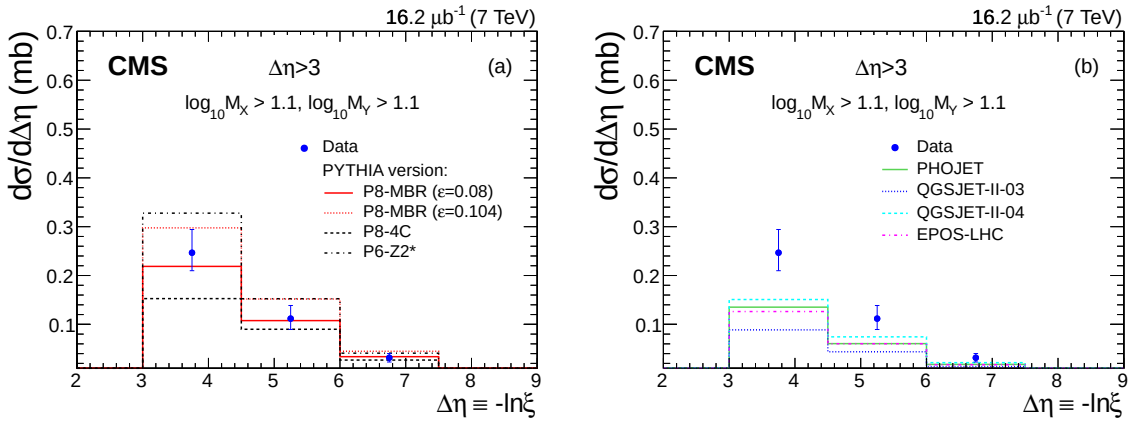

Fig. 3.9: Differential cross-sections of diffractive dissociation in $\log_{10} M_{\mathrm{X}} > 1.1$ *and* $\log_{10} M_{\mathrm{Y}} > 1.1$ and $\Delta\eta > 3$ for proton-proton collisions at $\sqrt{s} = 7$ TeV measured by CMS experiments [29].

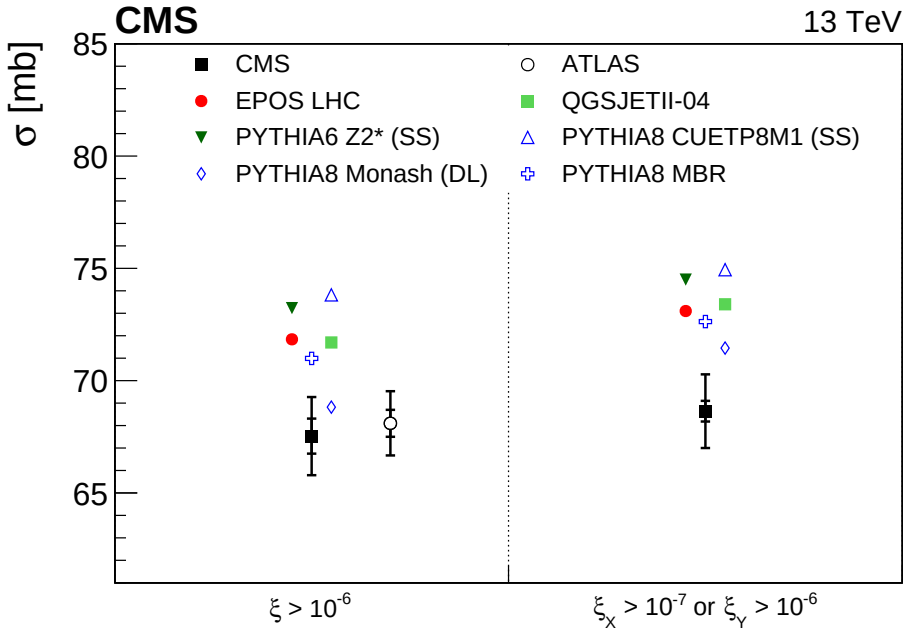

Fig. 3.10: Inelastic cross-sections measured by CMS and ATLAS experiments for proton-proton collisions at $\sqrt{s} = 13$ TeV [61, 62]. The figure is taken from Ref. [61]

3.3.3 Results by the ALICE experiment

Measurements of cross-sections for SD and DD in proton-proton collisions at $\sqrt{s} = 7$ TeV were performed by the ALICE experiments using detectors covering $-3.7 < \eta < -1.7$, $|\eta| < 2.0$, and $1.7 < \eta < 5.1$ [30]. Inelastic cross-section was measured using luminosity measured by van der Meer scans and simulations for trigger efficiency. Rates for SD and DD were measured using these detectors except for the low diffractive-mass regions and were extrapolated using models. The results of cross-sections are

$$\sigma^{\mathrm{SD}} = 14.9^{+3.4}_{-5.9}\ \mathrm{mb} \tag{3.22}$$

for SD with $M_X < 200\ \mathrm{GeV/c^2}$ and

$$\sigma^{\mathrm{DD}} = 9.0 \pm 2.6\ \mathrm{mb} \tag{3.23}$$

for DD with $\Delta\eta^{\mathrm{gap}} > 3$, where $\Delta\eta^{\mathrm{gap}}$ is a rapidity gap in charged particle distributions.

3.3.4 Results by the TOTEM experiment

A measurement of cross-sections for very low diffractive-mass events with $M_X < 3.4\ \mathrm{GeV/c^2}$ was performed by comparing two inelastic cross-section measurements in Ref. [38]. Using T1 and T2 telescopes, which covers $3.1 \leq |\eta| \leq 4.7$ and $5.3 \leq |\eta| \leq 6.5$, respectively, the inelastic cross-section for events with particle productions in $|\eta| < 6.5$ was measured in Ref [38]. Independently, total and inelastic cross-section was measured by Roman Pot detectors and the optical theorem with no assumption for low diffractive-mass events in Ref. [45]. By subtracting two inelastic cross-sections, inelastic cross-sections for events without particle productions in $|\eta| < 6.5$, which correspond to very low diffractive-mass events with $M_X < 3.4\ \mathrm{GeV/c^2}$ including both SD and DD contributions, was measured as [38],

$$\sigma_{\mathrm{inel},|\eta|>6.5} = 2.62 \pm 2.17\ \mathrm{mb}. \tag{3.24}$$

The similar analysis was performed by the ATLAS experiment in Ref. [62]. Based on inelastic cross-section measurements by the ATLAS experiment [60, 63], the cross-sections for diffractive dissociation for $\xi < 5 \times 10^6$ was measured for proton-proton collisions with $\sqrt{s} = 7$ TeV as,

$$\sigma(\xi < 5 \times 10^6) = 9.9 \pm 2.4\ \mathrm{mb}. \tag{3.25}$$

The method adopted in these results is the only method for published results of cross-sections for very low diffractive-mass events. Experimental uncertainties of these results are large even though the cross-section is only considering very low diffractive-mass regions. One should note that it is impossible to separate SD and DD contributions in this method.

3.3.5 Very low diffractive mass events

It is very hard to detect a very large rapidity gap produced in very low diffractive-mass events, whereas large cross-sections are predicted for these cases. Detectors covering $|\eta| > 6.5$, *e.g.* zero degree calorimeters and Roman Pot detectors, are necessary for the detection of these very low diffractive-mass events. Uncertainties for SD and DD cross-sections are not so large in the results by the CMS experiment discussed in Sec. 3.3.2 because extrapolations for low

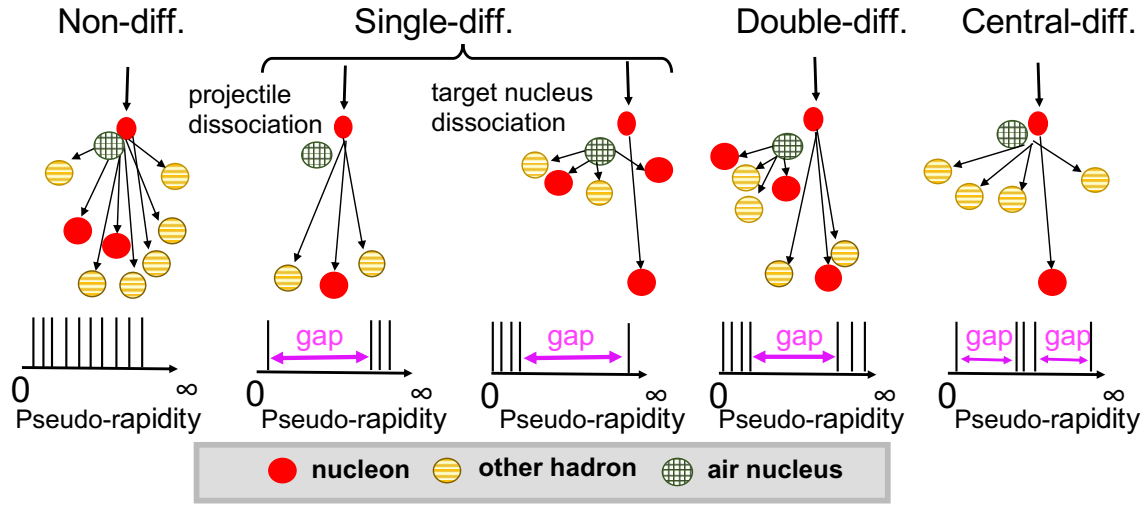

Fig. 3.11: Schematic views of ND, SD, DD, and CD for the first interaction of the air shower in the lab frame. These figures are reproduced and modified from Ref. [49].

diffractive-mass events were performed by one model, which is PYTHIA8 MBR. However, the validity is unclear for very low diffractive-mass events. Uncertainty becomes very large if many models are considered in extrapolations. Cross-sections for very low diffractive-mass events were estimated indirectly using two different measurements of inelastic cross-sections by the TOTEM and the ATLAS experiments, as discussed in the previous section. These cross-sections were measured successfully, however, experimental uncertainties for these results are large.

The possibility to measure very low diffractive-mass events directly is detecting forward neutral particles produced in these events by zero degree calorimeters. Using zero-degree calorimeters, we can measure particles in the largest rapidity regions. This measurement can validate models used for extrapolations of low diffractive-mass events in experiments. We discuss this possibility in Chap. 6 and 7.

3.4 Effects of diffractive dissociation on air shower

From a cosmic-ray point of view, SD can be divided into two types: projectile SD, where a projectile cosmic-ray particle dissociates, and target SD, where a target air nucleus dissociates and a projectile cosmic-ray particle is intact. Effects on the air shower are different among these types; if a comic-ray particle is intact, most of the projectile particle energy is carried by one particle. Thus, $X_{\max}$ becomes one interaction length larger. Meanwhile, in projectile SD and DD, a projectile cosmic-ray particle dissociates. In this case, the projectile particle energy is shared by the several particles produced in the dissociation. The elasticity is typically larger than ND but smaller than target SD. Therefore, we can categorize hadronic collisions into five types as illustrated in Figs. 3.11: projectile SD, target SD, DD, CD, and ND.

Effects of diffractive dissociation were discussed in the previous studies [36, 39]. In Ref. [36], two additional tunes for QGSJET II-04 was produced: SD+ and SD-. SD+ was tuned using the results by the ATLAS [37] and the CMS [29] experiments. SD- was tuned

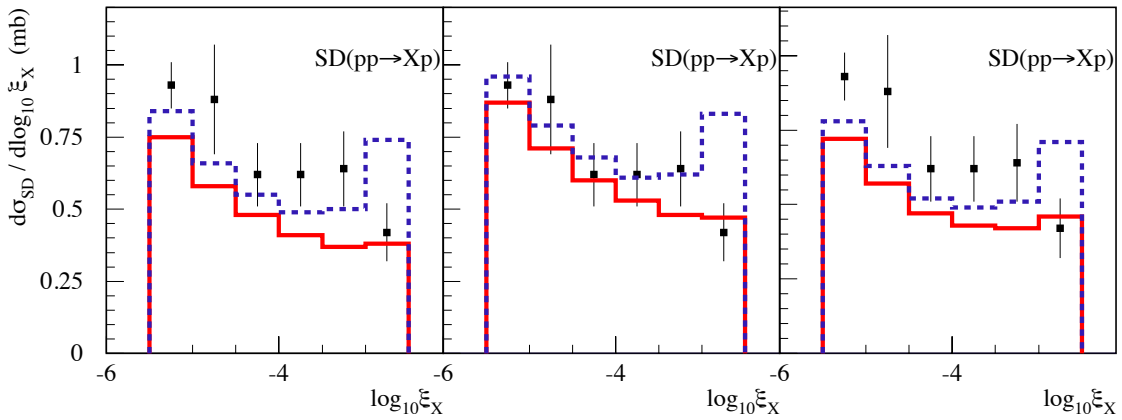

Fig. 3.12: $d\sigma_{\mathrm{SD}}/d\log_{10}\xi_{\mathrm{X}}$ measured by the CMS experiment (black points) [29] and its predictions by QGSJET II-04 default(left), SD+ (middle), SD- (right) [36]. Red solid lines are predictions for SD. Blue dashed lines are predictions for SD and DD with $M_{\mathrm{Y}} < 3\ \mathrm{GeV/c^2}$. Reprinted figures with permission from [S. Ostapchenko, Phys. Rev. D 89, 074009, 2014.] Copyright 2014 by the American Physical Society.

using the results of the TOTEM experiment [38]. Figures 3.12 illustrate $d\sigma_{\mathrm{SD}}/d\log_{10}\xi_{\mathrm{X}}$ measured by the CMS experiments [29] and predicted by these tunes. SD+ showed better agreements with the results of the CMS experiment [29]. Tuning was also performed using the results by the ATLAS [37] and the TOTEM [38] experiments. Predictions of $\langle X_{\mathrm{max}}\rangle$ and $\sigma(X_{\mathrm{max}})$ by these tunes were illustrated in Fig. 3.13. Effects of these tunes on $\langle X_{\mathrm{max}}\rangle$ were estimated to be $10\ \mathrm{g/cm^2}$. However, these tunes also affected cross-sections as illustrated in Fig. 3.14. Therefore, the effects of SD and other effects were not separated in this way. Another previous study in Ref. [39] was performed with an extreme assumption, turning all the diffractive dissociation off in air shower simulations. The effects of SD and DD were not separated. In consequence, the effects of each type of diffractive dissociation were unclear in previous studies, even though the effect of each type of diffractive dissociation is different qualitatively.

Another problem in the previous studies is that effects are estimated in the definitions based on the hadronic interaction model. Since the definition of experimental results depends on the coverage of detectors adopted in each experiment, the effects of experimental results and their uncertainty are unclear. In the CMS experiment, SD and DD cross-sections for proton-proton collisions with $\sqrt{s} = 7\ \mathrm{TeV}$ were measured for $\xi_{\mathrm{X}} < 0.05$ and $\Delta\eta < 3$, respectively. In the ALICE experiment, SD and DD cross-sections for proton-proton collisions with $\sqrt{s} = 7\ \mathrm{TeV}$ were measured for $M_{\mathrm{X}} < 200\ \mathrm{GeV/c^2}$ and $\Delta\eta^{\mathrm{gap}} < 3$, respectively. ND contamination was expected for DD. Large experimental uncertainty exists in the ALICE results. However, in the previous studies, the effects of these experimental definitions were unclear. To understand the effects of the experimental uncertainty on X_{max} predictions, a study based on these experimental definitions is necessary.

The analyses using the air shower simulation are performed in the following chapters to solve these problems. The effects of collision types and characteristics in diffractive dissociation on predictions of X_{max} or N_{μ} are discussed comprehensively in Chap. 4; effects of ratios of each collision type to other collision types are discussed. The effects of diffractive mass dependencies of cross-sections are also discussed. Effects on $\langle X_{\mathrm{max}}\rangle$, $\sigma(X_{\mathrm{max}})$, the

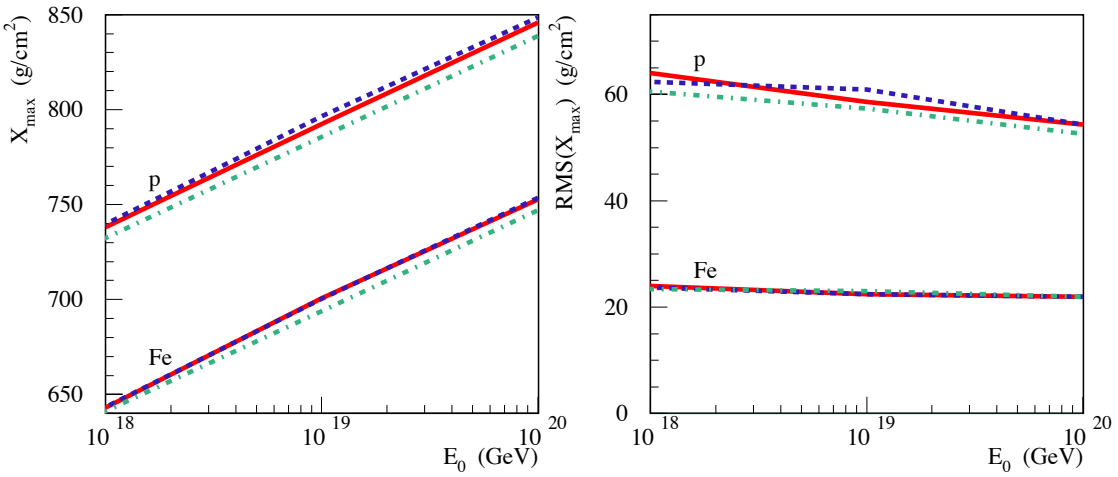

Fig. 3.13: Predictions of $\langle X_{\max} \rangle$ (left) and $\sigma(X_{\max})$ (right) by QGSJET II-04 default (red solid), SD+ (blue dashed), and SD- (green dot-dashed) [36]. Reprinted figures with permission from [S. Ostapchenko, Phys. Rev. D 89, 074009, 2014.] Copyright 2014 by the American Physical Society.

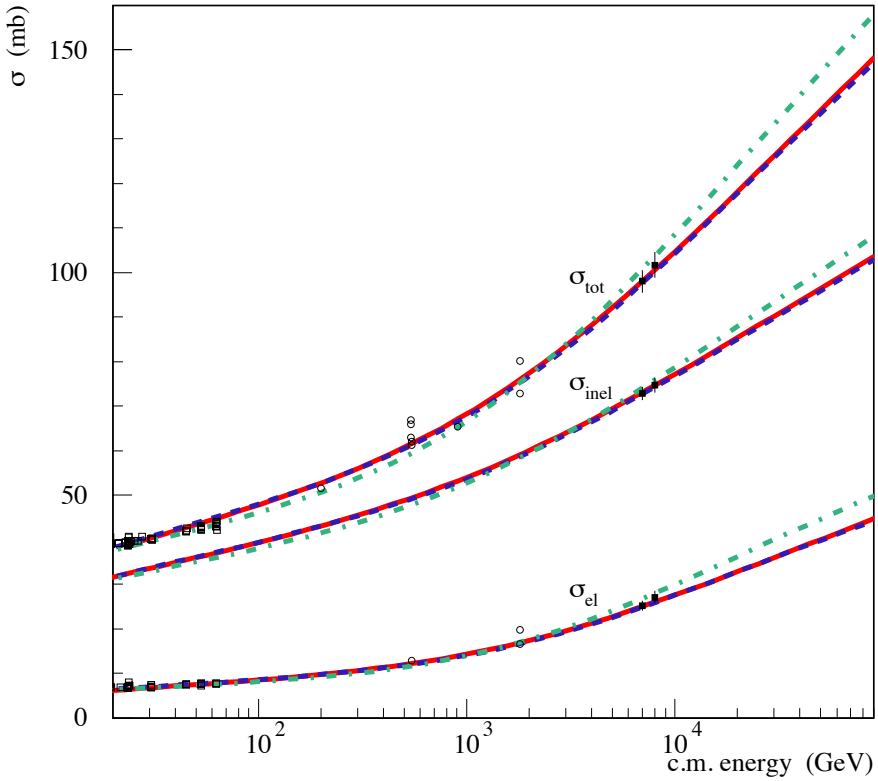

Fig. 3.14: Predictions of total, inelastic, and elastic cross-sections by QGSJET II-04 default (red solid), SD+ (blue dashed), and SD- (green dot-dashed) [36]. Reprinted figures with permission from [S. Ostapchenko, Phys. Rev. D 89, 074009, 2014.] Copyright 2014 by the American Physical Society.

depth of the maximum of the muon productions, and N_μ are considered. Effects based on experimental definitions are discussed in Chap. 5. The conversion of experimental uncertainties in accelerator experiments into the uncertainty in $X_{\max}$ is also performed in Chap. 5.

Chapter 4

Effects of diffractive dissociation on predictions of X_{max} and N_{μ}

4.1 Motivation

As discussed in the previous chapter, each collision type shows a different effect qualitatively. Moreover, diffractive-mass may affect X_{max} and N_{μ}, since elasticity and multiplicity in diffractive dissociation depend on diffractive-mass. However, effects of each collision type and diffractive mass were not estimated separately in the previous studies [36, 39]. In this chapter, effects of collision types and diffractive mass are discussed by focusing on two characteristics; cross-sectional fractions of collision types and diffractive-mass dependencies of cross-sections. Since experimental results of total and inelastic cross-sections measured using Roman-Pot detectors and the optical theorem [64, 59, 60] showed small experimental uncertainty, we focus only on cross-sectional fractions of collision types. For mass-sensitive observable, we focus on X_{max}, N_{μ}, and the depth of maximum of muon productions, X^{μ}_{max}. X^{μ}_{max} was measured by PAO [65]. The interpretations of mass composition estimated from X^{μ}_{max} were heavier than those from X_{max}, whereas the interpretations should be consistent. The effect of diffractive dissociation on this difference in interpretations is also given in this chapter.

4.2 Simulation setup and analysis method

4.2.1 Simulation setup

In this study, simulations were performed using one-dimensional air shower simulation CONEX v6.40 [66]. By using this package, the computation time was reduced significantly compared to three-dimensional simulations. This feature of the CONEX was important for analyses with each collision type since these analyses need high statistics of simulated air showers. 4×10^4 air showers were simulated for each case and each high-energy hadronic interaction model in analyses with 60° zenith angle. EPOS-LHC, QGSJET II-04, and SIBYLL 2.3c were adopted for high-energy hadronic interaction models above 80 GeV in projectile energy. For the low-energy hadronic interaction model, UrQMD [67, 68] was adopted. The depth of maximum of shower development calculated in CONEX was adopted

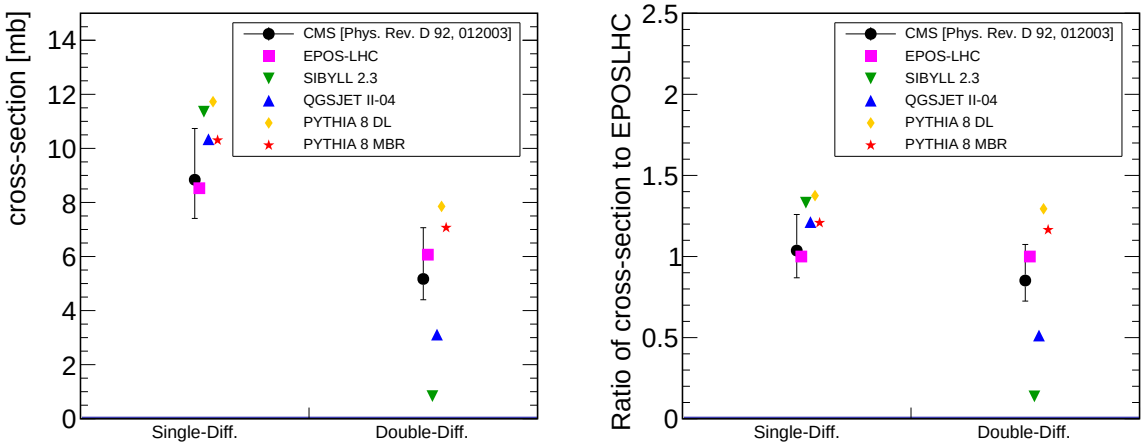

(a) (b)

Fig. 4.1: (left) Comparison of cross-sections of SD and DD between experiments and predictions by hadronic interaction models for CMS results [29]. Error bars are corresponds to experimental uncertainty of each result. Each hadronic interaction model is simulated with CRMC v1.6 [56]. Definitions of SD and DD in Ref. [29] are considered. (right) Ratio of each results to EPOS-LHC.

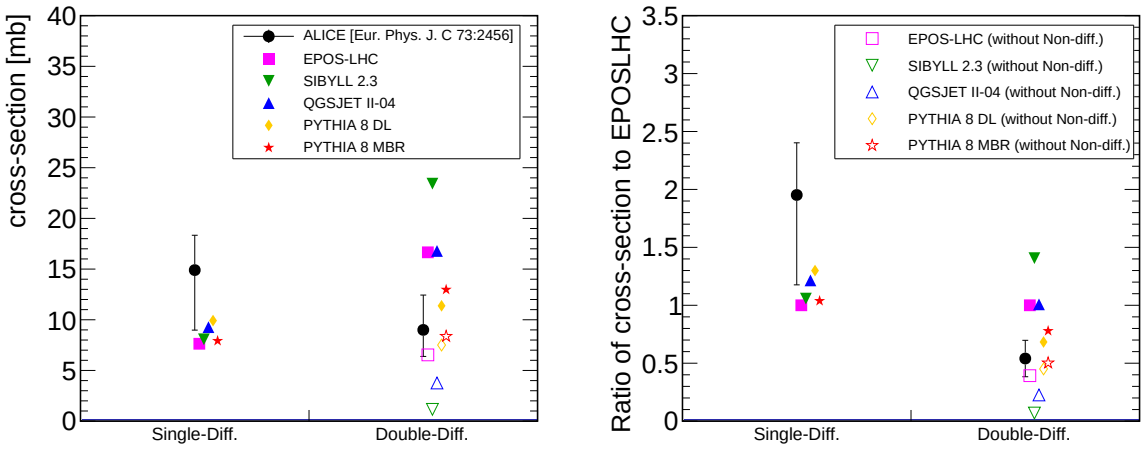

(a) (b)

Fig. 4.2: (left) Comparison of cross-sections of SD and DD between experiments and predictions by hadronic interaction models for ALICE results [30]. Definitions of SD and DD in Ref. [30] are considered. Contamination of ND events is not subtracted in the result for DD cross-sections, thus the results without ND contamination are shown in open markers. (right) The ratio of each results to EPOS-LHC.

as $X_{\max}$. Longitudinal muon production profiles were fitted by the Gaisser-Hillas function [69] to calculate $X^{\mu}_{\max}$. The number of muons at the ground for zenith angle 60° were adopted for the number of muons, N_μ, in this study. Some modifications were applied in CONEX for the analyses in this chapter; information of collision types, diffractive-mass, and the largest rapidity gap at the first inelastic interaction was added in the outputs. The diffractive mass for each event was calculated by separating the dissociation system in each event and calculating the square of the sum of four-momentum. Moreover, simulation samples with modification of a fraction of collision types for whole air showers in CONEX were prepared for analysis. Details of this modification were provided in the next sections.

4.2.2 Analysis method

Analyses in this chapter were performed from the following two points: effects of detailed characteristics with focusing on the first interaction in the air shower and effects of fractions of diffractive dissociation with considering whole air shower development. The effect of each characteristic at the first interaction was estimated from the dependency of $X_{\max}$ or N_μ on the characteristic. These analyses at the first interaction allowed us to understand the effects of detail characteristics of diffractive dissociation comprehensively. Effects of interactions caused by secondary cosmic rays in the air shower were considered by changing a characteristic for the whole air shower.

The following four methods were adopted for the analyses in this chapter;

(A) Effects of collision types on the mean value of $X_{\max}$ or N_μ were analyzed at the first interaction using the mean value categorized by the collision type at the first interaction. The mean value of observable, $\langle O \rangle$, can be calculated from categorized mean values of observable, $\langle O^i \rangle$, and fractions of each collision type, f_i, where i represents a collision type, as

$$\langle O \rangle = \sum_i f_i \langle O^i \rangle. \tag{4.1}$$

Here, O can be $X_{\max}$, $X^{\mu}_{\max}$, and N_μ in the analyses. Fractions of collision types at the first interaction were presented in Fig. 4.3. From this relation, we can calculate the mean value of observable after modification of fractions. In the analysis, we utilized the following four ratios and modify these ratios to change fractions: the ratio of diffractive dissociation to inelastic collisions R_1, the ratio of SD to SD and DD R_2, the ratio of target SD to all SD R_3, and the ratio of CD to all diffractive dissociation R_4. Each fraction can be calculated using these ratios as follows;

$$\begin{aligned} f^{\mathrm{ND}} &= 1 - R_1, \\ f^{\mathrm{projectile\,SD}} &= R_1 R_2 (1 - R_3)(1 - R_4), \\ f^{\mathrm{target\,SD}} &= R_1 R_2 R_3 (1 - R_4), \\ f^{\mathrm{DD}} &= R_1 R_2 (1 - R_4), \\ f^{\mathrm{CD}} &= R_1 R_4. \end{aligned} \tag{4.2}$$

Note that modifications of fractions of CD using R_4 were not performed in the analyses, since no and few CD collisions were predicted by SIBYLL 2.3c and QGSJET II-04, respectively. Due to too small fractions of CD, we cannot discuss the effects of fractions of CD for these two hadronic interaction models.

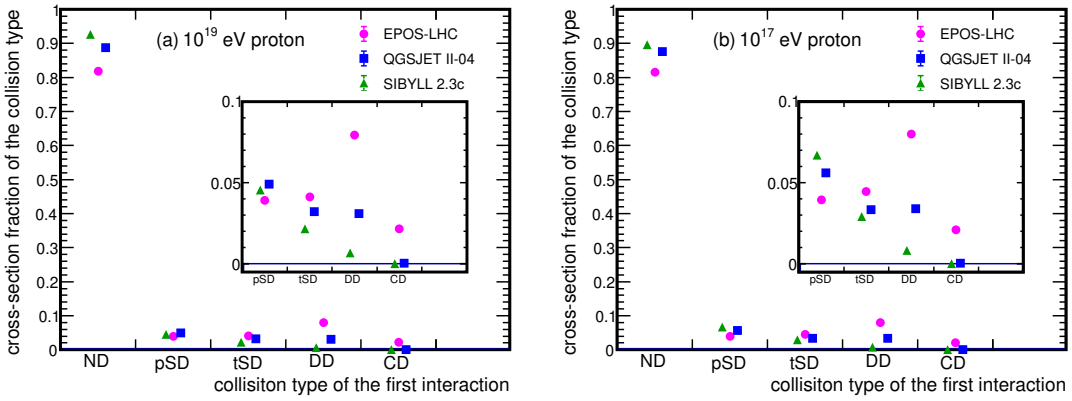

Fig. 4.3: Fractions of collision types at the first interaction for (a) 10^{19} eV and (b) 10^{17} eV proton primary. The figure is reproduced from Ref. [49].

(B) Effects of collision types on the fluctuation of $X_{\max}$, $\sigma(X_{\max})$, were analyzed at the first interaction using distributions of $X_{\max}$ for each category of collision type. Using distributions of $X_{\max}$ for each category normalized by the number of events in each category, we rescaled these distributions by fractions after modifications and added them into one distribution. Using the distribution, we can calculate $\sigma(X_{\max})$ after modification of fractions. Effects of fractions of collision types on $\sigma(X_{\max})$ were estimated by comparing modified $\sigma(X_{\max})$.

(C) Effects of differential cross-sections over diffractive mass, $d\sigma/d\log_{10}\xi$, were analyzed at the first interaction using diffractive mass dependencies of each $X_{\max}$ or N_μ. In the analysis, we divided diffractive mass into bins with 0.5 steps in $\log_{10}(\xi)$. The mean value of observable can be calculated using probability of diffractive-mass in each diffractive-mass bin, P_j, where j represents diffractive-mass bin, and observable in each diffractive-mass bin, O_j, as follows;

$$\langle O \rangle = \sum_j P_j O_j. \tag{4.3}$$

Modified $\langle O \rangle$ were calculated using P_j from three hadronic interaction models. Effects of $d\sigma/d\log_{10}\xi$ were estimated by comparing three modified $\langle O \rangle$.

(D) To consider effects of interactions after the first interaction in an air shower, fractions of diffractive dissociation in inelastic collisions were modified for all interactions with projectile above 10^{15} eV in whole air shower. In this analysis, we only focused on the modification of R_1.

Fractions of diffractive dissociation depend on energy. These energy dependencies were simulated using the CRMC package [56]. Figure 4.4 shows the fractions for proton-Nitrogen and π^+-Nitrogen collisions. The fractions by EPOS-LHC and SIBYLL 2.3c were fitted by the equation $a\log_{10}(E) + b$. Each fitted result was used as the reference fraction $R_1^{\rm Ref}$ in the modification of fractions. $R_1^{\rm Ref}$ from proton-Nitrogen collisions and π^+-Nitrogen collisions were used for baryon-air and meson-air collisions, respectively. Hereafter, $R_1^{\rm Ref}$ from the fitting of EPOS-LHC (SIBYLL 2.3c) was called EPOS-based (SIBYLL-based) $R_1^{\rm Ref}$.

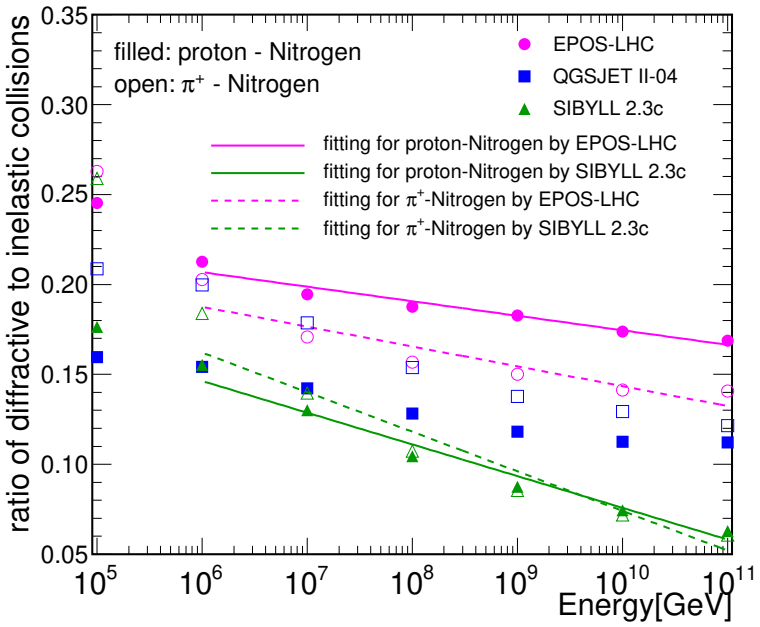

Fig. 4.4: Ratio of diffractive dissociation to inelastic collisions for proton-Nitrogen collisions (filled markers) and π^+-Nitrogen collisions (open markers) calculated by the CMRC v1.7 package. Magenta circles, blue squares, and green triangles show results by EPOS-LHC, QGSJET II-04, and SIBYLL 2.3c, respectively. The figure is reproduced from Ref. [49].

Modifications of simulations were performed using the reference fractions; for each collision with projectile $E > 10^{15}$ eV, a collision type was defined randomly according to R_1^{Ref} before simulating a collision. The collision was simulated by hadronic interaction models repeatedly until the collision type of the simulated collision matches with the collision type defined randomly according to R_1^{Ref}.

4.3 Definitions and uncertainties of diffractive dissociation in this study

The definition of diffractive dissociation depends on each experiment. In experiments, definitions of diffractive dissociation were based on diffractive mass and rapidity gaps. For example, definitions of results by the ALICE experiment [30] were $M_{\mathrm{X}} < 200$ GeV for SD and $\Delta\eta^{\mathrm{gap}} < 3$ for DD. The definition for DD includes some contamination of ND collisions. By contrast, definitions of CMS results [29] are $\xi < 0.05$ for SD and $\Delta\eta < 3$ for DD. Here, $\Delta\eta$ is defined as $\Delta\eta = -\log(M_{\mathrm{X}}^2 M_{\mathrm{Y}}^2/(sm_p^2))$, where M_{X} and M_{Y} are diffractive mass of two dissociation systems, m_p is the mass of proton.

Each hadronic interaction model also has definitions based on the phenomenological model. In this chapter, we utilized the collision type information provided from each hadronic interaction model. For SIBYLL 2.3c, if the number of the interacting nucleon in the nucleus was one and the interaction was diffractive dissociation in the collision-type information, the collision was considered as diffractive dissociation. This definition was based on the definition in Ref. [39, 31]. We discuss effects based on the experimental definitions in Chap. 5.

In the analysis focusing on the first interaction, we adopted the uncertainty region of each characteristic and considered the effects of each characteristic on $X_{\rm max}$ or N_μ with changing the characteristic within the uncertainty region. Uncertainty regions for fractions of diffractive dissociation were estimated based on current experimental results in LHC; we rescaled the fraction using the ratio of experimental data to hadronic interaction models. Experimental uncertainty was propagated to the fraction after rescaling. The uncertainty in the fraction after rescaling was utilized as the uncertainty region. High diffractive-mass regions for $\xi > 0.05$ or $M_{\rm X} > 200$ GeV have not been yet measured. Thus, we utilized predictions by EPOS-LHC for these regions, since the model shows better agreements with experimental data in three hadronic interaction models adopted in the air shower simulation. Details of estimations of the uncertainty regions were given later.

For characteristics without enough experimental results, we used differences among three hadronic interaction models as uncertainty regions. For example, the ratio of target SD to all SD for proton-nucleus or nucleus-nucleus collisions has not been measured at LHC. Thus, uncertainty regions for the ratio were estimated from differences among hadronic interaction models. For $d\sigma/d\log_{10}\xi$, predictions by three hadronic interaction models do not agree with experimental results as shown in Figs. 3.8 and 3.9. Moreover, experimental results of $d\sigma/d\log_{10}\xi$ for low diffractive-mass regions do not exist. Here, we utilized differences of three hadronic interaction models as uncertainty regions of $d\sigma/d\log_{10}\xi$, because SIBYLL 2.3c and EPOS-LHC shows two extreme cases; SIBYLL 2.3c shows flat $d\sigma/d\log_{10}\xi$ without peaks at low diffractive-mass regions, whereas EPOS-LHC shows a very sharp peak at the lowest diffractive-mass region. In this way, uncertainty regions of $d\sigma/d\log_{10}\xi$ may be overestimated, since two extreme cases were considered.

The uncertainty region for the fractions of diffractive dissociation were calculated as follows;

(i) Ratios of experimental results to predictions by EPOS-LHC and its uncertainty, $r^{+\delta r}_{-\delta r}$, were calculated. The ratios are illustrated in Figs. 4.1(b) and 4.2(b). Note that the result for DD by the ALICE experiment [30] was ignored because contamination of ND events were expected. Contamination of ND events is considered in Chap. 5.

(ii) Events categorized by collision types at the first interactions were additionally categorized by the experimental definitions. Results of additional categorization using CMS and ALICE definitions are presented in Tab. 4.3. Ratios r were applied to the fractions where experimental definitions are satisfied. The fraction of SD and DD was calculated from two fractions for low and high diffractive mass regions: the fraction modified by the ratio r and the fraction predicted by EPOS-LHC for $\xi > 0.05$ or $M_{\rm X} > 200$ GeV.

(iii) The upper and lower limit of fractions of SD and DD were calculated by applying $r\pm\delta r$ instead of r in step (ii). Results after applying r and its uncertainty are presented in Tab. 4.1 and 4.2. Note that the ratio for SD from experimental results in proton-proton collisions was applied for the sum of fractions of projectile SD and target SD in proton-air nucleus collisions.

(iv) The uncertainty regions for R_1 and R_2 were calculated using propagations of uncertainty for SD and DD calculated in step (ii) and (iii). Results of R_1 and R_2 are presented in Tab. 4.4. Note that the fraction of CD and its error calculated by the average and differences among hadronic interaction models was 0.0105 ± 0.0105 and

Definitions	SD $\xi < 0.05$	DD $\Delta\eta < 3$
ratio r	$1.04^{+0.22}_{-0.17}$	$0.85^{+0.28}_{-0.13}$
EPOS-LHC 10^{17} eV	$0.086^{+0.013}_{-0.010}$	$0.075^{+0.010}_{-0.004}$
EPOS-LHC 10^{19} eV	$0.082^{+0.011}_{-0.009}$	$0.074^{+0.010}_{-0.004}$

Table 4.1: The center values and uncertainty regions of SD and DD for the first interaction in air showers estimated from results by the CMS experiment [29]. SD includes projectile SD and target SD.

Definitions	SD $M_{\mathrm{X}} < 200$ GeV
ratio r	$1.95^{+0.45}_{-0.78}$
EPOS-LHC 10^{17} eV	$0.128^{+0.021}_{-0.036}$
EPOS-LHC 10^{19} eV	$0.122^{+0.020}_{-0.034}$

Table 4.2: The center values and uncertainty regions of SD for the first interaction in air showers estimated from results by the ALICE experiment [30].

0.0108 ± 0.0108 for 10^{17} eV and 10^{19} eV, respectively. The uncertainty was also considered in R_1.

Note that experimental results by the CMS and the ALICE experiments [29, 30] were measured for proton-proton collisions with $\sqrt{s} = 7$ TeV. This energy roughly corresponds to collisions between 2.6×10^{16} eV proton and proton at rest, whereas collisions between 10^{17} eV proton or 10^{19} eV proton and air nucleus in the air shower were considered in the analyses. In the estimation of uncertainty regions, we applied ratios in Figs. 4.1(b) and 4.2(b) without considering energy dependence.

	projectile SD	target SD	DD
EPOS-LHC, 10^{17} eV			
CMS definition	0.630	0.745	0.435
ALICE definition	0.502	0.609	0.647
EPOS-LHC, 10^{19} eV			
CMS definition	0.568	0.701	0.433
ALICE definition	0.491	0.594	0.681

Table 4.3: Fractions of events which pass the CMS or ALICE definitions for each category for collisions of a 10^{19} eV proton or a 10^{17} eV proton with an air nucleus at rest. The CMS and ALICE definitions for cross-section measurements were described in Sec. 3.3.2 and 3.3.3, respectively.

	R_1	R_2
	10^{17} eV	
From CMS results	$0.171^{+0.019}_{-0.015}$	$0.534^{+0.050}_{-0.032}$
From ALICE results	$0.219^{+0.024}_{-0.038}$	$0.616^{+0.039}_{-0.067}$
uncertainty region for analyses	0.156 - 0.243	0.502 - 0.655
	10^{19} eV	
From CMS results	$0.167^{+0.018}_{-0.014}$	$0.526^{+0.047}_{-0.030}$
From ALICE results	$0.212^{+0.022}_{-0.036}$	$0.606^{+0.039}_{-0.066}$
uncertainty region for analyses	0.153 - 0.235	0.496 - 0.645

Table 4.4: The ratios R_1 and R_2 with their uncertainty regions estimated from results by the CMS and the ALICE experiments [29, 30]. Uncertainty regions used for this analysis in this chapter are also shown in the "for analysis" row.

4.4 Effects on $\langle X_{\mathrm{max}} \rangle$

Predictions of $\langle X_{\mathrm{max}} \rangle$ depends on collision types and diffractive mass as illustrated in Figs. 4.5 (a) and 4.6. $\langle X_{\mathrm{max}} \rangle$ for the categories of diffractive dissociation shows a larger value than that for ND collisions; $\langle X_{\mathrm{max}} \rangle$ for the category of target SD and CD dissociation typically shows approximately 50 g/cm^2 larger than that for the category of ND collisions, because the projectile proton is intact at the first interaction and additionally travels one interaction length, typically ~ 50 g/cm^2 for 10^{19} eV protons, before another interaction. $\langle X_{\mathrm{max}} \rangle$ for the category of projectile SD and DD shows a larger value than that for the category of ND collisions but a smaller value than that for target SD, because the projectile proton dissociates in these collisions and high elasticity and low multiplicity are expected at the first interaction. Diffractive dissociation with lower diffractive mass is characterized by higher elasticity than that with higher diffractive mass, thus $\langle X_{\mathrm{max}} \rangle$ become larger as diffractive mass become smaller as presented in Fig. 4.6. Note that events with projectile SD at the first interaction are selected for the calculation of diffractive-mass dependencies.

Effects of collision types at the first interactions are analyzed with method A in Sec. 4.2.2. Figures 4.7(a), (b), and (c) illustrate $\langle X_{\mathrm{max}} \rangle$ with modifying R_1, R_2, and R_3, respectively, for 10^{19} eV proton primary (upper panel) and 10^{17} eV proton primary (middle panel). Results are calculated for three hadronic interaction models EPOS-LHC (magenta), QGSJET II-04 (blue), and SIBYLL 2.3c (green). Black points in each panel correspond to the predictions by these hadronic interaction models. Orange arrow represents the uncertainty range of each ratio estimated in Sec. 4.3. The bottom panel show the differences from the model original value, $\Delta\langle X_{\mathrm{max}} \rangle$, defined as,

$$\Delta\langle X_{\mathrm{max}} \rangle = \langle X_{\mathrm{max}}^{\mathrm{Modified}} \rangle - \langle X_{\mathrm{max}}^{\mathrm{original}} \rangle, \tag{4.4}$$

where $\langle X_{\mathrm{max}}^{\mathrm{Modified}} \rangle$ and $\langle X_{\mathrm{max}}^{\mathrm{Original}} \rangle$ are modified and original value of $\langle X_{\mathrm{max}} \rangle$, respectively. The size of effects when ratios are modified within the uncertainty regions for 10^{19} eV primary at the first interaction are 2.8-3.8 g/cm^2 for R_1, 0.03-0.14 g/cm^2 for R_2, and 0.04-0.19 g/cm^2 for R_3. Those for 10^{17} eV primary are 3.0-4.0 g/cm^2 for R_1, 0.16-0.28 g/cm^2 for R_2, and 0.14-0.57 g/cm^2 for R_3. Note that statistical error in this analysis is ± 0.3 g/cm^2, thus effects of R_2 and R_3 for 10^{19} eV primary are consistent to zero within statistical errors.

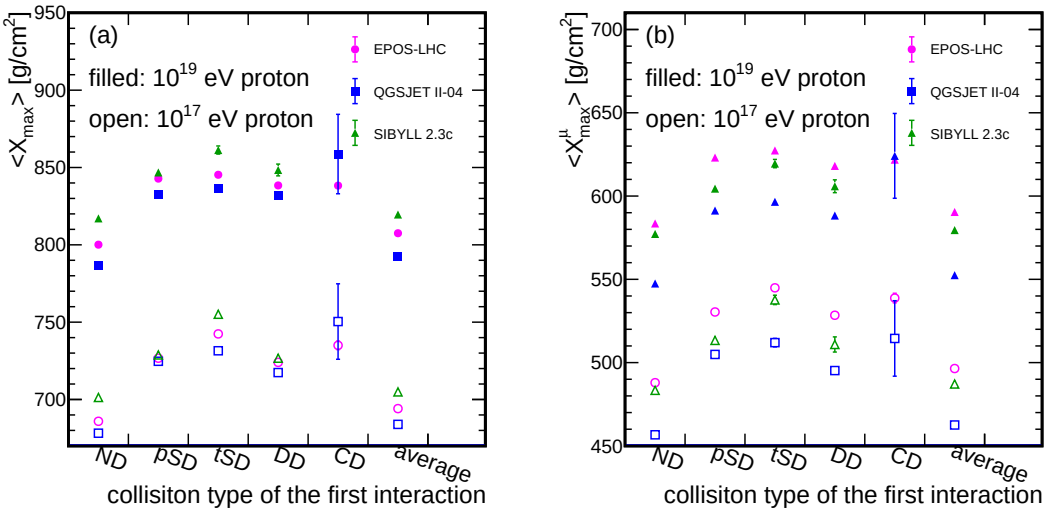

Fig. 4.5: (a) $\langle X_{\mathrm{max}} \rangle$ and (b) $\langle X^{\mu}_{\mathrm{max}} \rangle$ categorized by collision types at the first interaction. These figures are reproduced from Ref. [49].

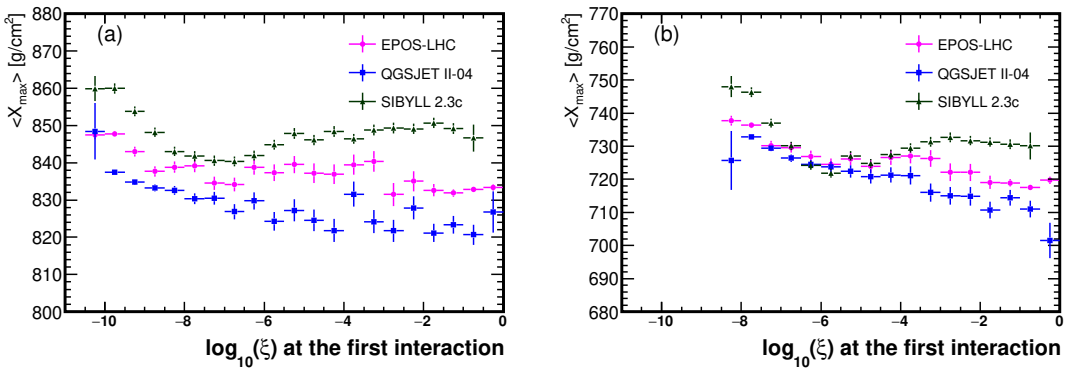

Fig. 4.6: Diffractive-mass dependencies of $\langle X_{\mathrm{max}} \rangle$ for (a) 10^{19} eV and (b) 10^{17} eV proton primary. These figures are reproduced from Ref. [49].

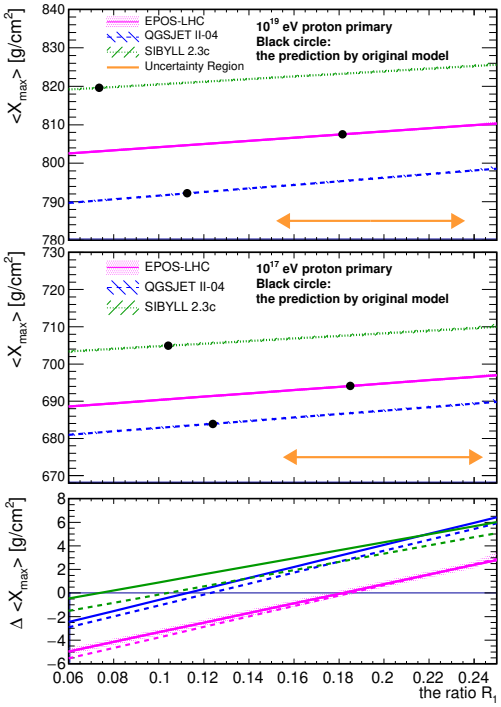

(a) R_1 dependence of $\langle X_{\mathrm{max}}^{\mathrm{modified}} \rangle$

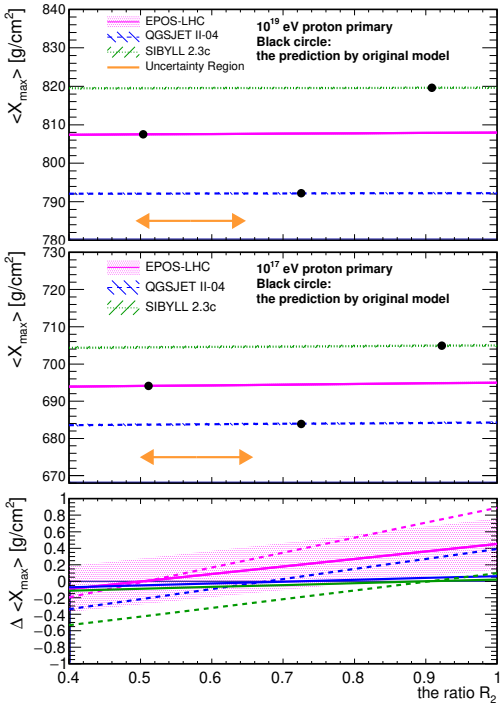

(b) R_2 dependence of $\langle X_{\mathrm{max}}^{\mathrm{modified}} \rangle$

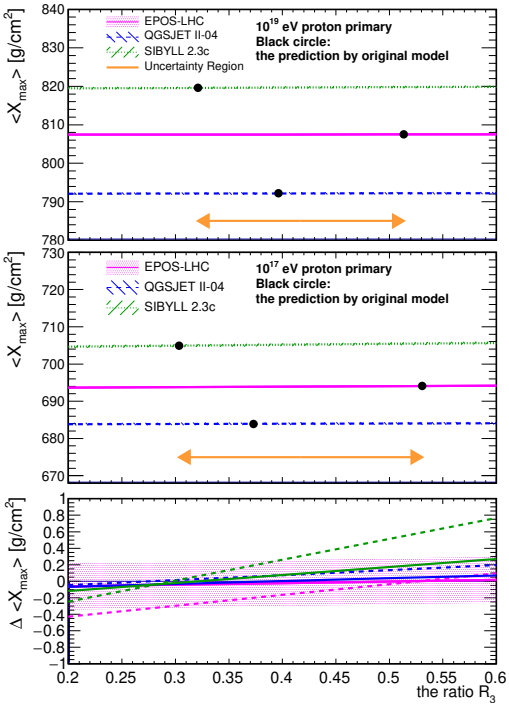

(c) R_3 dependence of $\langle X_{\mathrm{max}}^{\mathrm{modified}} \rangle$

Fig. 4.7: Fraction dependencies of $\langle X_{\mathrm{max}} \rangle$ for (a) R_1, (b) R_2, and (c) R_3. Top and middle panel for each figure show the results for 10^{19} eV and 10^{17} eV proton primary, respectively. Bottom panel of each figure shows difference $\Delta\langle X_{\mathrm{max}} \rangle$ for 10^{19} eV (solid lines) and 10^{17} eV (dashed lines) primary. Orange arrays represent the uncertainty region estimated in Sec. 4.3. These figures are reproduced with modifications from Ref. [49].

	Modified $\langle X_{\rm max}^{\rm projectile\ SD}\rangle$ [g/cm^2] model for probability of diffractive-mass				the size of effects
model	original	EPOS-LHC	QGSJET II-04	SIBYLL 2.3c	
EPOS-LHC	838.0± 0.3	838.0 ± 0.3	841.7 ± 0.4	837.6 ± 0.5	4.1± 0.7
QGSJET II-04	833.3 ± 0.3	829.3 ± 1.0	833.3 ± 0.3	828.2 ± 0.6	5.1 ± 0.7
SIBYLL 2.3c	847.4 ± 0.3	850.3 ±0.7	851.9 ± 0.6	847.4 ± 0.3	4.4 ± 0.7

Table 4.5: Modified $\langle X_{\rm max}\rangle$ with changing probability of diffractive mass for three probability by hadronic interaction models. Errors are statistical errors of estimations. Primary cosmic rays are proton with 10^{19} eV.

Effects of diffractive mass at the first interactions are analyzed with method C in Sec. 4.2.2. Results of modified $\langle X_{\rm max}\rangle$ for the category of projectile SD, $\langle X_{\rm max}^{\rm projectile\ SD}\rangle$, and the size of effects are shown in Tab. 4.5. By changing probability of diffractive mass, $\langle X_{\rm max}^{\rm projectile\ SD}\rangle$ changes 4.1-5.1 g/cm^2, whereas diffractive mass only affects the collision types with dissociation of a projectile proton, namely projectile SD and DD. The fraction of these cases is 5-12 % in inelastic collisions. Thus, effects of probability of diffractive mass on $\langle X_{\rm max}\rangle$ are approximately 0.6 g/cm^2 at the first interaction.

The effects of the fraction of diffractive dissociation in inelastic collisions are discussed for whole air showers with focusing on effects of R_1 to consider effects in collisions of secondary particles. R_1 is modified for all collisions with projectile energy larger than 10^{15} eV in the whole air shower using the method D in Sec. 4.2.2. The results of this modification are summarized in Tab. 4.6. The effect with modification for whole air shower using SIBYLL-based $R_1^{\rm Ref}$ is -4.2 g/cm^2 for EPOS-LHC and that using EPOS-based $R_1^{\rm Ref}$ is 8.9 g/cm^2 for SIBYLL 2.3c.

Systematic uncertainty of this method can be estimated from the result of EPOS-LHC with modification by EPOS-based $R_1^{\rm Ref}$ and that of SIBYLL 2.3c with modification by SIBYLL-based $R_1^{\rm Ref}$. From differences of $\langle X_{\rm max}\rangle$ between these cases, the sizes of the systematic uncertainty of this method are 2.0 g/cm^2 and 0.9 g/cm^2 for EPOS-based $R_1^{\rm Ref}$ and SIBYLL-based $R_1^{\rm Ref}$, respectively. Since the results with modification by EPOS-based and SIBYLL-based $R_1^{\rm Ref}$ are larger than the original values of EPOS-LHC and SIBYLL 2.3c, respectively, results estimated in method D can be overestimated within the size of systematic uncertainty. It means that the systematic uncertainties are -2.0 g/cm^2 and -0.9 g/cm^2 for 8.9 g/cm^2 and -4.2 g/cm^2, respectively.

By comparing results using method D and effects of R_1 at the first interaction, we can understand the ratio of effects for whole air showers to at the first interaction. From Fig. 4.7, for 10^{19} eV primary, the effect of modification of R_1 from the original value of EPOS-LHC to predictions by SIBYLL 2.3c at the first interaction is -4.4 ± 0.3 g/cm^2 for EPOS-LHC. That from the original value of SIBYLL 2.3c to predictions by EPOS-LHC at the first interaction is 3.7 ± 0.3 g/cm^2 for SIBYLL 2.3c. From the comparison between -4.2 ± 0.4 g/cm^2 and -4.4 ± 0.3 g/cm^2, the effect for the whole air shower including collisions of secondary particles is 0.95 times larger than that at the first interaction for the EPOS-LHC case. From the comparison between 8.9 ± 0.4 g/cm^2 and 3.7 ± 0.3 g/cm^2, the effect for the whole air shower is 2.4 times larger than at the first interaction for the SIBYLL 2.3c case. Considering statistical uncertainty of each value and systematic uncertainty in the method D, the ratios of effects are $2.4 \pm 0.4({\rm stat.})^{+0.0}_{-0.5}({\rm syst.})$ and $0.95 \pm 0.2({\rm stat.})^{+0.2}_{-0.0}({\rm syst.})$ for SIBYLL 2.3c and

interaction model	$\langle X_{\rm max}\rangle$ [g/cm^2] original	with modification EPOS-based $R_1^{\rm Ref}$	difference	SIBYLL-based $R_1^{\rm Ref}$	difference
EPOS-LHC	807.5 ± 0.3	809.5 ± 0.4	2.0 ± 0.4	803.3 ± 0.3	-4.2 ± 0.4
QGSJET II-04	792.2 ± 0.3	796.6 ± 0.3	4.4 ± 0.4	788.5 ± 0.3	-3.7 ± 0.4
SIBYLL 2.3c	819.6 ± 0.3	828.6 ± 0.3	8.9 ± 0.4	820.5 ± 0.3	0.9 ± 0.4
difference between models	27.4 ± 0.4	31.9 ± 0.5		32.0 ± 0.4	

Table 4.6: Results of $\langle X_{\rm max}\rangle$ with modifications for whole air shower. Errors are statistical errors. Primary cosmic rays are proton with 10^{19} eV.

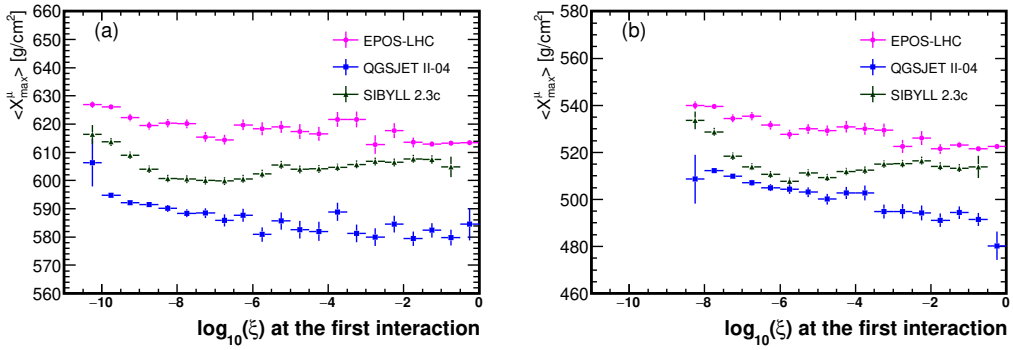

Fig. 4.8: Diffractive-mass dependencies for $\langle X^{\mu}_{\rm max}\rangle$ for (a) 10^{19} eV and (b) 10^{17} eV proton primary. These figures are reproduced from Ref. [49].

EPOS-LHC cases, respectively.

From this result, $0.95 - 2.4$ times larger effects are expected for effects estimated at the first interaction. By considering 2.4 times larger effects for effects of R_1 at the first interaction, which are 2.8-3.8 g/cm^2, the maximum size of the effect of R_1 is 6.7-9.1 g/cm^2. Effects of R_1, R_2, and diffractive mass are less than 1.5 g/cm^2 at maximum and negligible.

4.5 Effects on $\langle X^{\mu}_{\rm max}\rangle$

Predictions of $\langle X^{\mu}_{\rm max}\rangle$ depends on collision types and diffractive mass as presented in Figs. 4.5(b) and 4.8. Dependencies are similar with the case of $\langle X_{\rm max}\rangle$; categories of diffractive dissociation show larger $\langle X^{\mu}_{\rm max}\rangle$ than ND collisions. Diffractive dissociation with lower diffractive mass show larger $\langle X^{\mu}_{\rm max}\rangle$. In this section, effects of fractions of categories and diffractive mass are estimated as we performed in Sec. 4.4.

To understand the effects of collision types and diffractive mass at the first interactions, we apply the analysis method A and C in Sec. 4.2.2 to $\langle X^{\mu}_{\rm max}\rangle$ as in the previous section. Figures 4.9 show $\langle X^{\mu,\rm modified}_{\rm max}\rangle$ with changing ratios R_1, R_2, and R_3 in the uncertainty range defined in Sec. 4.3. The size of effects when ratios are modified within the uncertainty region at the first interaction are 2.6-3.7 g/cm^2 for R_1, 0.04-0.17 g/cm^2 for R_2, and 0.07-0.19 g/cm^2 for R_3 for 10^{19} eV primary. Those for 10^{17} eV primary are 3.18-4.14 g/cm^2 for R_1, 0.16-0.24 g/cm^2 for R_2, and 0.12-0.45 g/cm^2 for R_3. Statistical errors for this estimation is ± 0.3g/cm^2, thus effects of R_2 and R_3 for 10^{19} eV primary are consistent to zero. Effects of the probability of diffractive mass are estimated with method C in Sec. 4.2.2

	$\langle X_{\rm max}\rangle$ [g/cm^2]	Modified $\langle X^{\mu,\text{projectile SD}}_{\rm max}\rangle$ [g/cm^2] model for probability of diffractive-mass			the size of effects
model	original	EPOS-LHC	QGSJET II-04	SIBYLL 2.3c	
EPOS-LHC	618.2± 0.3	618.2 ± 0.3	621.7 ± 0.5	618.4 ± 0.5	3.5± 0.6
QGSJET II-04	590.9 ± 0.3	587.4 ± 1.1	591.0 ± 0.3	586.2 ± 0.6	4.8 ± 0.7
SIBYLL 2.3c	604.8 ± 0.3	607.1 ±0.7	607.6 ± 0.6	604.8 ± 0.3	2.8 ± 0.7

Table 4.7: Modified $\langle X^{\mu}_{\rm max}\rangle$ with changing probability of diffractive mass for three probability by hadronic interaction models. Errors are statistical errors of estimations. Primary cosmic rays are proton with 10^{19} eV.

and results are presented in Tab. 4.7. The size of effects is 2.8-4.8 g/cm^2 for events with projectile SD at the first interaction. By considering the fraction of projectile SD and DD, effects of $\langle X^{\mu}_{\rm max}\rangle$ at the first interaction are less than 0.6 g/cm^2.

Effects of the secondary interactions are discussed by changing R_1 for whole air showers using method D in Sec. 4.2.2. Results are presented in Tab. 4.8. The result for EPOS-LHC with modification using SIBYLL-based $R_1^{\rm Ref}$ is -4.4 g/cm^2 and that for SIBYLL 2.3c using EPOS-based $R_1^{\rm Ref}$ is 9.4 g/cm^2. Systematic uncertainties of this estimation are -0.9 g/cm^2 for EPOS-LHC and -1.0 g/cm^2 for SIBYLL 2.3c. Systematic uncertainties are estimated from differences between results of EPOS-LHC (SIBYLL 2.3c) and EPOS-LHC (SIBYLL 2.3c) with modification using EPOS-based (SIBYLL-based) $R_1^{\rm Ref}$.

By comparing results using method D and effects of R_1 at the first interaction, we can understand the ratio of effects for whole air showers to at the first interaction. From the estimation at the first interaction, the effect of R_1 when R_1 is changed from a prediction by EPOS-LHC to that by SIBYLL 2.3c is -4.1 ± 0.3 g/cm^2 for EPOS-LHC. For SIBYLL 2.3c, that when R_1 is changed from a prediction by SIBYLL 2.3c to that by EPOS-LHC is 3.4 ± 0.3 g/cm^2. From the comparison between -4.4 ± 0.4 g/cm^2 and -4.1 ± 0.3 g/cm^2 or 9.4 ± 0.4 g/cm^2 and 3.4 ± 0.3 g/cm^2, the ratio of effects for whole air showers to at the first interaction is approximately 1.1 for EPOS-LHC and 2.8 for SIBYLL 2.3c. Thus, effects for the whole air shower are 1.1-2.8 times larger than that at the first interaction. Considering the statistical uncertainty of each value and the systematic uncertainty for the results in method D, the ratios of effects are $2.8\pm0.5(\text{stat.})^{+0.0}_{-0.3}(\text{syst.})$ and $1.1\pm0.2(\text{stat.})^{+0.2}_{-0.0}(\text{syst.})$ for SIBYLL 2.3c and EPOS-LHC cases, respectively.

If 2.8 times larger effects are considered for 10^{19} eV primary, effects of R_2, R_3, and diffractive mass are less than 2 g/cm^2. By contrast, the maximum size of the effect of R_1 is 7.3-10.4 g/cm^2 with considering 2.8 times larger effects for at the first interaction, which are 2.6-3.7 g/cm^2. In consequence, effects of R_1 show substantially large effects, whereas other characteristics show minor effects.

From the discussion above, the size of effects of R_1 on $\langle X_{\rm max}\rangle$ and $\langle X^{\mu}_{\rm max}\rangle$ are similar. It means that diffractive dissociation cannot solve the inconsistent interpretations of mass composition from $X_{\rm max}$ and $X^{\mu}_{\rm max}$.

4.6 Effects on $\sigma(X_{\rm max})$

Fluctuations of $X_{\rm max}$ are caused by the fluctuation of the depth of the first interaction and fluctuations of air showers induced by particles produced at the first interaction. If the mul-

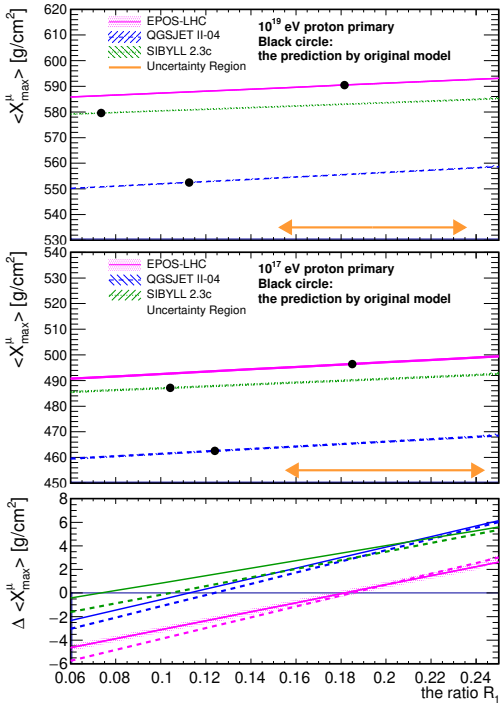

(a) R_1 dependence of $\langle X^{\mu,\mathrm{modified}}_{\mathrm{max}} \rangle$

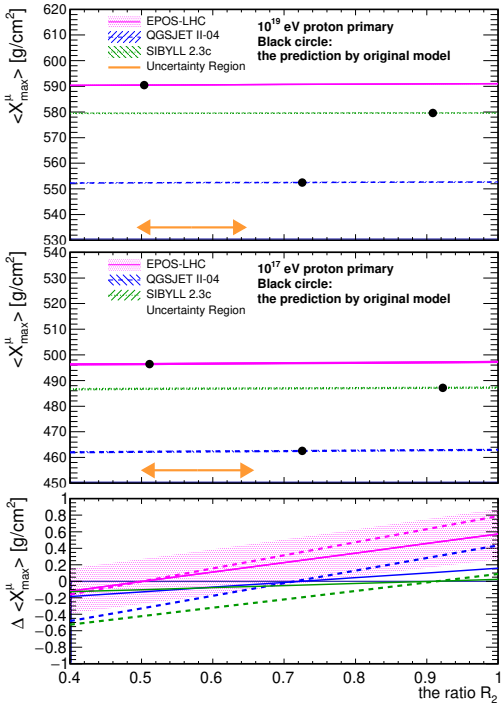

(b) R_2 dependence of $\langle X^{\mu,\mathrm{modified}}_{\mathrm{max}} \rangle$

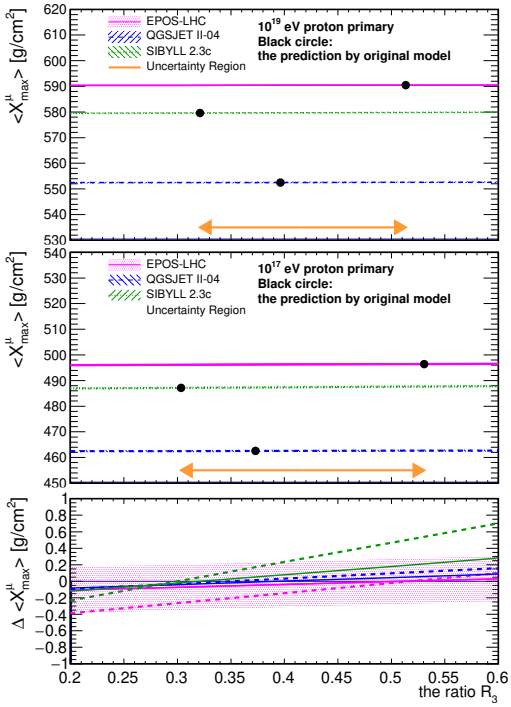

(c) R_3 dependence of $\langle X^{\mu,\mathrm{modified}}_{\mathrm{max}} \rangle$

Fig. 4.9: Fraction dependencies of $\langle X^{\mu}_{\mathrm{max}} \rangle$ for (a) R_1, (b) R_2, and (c) R_3. Top and middle panel for each figure show the results for 10^{19} eV and 10^{17} eV proton primary, respectively. Bottom panel of each figure shows difference $\Delta\langle X^{\mu}_{\mathrm{max}} \rangle$ for 10^{19} eV (solid lines) and 10^{17} eV (dashed lines) primary. Orange arrays represent the uncertainty region estimated in Sec. 4.3. These figures are reproduced with modifications from Ref. [49].

interaction model	$\langle X^{\mu}_{\mathrm{max}} \rangle$ [g/cm^2] original	with modification EPOS-based R_1^{Ref}	difference	with modification SIBYLL-based R_1^{Ref}	difference
EPOS-LHC	590.5 ± 0.3	591.4 ± 0.4	0.9 ± 0.4	586.1 ± 0.3	-4.4 ± 0.4
QGSJET II-04	552.5 ± 0.3	558.6 ± 0.3	6.1 ± 0.4	548.5 ± 0.3	-4.0 ± 0.4
SIBYLL 2.3c	579.6 ± 0.3	589.0 ± 0.3	9.4 ± 0.4	580.6 ± 0.3	1.0 ± 0.4
difference between models	38.0 ± 0.4	32.8 ± 0.5		37.6 ± 0.4	

Table 4.8: Results of $\langle X^{\mu}_{\mathrm{max}} \rangle$ with modifications for whole air shower. Errors are statistical errors. Primary cosmic rays are proton with 10^{19} eV.

	ND	projectile SD	target SD	DD	CD	inclusive
EPOS-LHC	53.8	65.3	69.5	61.8	66.0	58.2
QGSJET II-04	57.1	66.5	76.3	66.8	92.6	60.5
SIBYLL 2.3c	60.5	64.2	76.9	62.6		61.8

Table 4.9: $\sigma(X_{\mathrm{max}})$ with categorization at the first interaction for ND, projectile SD, target SD, DD, CD, and without categorization (inclusive). Primary cosmic rays are protons with 10^{19} eV.

tiplicity of the first interaction is high, many air showers are produced by particles produced at the interaction, therefore fluctuations are suppressed. Diffractive dissociation is characterized by low multiplicity, thus $\sigma(X_{\mathrm{max}})$ for the case with diffractive dissociation at the first interaction is larger than ND collisions at the first interaction, as presented in Tab. 4.9. To compare $\sigma(X_{\mathrm{max}})$ for each category and $\sigma(X_{\mathrm{max}})$ without categorization, it is, however, necessary to consider $\langle X_{\mathrm{max}} \rangle$. If $\sigma(X_{\mathrm{max}})$ of the distribution is calculated from sum of two distributions with different $\rangle X_{\mathrm{max}} \langle$, $\sigma(X_{\mathrm{max}})$ becomes larger due to the difference of $\langle X_{\mathrm{max}} \rangle$. In this section, we discuss the effect of the ratio R_1 on $\sigma(X_{\mathrm{max}})$ using the method B in Sec. 4.2.2, since the ratio shows the largest effect on $\langle X_{\mathrm{max}} \rangle$.

Effects of uncertainty in fractions of diffractive dissociation on $\sigma(X_{\mathrm{max}})$ are presented in Tab. 4.10. By comparing modified $\sigma(X_{\mathrm{max}})$ with R_1 at the upper and the lower limit of the uncertainty range, the size of the effects of R_1 is 1.6 g/cm^2 for EPOS-LHC, 1.9 g/cm^2 for QGSJET II-04, and 1.1 g/cm^2 for SIBYLL 2.3c. Differences of predictions between hadronic interaction models in $\sigma(X_{\mathrm{max}})$ are 3.6 g/cm^2, thus the effect of R_1 at the first interaction is half of differences between hadronic interaction models. Meanwhile, the difference of $\sigma(X_{\mathrm{max}})$ between proton-induced showers and helium induced showers is approximately 20 g/cm^2. Therefore, this effect is negligible for interpretations of mass composition.

interaction model	$\sigma(X_{\mathrm{max}})$[g/cm^2] with modification uncertainty upper	lower	the size of effects [g/cm^2]
EPOS-LHC	59.2	57.6	1.9
QGSJET II-04	63.4	61.5	1.6
SIBYLL 2.3c	64.1	63.0	1.1

Table 4.10: $\sigma(X_{\mathrm{max}})$ with modification of R_1 within the uncertainty range defined in Tab. 4.4.

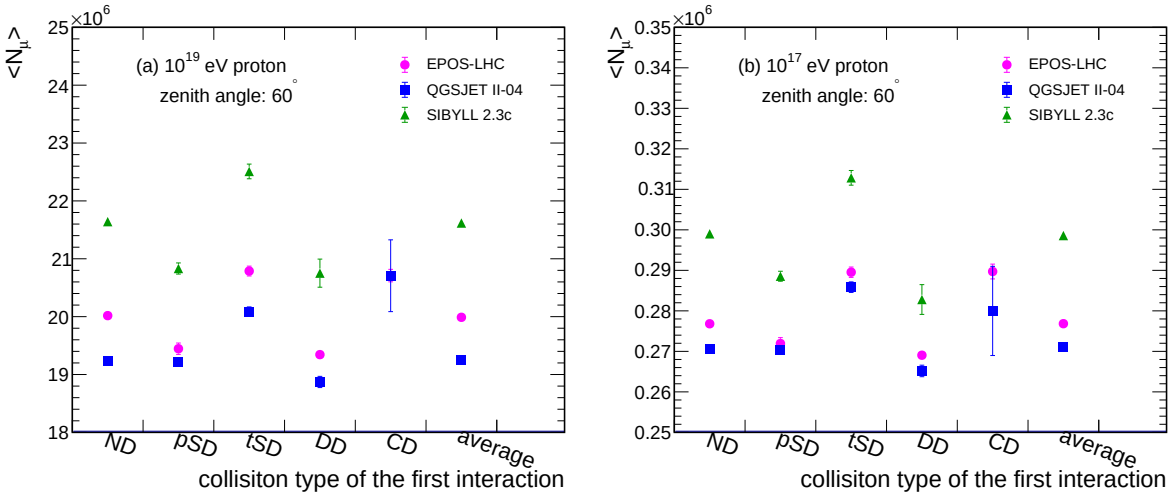

Fig. 4.10: N_μ with categorization by collision types at the first interaction for (a) 10^{19} eV and (b) 10^{17} eV. These figures are reproduced from Ref. [49].

4.7 Effects on N_μ

Predictions of N_μ depends on collision types and diffractive mass. These dependencies show different characteristics from $\langle X_{\rm max} \rangle$ and $\langle X^\mu_{\rm max} \rangle$ as illustrated in Figs. 4.10 and 4.11. Figure 4.12 illustrates profiles of longitudinal developments of the number of muons. As illustrated in Fig. 4.10, N_μ with projectile SD and DD at the first interaction show smaller values than that with ND. Moreover, N_μ with target SD and CD show larger values than that with ND. Qualitative explanations for these features are as follows; if the first interaction is target SD or CD, projectile proton additional travels for typically one interaction length. The shower development is shifted to one interaction length deeper parts of the atmosphere than the development with ND collisions at the first interaction. The feature is illustrated in yellow dash-dotted and cyan dash-three-dotted lines of Figure 4.12 for projectile SD and DD, respectively. Muons are typically detected for inclined showers. It means that muons are measured at much after the depth of the maximum of the number of muons. Therefore, N_μ at detectors becomes larger for these collision types. If the first interaction is projectile SD or DD, a low multiplicity collision happens at the first interaction. Multiplicity affects the number of muons as discussed in Sec. 2.1. The feature of projectile SD or DD makes N_μ smaller than the case with ND collisions at the first interaction, as illustrated in magenta dotted and green dash-two-dotted lines of Figure 4.12.

From Fig. 4.11, diffractive-mass dependencies vary between hadronic interaction models. SIBYLL 2.3c shows a strange dip structure at the low diffractive-mass region, whereas the other two models show small diffractive-mass dependencies. These dependencies may be connected with particle productions because the number of muons is sensitive to multiplicity.

Effects of fractions of collision types and diffractive-mass spectrum are analyzed using methods A and C in Sec. 4.2.2. Results of N_μ with modification of R_1, R_2, and R_3 are illustrated in Fig. 4.13(a), (b), and (c), respectively. Difference of N_μ from the original

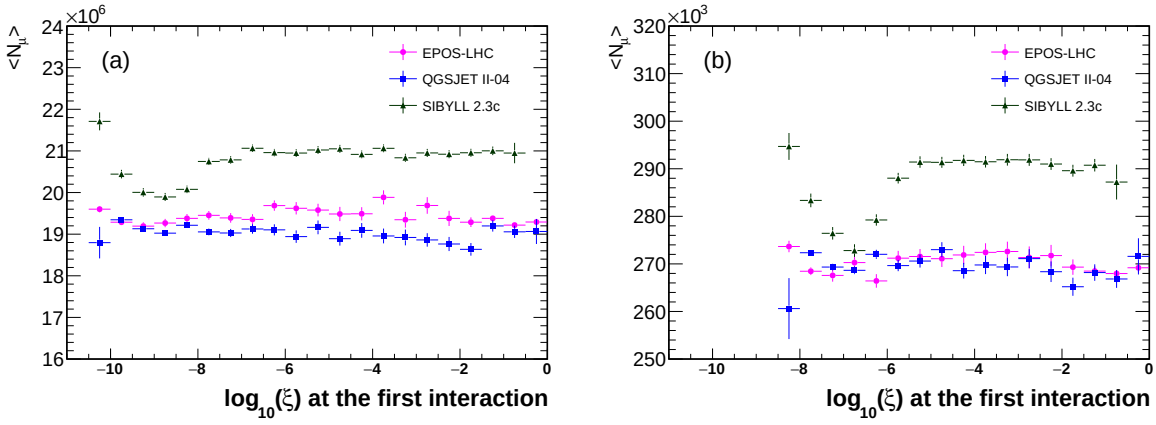

Fig. 4.11: Diffractive-mass dependencies of N_μ for (a) 10^{19} eV and (b) 10^{17} eV proton primary. These figures are reproduced from Ref. [49].

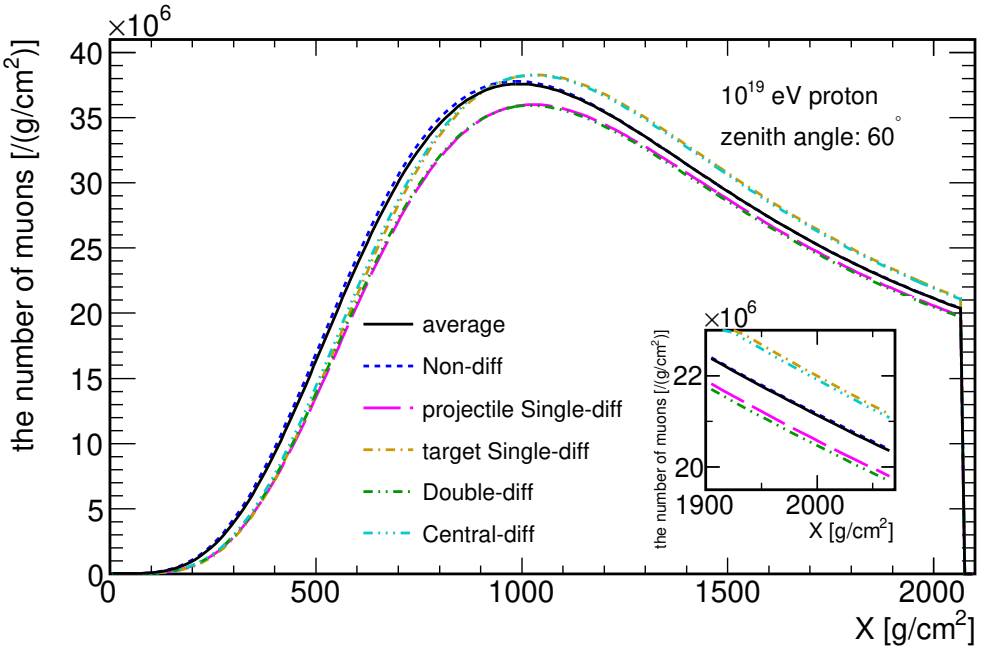

Fig. 4.12: Profiles of longitudinal developments of the number of muons with categorization using collision types at the first interaction. Profiles for ND, projectile SD, target SD, DD, and CD at the first interactions are illustrated by blue dotted, magenta dashed, yellow dash-dotted, green dash-two-dotted, and cyan dash-three-dotted lines, respectively. The profile of the average of all categories is illustrated by a black solid line. The figure is reproduced from Ref. [49].

	$\langle X_{\rm max}\rangle$ [g/cm^2]	Modified $\langle N_\mu^{\rm projectile\ SD}\rangle$ [$\times 10^7$] model for probability of diffractive-mass			the size of effects [%]
model	original	EPOS-LHC	QGSJET II-04	SIBYLL 2.3c	
EPOS-LHC	1.935± 0.002	1.935 ± 0.003	1.928 ± 0.003	1.944± 0.003	0.9± 0.2
QGSJET II-04	1.912 ± 0.002	1.905 ± 0.005	1.916 ± 0.002	1.902 ± 0.003	0.8 ± 0.2
SIBYLL 2.3c	2.078 ± 0.002	2.083 ±0.005	2.042 ± 0.004	2.076 ± 0.002	2.0 ± 0.3

Table 4.11: Modified $\langle N_\mu^{\rm projectile\ SD}\rangle$ with changing probability of diffractive mass for three probability by hadronic interaction models. Errors are statistical errors of estimations. Primary cosmic rays are protons with 10^{19} eV.

prediction in percent, ΔN_μ, is defined as,

$$\Delta N_\mu = \frac{\langle N_\mu^{\rm modified}\rangle - \langle N_\mu^{\rm original}\rangle}{\langle N_\mu^{\rm original}\rangle} \times 100, \tag{4.5}$$

where $\langle N_\mu^{\rm modified}\rangle$ and $\langle N_\mu^{\rm original}\rangle$ are a modified and a original prediction of mean of N_μ. From ΔN_μ illustrated in the bottom panel of Fig. 4.13 and the uncertainty region, we can calculate the size of effects, E_{N_μ}, defined as

$$E_{N_\mu} = \Delta N_\mu^{\rm Max.} - \Delta N_\mu^{\rm Min.}, \tag{4.6}$$

where $\Delta N_\mu^{\rm Max.}$ and $\Delta N_\mu^{\rm Min.}$ are the maximum and the minimum values of ΔN_μ in the uncertainty region for each case. The results of E_{N_μ} are 0.06-0.12 % for R_1, 0.03-0.09 % for R_2, and 0.07-0.10 % for 10^{19} eV primary. For 10^{17} eV primary, the size of effects are 0.00-0.12 % for R_1, 0.07-0.11 % for R_2, and 0.12-0.18 % for R_3. Statistical errors of this estimation are ± 0.1 % in ΔN_μ. Thus, effects of ratios on N_μ at the first interaction are less than 0.2 % and consistent to zero within statistical errors of estimations. These results show different features of N_μ comparing to $\langle X_{\rm max}\rangle$ and $\langle X_{\rm max}^\mu\rangle$; for $\langle X_{\rm max}\rangle$ and $\langle X_{\rm max}^\mu\rangle$, effects of R_1 are much larger than effects of the other ratios. By contrast, effects of R_1, R_2, and R_3 show similar values for N_μ.

Effects of diffractive mass are as large as effects of fractions of diffractive dissociation except for SIBYLL 2.3c cases. Original predictions of N_μ, modified N_μ with changing probability for diffractive mass, and the size of effects are presented in Tab. 4.11. The size of effects E_{N_μ} is calculated from Eqs. (4.6). The size of effects for projectile SD at the first interaction is 2.0% for SIBYLL 2.3c and less than 1.0% for EPOS-LHC and QGSJET II-04. Considering fractions of projectile SD and DD, the effects of the probability of diffractive mass at the first interaction are approximately 0.1 % for EPOS-LHC and QGSJET II-04 and 0.2 % for SIBYLL 2.3c at maximum. The size of effects is two times larger for SIBYLL 2.3c than the effects of fractions of diffractive dissociation. A dip structure at the low diffractive mass region in Fig. 4.11 may affect the result for SIBYLL 2.3c. This dip structure is only seen in SIBYLL 2.3c for both 10^{17} eV and 10^{19} eV proton primary and may be caused by modeling of particle productions in diffractive dissociation at low diffractive mass.

In an air shower, hadronic interactions occur repeatedly before muons are produced by the decay of charged pions, therefore effects on N_μ are piled up by the number of interactions before muons are produced. From Ref. [70], the number of interactions before producing muons for 10^{15} eV primary cosmic-rays are 4-7. Thus, for 10^{19} eV primary, the number of

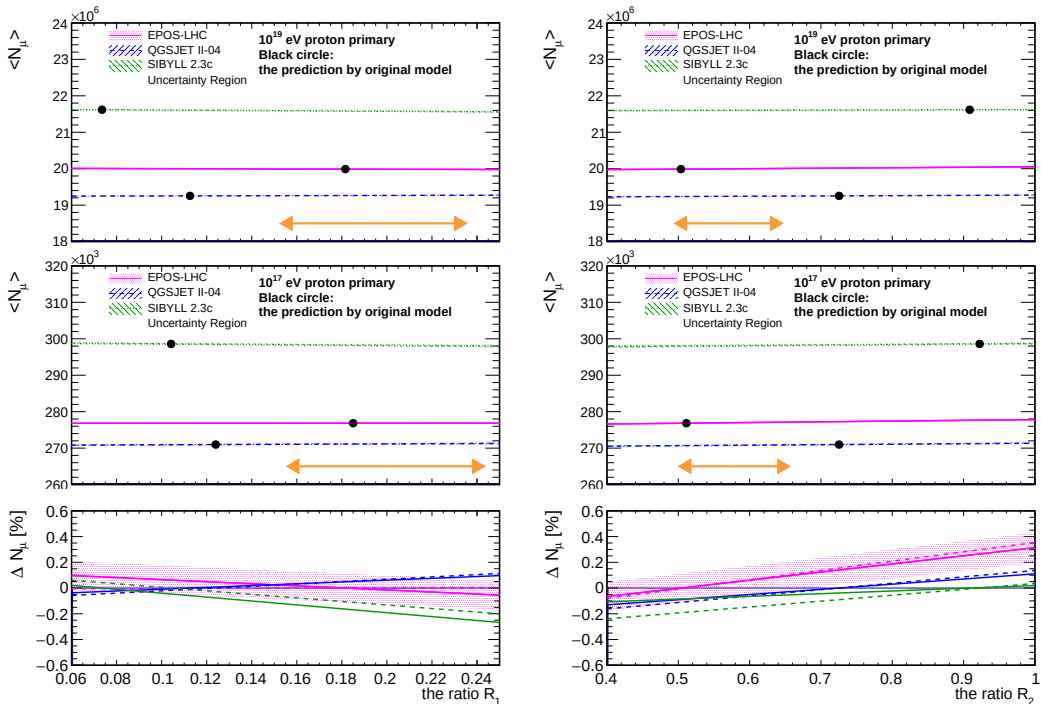

(a) R_1 dependence of $\langle N_\mu^{\mathrm{modified}} \rangle$ (b) R_2 dependence of $\langle N_\mu^{\mathrm{modified}} \rangle$

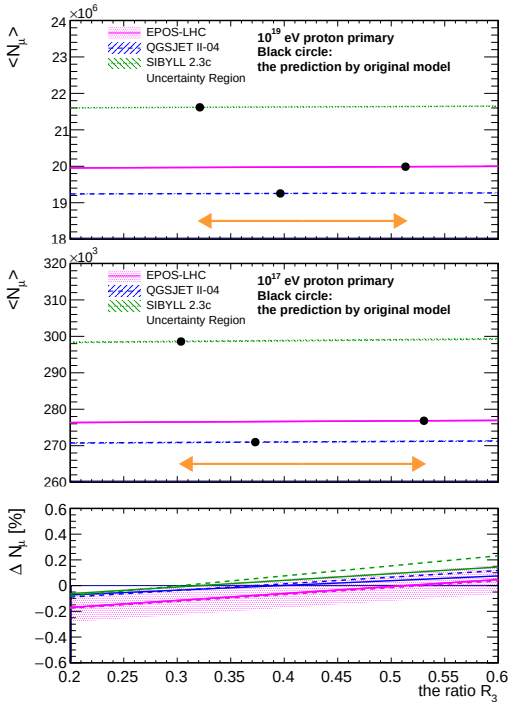

(c) R_3 dependence of $\langle N_\mu^{\mathrm{modified}} \rangle$

Fig. 4.13: Fraction dependencies of $\langle N_\mu \rangle$ for (a) R_1, (b) R_2, and (c) R_3. Top and middle panel for each figure show the results for 10^{19} eV and 10^{17} eV proton primary, respectively. Bottom panel of each figure shows difference $\Delta\langle N_\mu \rangle$ for 10^{19} eV (solid lines) and 10^{17} eV (dashed lines) primary. Orange arrays represent the uncertainty region estimated in Sec. 4.3. These figures are reproduced with modifications from Ref. [49].

interactions is expected to be 10 or more. The effects at the first interaction are 0.20% at maximum. If 0.20% is piled-up for 15 times, the size of effects is a few %. The sizes of these effects are much smaller than the muon deficit problem.

4.8 Summary of effects on $X_{\rm max}$ and N_μ

From discussions in this chapter, fractions of diffractive dissociation in inelastic collisions show large effects on $\langle X_{\rm max}\rangle$ and $\langle X^\mu_{\rm max}\rangle$, whereas other characteristics show minor effects on $X_{\rm max}$ or N_μ. Effects of uncertainty in R_1 are 6.7-9.1 $\mathrm{g/cm^2}$ at maximum for $\langle X_{\rm max}\rangle$ and 7.3-10.4 $\mathrm{g/cm^2}$ at maximum for $\langle X^\mu_{\rm max}\rangle$. Effects of uncertainty in R_2, R_3, and diffractive mass are less than 1.5 $\mathrm{g/cm^2}$ and less than 2.0 $\mathrm{g/cm^2}$ for $\langle X_{\rm max}\rangle$ and $\langle X^\mu_{\rm max}\rangle$, respectively. Differences of predictions among hadronic interaction models are 27.4 $\mathrm{g/cm^2}$ and 38.0 $\mathrm{g/cm^2}$ for $\langle X_{\rm max}\rangle$ and $\langle X^\mu_{\rm max}\rangle$, respectively. Thus, effects of R_1 are approximately one-third of the differences. Effects of other characteristics are less than one-tenth of the differences and negligible.

Effects of diffractive dissociation on $\langle X_{\rm max}\rangle$ and $\langle X^\mu_{\rm max}\rangle$ are found to be similar. Therefore, diffractive dissociation cannot solve the inconsistent interpretations of mass composition from $X_{\rm max}$ and $X^\mu_{\rm max}$ reported by PAO [65]. Effects of diffractive dissociation on N_μ and $\sigma(X_{\rm max})$ are a few % and less than 2 $\mathrm{g/cm^2}$, respectively. These effects are negligible comparing with muon deficit problem and differences between proton-induced and helium-induced showers for N_μ and $\sigma(X_{\rm max})$, respectively.

Chapter 5

Uncertainty of $\langle X_{\rm max} \rangle$ due to experimental uncertainties on diffractive dissociation

5.1 Experimental uncertainty in results from the LHC and its effects on $\langle X_{\rm max} \rangle$

Effects of diffractive dissociation were discussed in Chap. 4 with model-based definitions. As discussed in the previous chapter, the fraction of diffractive dissociation in inelastic collisions shows a substantially large effect, whereas other characteristics of diffractive dissociation show much smaller effects. Discussions with model-based definitions are useful to understand the effect of each characteristic. The following points are, however, not considered in the previous chapter: contamination of ND in experiments and differences in definitions between experiments and models.

We convert uncertainties in experimental results at the LHC to the uncertainty of $\langle X_{\rm max} \rangle$ with considering these points in this chapter. The primary particle of simulated air showers is a 10^{17} eV proton. Measurements considered in this chapter are measured for proton-proton collisions with $\sqrt{s} = 7$ TeV at LHC. These measurements correspond to 2.6×10^{16} eV in the laboratory frame. However, we perform the estimation with assuming negligible energy dependence in ratios of experimental results to predictions by each hadronic interaction model.

The procedure to estimate the uncertainty of $\langle X_{\rm max} \rangle$ from experimental uncertainty was as follows;

(i) The categorization with definitions in experiments was applied for the first interaction of simulated air shower events. For each category, $\langle X_{\rm max} \rangle$ was calculated. Tables 5.1 and 5.2 present the number of events and $\langle X_{\rm max} \rangle$ with experiment-based categorization. The fraction and $\langle X_{\rm max} \rangle$ for outside of definitions were calculated from Tabs. 5.1 and 5.2, Fig. 4.5(a), and Fig. 4.3 using Eq. (4.1).

(ii) The ratio of experimental results to model predictions in proton-proton collisions with $\sqrt{s} = 7$ TeV and its uncertainty were applied for the fraction of categorized events. The calculated ratios and their uncertainties are summarized in Tab. 5.3. Modified fractions were calculated by scaling the fraction of each category by the ratio in Tab. 5.3.

interaction model	collision type	the number of events			$\langle X_{\mathrm{max}} \rangle$ [g/cm^2]	
		total	pass	reject	pass	reject
EPOS-LHC	projectile SD	1000	630	370	731.40 ± 0.11	720.14 ± 0.18
	target SD	1000	745	255	732.40 ± 0.10	721.79 ± 0.27
	DD	1000	435	565	735.52 ± 0.16	716.03 ± 0.11
SIBYLL 2.3c	projectile SD	1000	955	45	729.90 ± 0.07	721.83 ± 1.26
	target SD	1000	967	33	753.18 ± 0.09	760.86 ± 2.94
	DD	1000	441	559	724.47 ± 0.16	724.87 ± 0.12

Table 5.1: The number of events and $\langle X_{\mathrm{max}} \rangle$ categorized by CMS definitions for each collision type at the first interaction. The primary particle is the 10^{17} eV proton. In CMS definitions, non-diffractive and central-diffractive collisions are excluded in measured regions.

Uncertainties of modified fractions were calculated from the uncertainty in the ratio. The experimental results considered in this chapter were results in Ref. [29, 30].

One should note that the energy dependence of r and its uncertainty was ignored in this estimation. Moreover, r measured for proton-proton collisions were applied for fractions of proton-air nucleus collisions. Major parts of diffractive dissociation in proton-air nucleus collisions were diffractive dissociation with one interacting nucleon in the nucleus. The collision was not diffractive dissociation if one or more interacting nucleons make ND collisions. Thus, cases with two or more interacting nucleons in diffractive dissociation were suppressed by a factor of the fraction of diffractive dissociation. Therefore, the assumption that r can be applied for proton-air nucleus collisions was not far from the theoretical descriptions in hadronic interaction models.

(iii) Using the modified fractions and their uncertainty, the effect of the fraction of diffractive dissociation at the first interaction was calculated using method A in Sec. 4.2.2 with experiment-based definitions for collision types. In this calculation, $\langle X_{\mathrm{max}} \rangle$ for each category predicted by EPOS-LHC were adopted.

(iv) The size of effects was multiplied by a factor of 2.4 to consider the maximum size of effects including collisions of secondary particles. This factor was coming from the analysis in Sec. 4.4.

(v) To consider nuclear effects, the procedure in step (i)-(iv) was repeated for predictions of fractions by EPOS-LHC and SIBYLL 2.3c for categorized events in step (ii). EPOS-LHC and SIBYLL 2.3c were utilized to consider uncertainty for predictions of proton-air collisions. For example, the enhancement of projectile SD in proton-air collisions was considered in SIBYLL 2.3c, but not considered in EPOS-LHC.

(vi) The procedure in step (i)-(v) was repeated for results by the CMS and the ALICE experiments [29, 30].

interaction model	collision type	the number of events			$\langle X_{\mathrm{max}} \rangle$ [g/cm^2]	
		total	pass	reject	pass	reject
EPOS-LHC	projectile SD	1000	502	498	732.33 ± 0.14	722.10 ± 0.13
	target SD	1000	609	391	735.51 ± 0.12	720.59 ± 0.18
	DD	1000	647	353	731.56 ± 0.10	711.56 ± 0.17
	ND	10000	973	9027	714.91 ± 0.07	684.12 ± 0.01
SIBYLL 2.3c	projectile SD	1000	643	357	729.30 ± 0.11	729.94 ± 0.20
	target SD	1000	638	362	755.72 ± 0.13	749.42 ± 0.23
	DD	1000	746	254	725.38 ± 0.09	722.68 ± 0.25
	ND	10000	2557	7443	723.41 ± 0.03	693.50 ± 0.01

Table 5.2: The number of events and $\langle X_{\mathrm{max}} \rangle$ categorized by ALICE definitions for each collision type at the first interaction. The primary particle is the 10^{17} eV proton. Pass in ND row corresponds to contamination of ND collisions to DD.

interaction model	experiment	$r + \delta r - \delta r$	
		Single-diff.	Double-diff.
EPOS-LHC	CMS	$1.04 + 0.22 - 0.17$	$0.85 + 0.28 - 0.13$
	ALICE	$1.95 + 0.45 - 0.78$	$0.54 + 0.16 - 0.16$
SIBYLL 2.3c	CMS	$0.78 + 0.17 - 0.13$	$6.19 + 2.05 - 0.92$
	ALICE	$1.85 + 0.43 - 0.73$	$0.38 + 0.11 - 0.11$

Table 5.3: Ratios of experimental results to predictions by hadronic interaction models for results by the CMS and the ALICE experiments in proton-proton collisions with $\sqrt{s} = 7$ TeV [29, 30].

5.2 Estimation of uncertainty of $\langle X_{\mathrm{max}} \rangle$

5.2.1 Estimation from the results by the CMS experiment

First, we estimate uncertainty of $\langle X_{\mathrm{max}} \rangle$ from results by the CMS experiment at $\sqrt{s} = 7$ TeV [29]. In the experiment, SD with $\xi < 0.05$ and DD with $\Delta\eta > 3$ were measured. To consider the definitions of measurements, these criteria were additionally applied for the categorization of simulated events. Fractions and $\langle X_{\mathrm{max}} \rangle$ with definitions of the CMS experiment, calculated in step (i), are presented in Tab. 5.4. The fractions rescaled by the ratio r and its uncertainty, calculated in step (ii), are presented in Tab. 5.5.

The effects of experimental uncertainty on $\langle X_{\mathrm{max}} \rangle$, calculated in step (iii) and (iv), are presented in Tab. 5.6. The uncertainty in measurements of SD corresponds to $^{+0.5}_{-0.4}$ g/cm^2 and $^{+0.6}_{-0.5}$ g/cm^2 using EPOS-LHC and SIBYLL 2.3c for fractions in step (i)-(iv), respectively. Differences between EPOS-LHC and SIBYLL 2.3c for fractions were 0.2 g/cm^2 and caused by different treatments in proton-nuleus collisions (nuclear effects). The uncertainty in measurements of DD corresponds to $^{+0.4}_{-0.2}$ g/cm^2 and $^{+0.3}_{-0.2}$ g/cm^2 on $\langle X_{\mathrm{max}} \rangle$ using EPOS-LHC and SIBYLL 2.3c, respectively. Using propagations of errors, the uncertainty propagated from measurements on $\langle X_{\mathrm{max}} \rangle$ was $^{+0.7}_{-0.5}$ g/cm^2 and $^{+0.7}_{-0.5}$ g/cm^2 using EPOS-LHC and SIBYLL 2.3c, respectively. According to Sec. 4.4, due to the effects of collisions of secondary particles, effects for the whole air showers were expected to be 2.4 times larger than those at the first interaction at maximum. Therefore, effects of uncertainty for the whole air shower were expected to be $^{+1.7}_{-1.1}$ g/cm^2 and $^{+1.7}_{-1.2}$ g/cm^2 at maximum using EPOS-LHC and SIBYLL 2.3c, respectively. With combining two uncertainties estimated using EPOS-LHC

		Fractions			
		projectile SD	target SD	DD	others
EPOS-LHC	Fraction [%]	2.5	3.3	3.5	90.7
	$\langle X_{\mathrm{max}} \rangle$ [g/cm^2]	731.4	734.4	735.5	690.6
SIBYLL 2.3c	Fraction [%]	6.4	2.8	0.36	93.1
	$\langle X_{\mathrm{max}} \rangle$ [g/cm^2]	729.9	753.2	724.5	704.8

Table 5.4: Fractions and $\langle X_{\mathrm{max}} \rangle$ for projectile SD, target SD, and DD with CMS definitions and those for the other events.

		Fractions		
		projectile SD	target SD	DD
EPOS-LHC	rescaled by r [%]	2.6	3.4	3.0
	rescaled by $r - \delta r$ [%]	2.2	2.9	2.5
	rescaled by $r + \delta r$ [%]	3.1	4.2	4.0
SIBYLL 2.3c	rescaled by r [%]	5.0	2.2	2.2
	rescaled by $r - \delta r$ [%]	4.2	1.8	1.9
	rescaled by $r + \delta r$ [%]	6.0	2.7	2.9

Table 5.5: Fractions rescaled by r and its uncertainty for CMS definition. r and its uncertainty shown in Tab. 5.3 are applied for fractions with CMS definition shown in Tab. 5.4.

and SIBYLL 2.3c for the whole air shower, $\langle X_{\mathrm{max}} \rangle$ and its uncertainty was $694.5^{+1.7}_{-1.2}$ g/cm^2.

5.2.2 Estimation from results by the ALICE experiment

Second, we estimate uncertainty from results by the ALICE experiment at $\sqrt{s} = 7$ TeV [30]. In the experiment, SD with $M_{\mathrm{X}} < 200$ GeV and DD with $\Delta\eta^{\mathrm{gap}} > 3$ were measured. Fractions and $\langle X_{\mathrm{max}} \rangle$ calculated in step (i) and fractions rescaled by ratio r calculated in step (ii) are presented in Tab. 5.7 and 5.8, respectively. The results of estimations of $\langle X_{\mathrm{max}} \rangle$ and its uncertainty in step (iii) and (iv) are presented in Tab. 5.9. Experimental uncertainties in measurements of SD and DD by the ALICE experiments correspond to $^{+1.0}_{-1.7}$ g/cm^2

	model for fractions before rescaling	considered uncertainty	$\langle X_{\mathrm{max}} \rangle$ [g/cm^2]	uncertainty
At first int.	EPOS-LHC	SD only	694.4	-0.4 $+0.5$
		DD only		-0.2 $+0.4$
		SD + DD		-0.5 $+0.7$
	SIBYLL 2.3c	SD only	694.6	-0.5 $+0.6$
		DD only		-0.2 $+0.3$
		SD + DD		-0.5 $+0.7$
	Differences in $\langle X_{\mathrm{max}} \rangle$		0.1	
Whole air shower (Uncertainty only)	EPOS-LHC	SD + DD		-1.1 $+1.7$
	SIBYLL 2.3c	SD + DD		-1.2 $+1.7$
	Nuclear effects			± 0.1

Table 5.6: $\langle X_{\mathrm{max}} \rangle$ with fractions rescaled by ratio r and uncertainty propagated from experimental uncertainty for the CMS case.

		Fractions			
		projectile SD	target SD	DD	others
EPOS-LHC	Fraction [%]	2.0	2.7	13.1	82.2
	$\langle X_{\mathrm{max}} \rangle$ [g/cm^2]	732.3	735.5	721.5	688.0
SIBYLL 2.3c	Fraction [%]	4.3	1.9	23.5	70.3
	$\langle X_{\mathrm{max}} \rangle$ [g/cm^2]	729.3	755.7	723.5	695.7

Table 5.7: Fractions and $\langle X_{\mathrm{max}} \rangle$ for projectile SD, target SD, and DD with ALICE definitions and those for the other events.

		Fractions		
		projectile SD	target SD	DD
EPOS-LHC	rescaled by r [%]	3.9	5.3	7.1
	rescaled by $r - \delta r$ [%]	2.3	3.2	5.0
	rescaled by $r + \delta r$ [%]	4.8	6.5	9.2
SIBYLL 2.3c	rescaled by r [%]	8.0	3.4	8.9
	rescaled by $r - \delta r$ [%]	4.8	2.1	6.3
	rescaled by $r + \delta r$ [%]	9.8	4.2	11.5

Table 5.8: Fractions rescaled by r and its uncertainty for ALICE definition. r and its uncertainty shown in Tab. 5.3 are applied for fractions with ALICE definition shown in Tab. 5.7.

and $^{+0.7}_{-0.7}$ g/cm^2, respectively, by using EPOS-LHC for estimations. Combining these two uncertainties, uncertainty came from both SD and DD measurements was $^{+1.2}_{-1.8}$ g/cm^2, if we consider effects at the first interaction only. If fractions predicted by SIBYLL 2.3c were adopted for fractions, the uncertainty came from both SD and DD measurements corresponds to $^{+1.5}_{-2.2}$ g/cm^2. Moreover, $\langle X_{\mathrm{max}} \rangle$ after rescaling of fractions vary 1.6 g/cm^2 between EPOS-LHC and SIBYLL 2.3c. This difference between the two models corresponds to differences caused by nuclear effects. Because projectile SD was enhanced compared to other collision types in SIBYLL 2.3c, the effects of the large ratio r from the ALICE experiment were enhanced by the fraction of projectile SD in SIBYLL 2.3c. Therefore, this effect showed a much larger size of effects than the CMS case.

Considering the effects of collisions of secondary particles, the size of uncertainty from measurements was expected to be 2.4 times larger. The results after multiplying by a factor of 2.4 were $^{+2.9}_{-4.3}$ g/cm^2 and $^{+3.6}_{-5.5}$ g/cm^2. The uncertainty from nuclear effects was ± 1.9 g/cm^2. This uncertainty from nuclear effects was calculated from 1.6 g/cm^2 differences at the first interaction and scaled by a factor of 2.4. The size of the uncertainty was larger than the CMS case because of the large uncertainty of diffractive dissociation in the measurement. For the result of the ALICE experiment, experimental uncertainty in measurements of SD was more important than that in measurements of DD. With combining two uncertainties estimated using EPOS-LHC and SIBYLL 2.3c for whole air shower, $\langle X_{\mathrm{max}} \rangle$ and its uncertainty were $695.4^{+4.0}_{-5.6}$ g/cm^2.

5.2.3 Estimated uncertainty of $\langle X_{\mathrm{max}} \rangle$ and discussions

Finally, uncertainty of $\langle X_{\mathrm{max}} \rangle$ from diffractive dissociation are discussed. Figure 5.1 illustrates the uncertainty. Black filled circle and its error bars are modified $\langle X_{\mathrm{max}} \rangle$ and uncer-

	model for fractions before rescaling	considered uncertainty	$\langle X_{\mathrm{max}} \rangle$ [g/cm^2]	uncertainty
At first int.	EPOS-LHC	SD only	694.6	-1.7 $+1.0$
		DD only		-0.7 $+0.7$
		SD + DD		-1.8 $+1.2$
	SIBYLL 2.3c	SD only	696.2	-2.1 $+1.2$
		DD only		-0.9 $+0.9$
		SD + DD		-2.2 $+1.5$
	Differences in $\langle X_{\mathrm{max}} \rangle$		1.6	
Whole air shower (Uncertainty only)	EPOS-LHC	SD + DD		-4.3 $+2.9$
	SIBYLL 2.3c	SD + DD		-5.5 $+3.6$
	Nuclear effects			± 1.9

Table 5.9: $\langle X_{\mathrm{max}} \rangle$ with fractions rescaled by ratio r and uncertainty propagated from experimental uncertainty for the ALICE case.

tainty by considering cross-section measurements of diffractive dissociation by the CMS experiment as discussed in Sec. 5.2.1. Black open circle and its error bars are modified $\langle X_{\mathrm{max}} \rangle$ and uncertainty estimated in Sec. 5.2.2. These uncertainties correspond to the uncertainty of the EPOS-LHC prediction from diffractive dissociation, since $\langle X_{\mathrm{max}} \rangle$ predicted by EPOS-LHC were adopted in estimations. Uncertainty from diffractive dissociation in EPOS-LHC is shown as the hatched region in Fig. 5.1. The maximum and the minimum value in error bars are considered as the maximum and the minimum value of uncertainty in EPOS-LHC.

The uncertainty from diffractive dissociation is substantially large; the size of uncertainty from results by the ALICE experiment is comparable with the difference between predictions by EPOS-LHC and QGSJET II-04, even though the difference between the two models is made from the pile-up of many reasons [71]. The size of uncertainty from results by the CMS experiment is small. However, results by the CMS experiment are valid only if predictions by PYTHIA8 MBR reproduce cross-sections of diffractive dissociation including very low diffractive mass cases.

The size of uncertainty from diffractive dissociation is comparable with one of the dominant sources of systematic uncertainty in measurements by PAO, *i.e.* reconstruction uncertainty and uncertainty of propagations of fluorescence lights in atmosphere [20]. Therefore, the uncertainty caused by measurements of diffractive dissociation is one of the dominant sources of uncertainty in interpretations of the mass composition. The uncertainty caused by these cross-section measurements should be reduced to less than ± 3.0 g/cm^2 to avoid effects on interpretations of mass composition.

Large uncertainty from diffractive dissociation is owing to low diffractive-mass cases and nuclear effects. Because of no direct measurements of diffractive dissociation for low diffractive-mass cases, systematic uncertainty of cross-section measurements of diffractive dissociation by the ALICE experiment [30] is very large. SD and DD cross-sections measured by the CMS experiment [29] depend on a hadronic interaction model. Limited data for proton-ion collisions also affect the uncertainty. From estimations in previous sections, nuclear effects are expected to be ± 1.9 g/cm^2 including effects in interactions between secondary particles and air nuclei. In the next chapters, we measure the low diffractive-mass cases directly using ATLAS and LHCf detectors and validate hadronic interaction models for these low diffractive-mass cases.

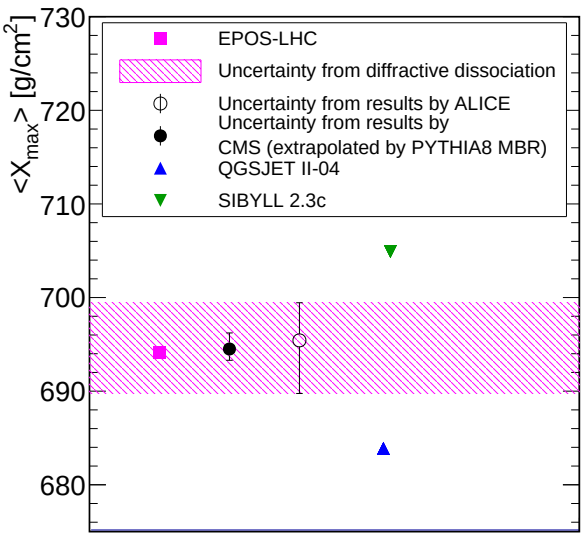

Fig. 5.1: Uncertainty of $\langle X_{\mathrm{max}} \rangle$ from diffractive dissociation. Uncertainty for the EPOS-LHC prediction is shown in the Magenta hatched region. Uncertainty in cross-section measurements of diffractive dissociation by the CMS and the ALICE experiments [29, 30] are considered. Black open and filled circles are estimated uncertainty considering measurements by the ALICE and the CMS experiment, respectively. Predictions of hadronic interaction models are also presented in a magenta square (EPOS-LHC), blue upward triangle (QGSJET II-04), and green downward triangle (SIBYLL 2.3c).

Chapter 6

ATLAS-LHCf joint analysis for direct measurements of photons from low diffractive mass events

6.1 Motivation and strategy of measurements

6.1.1 Motivation

As discussed in the previous chapter, the measurements of low diffractive-mass cases are important to reduce large experimental uncertainty in cross-section measurements of diffractive dissociation. Since a very large rapidity gap is expected for low diffractive-mass events, these events were not measured by the ALICE and the CMS experiment discussed in the previous chapter. Instead, these events were estimated by models. Results are valid only if the models used in the estimation correctly predict these events.

Very forward detectors which cover $|\eta| > 6.5$ are needed to measure low diffractive-mass events. The LHC forward (LHCf) experiment is one of the experiments at CERN LHC measuring very forward neutral particles in $|\eta| > 8.4$ using zero degree calorimeters. The LHCf experiment shares the interaction point with the ATLAS experiment. With combining detectors of the ATLAS and LHCf experiments, a direct measurement of photons produced in very low diffractive mass events becomes available. Only forward neutral particles are detected by the LHCf experiments since the detector was placed after the magnets to bend the beam particles. Detectors do not cover $5.0 < |\eta| < 8.0$. Thus, the measurements of $d\sigma^{\mathrm{SD}}/d\log_{10}\xi$ and $d\sigma^{\mathrm{DD}}/d\log_{10}\xi$ by detecting the rapidity gap are very hard. Meanwhile, particle productions in diffractive dissociation depend on the diffractive mass. If an energy spectrum of very forward photons is measured for specific diffractive-mass regions of SD, only $d\sigma^{\mathrm{SD}}/d\log_{10}\xi$ and particle productions affects the spectrum. In this chapter, we focus on the direct measurements of photons produced in low diffractive mass events of SD using ATLAS and LHCf detectors. In the next chapter, we discuss the interpretations of $d\sigma^{\mathrm{SD}}/d\log_{10}\xi$ from the spectrum. The validity of PYTHIA8 MBR is also discussed in the next chapter.

6.1.2 Strategy

A previous study presented the results of very forward photons from diffractive dissociation using ATLAS and LHCf detectors [72]. In the study, diffractive dissociation was selected by requiring $N_{\mathrm{ch}} = 0$, where N_{ch} is the number of charged particles in the pseudo-rapidity region covered by the inner detector of the ATLAS experiment. Very forward photons for the selected sample were measured by the LHCf detector. The result is illustrated in Fig. 6.1. The inclusive photon spectrum, very forward photons without any event selections measured by the LHCf experiment [73], is also illustrated by black circles in Fig. 6.1. The ratio of energy spectrum of very forward photons with $N_{\mathrm{ch}} = 0$ to inclusive energy spectrum is illustrated in Fig. 6.2. EPOS-LHC shows good agreements for the photon spectrum in $\eta > 10.94$ with $N_{\mathrm{ch}} = 0$ selections. PYTHIA8 DL shows good agreements for the photon spectrum in $8.81 < \eta < 8.99$ with $N_{\mathrm{ch}} = 0$ selections. A kink of the ratio was observed around 3 TeV for $\eta > 10.94$. The similar kink was predicted by EPOS-LHC. With $N_{\mathrm{ch}} = 0$ selections, events with large rapidity gap were selected since $|\eta| < 2.5$ are covered by the inner detector. Thus, we can select photons produced by diffractive dissociation with approximately $\log_{10}\xi < -5.0$. However, SD and DD were mixed in the measured samples. We cannot compare the results with predictions of SD directly, which is required to discuss effects of photon productions and $d\sigma^{\mathrm{SD}}/d\log_{10}\xi$.

Predictions of the SD fraction of the photon spectrum with $N_{\mathrm{ch}} = 0$ depend on hadronic interaction models. Figure 6.3 illustrates predictions of the SD fraction. A measurement of the SD fraction is required. In this chapter, by using another detector of the ATLAS experiment, we measure the SD fraction and the very forward photon spectrum from $\log_{10}\xi < -5.0$ in SD.

6.2 ATLAS and LHCf detectors

In this study, we utilize the inner detector and the Minimum Bias Trigger Scintillator (MBTS) detector of the ATLAS experiment [74] and the LHCf-Arm1 detector [75]. These detectors were installed around IP1 of LHC. Thus, the same collisions were measured by these detectors. The inner detector consists of three sub-detectors: silicon pixel detectors, which are installed close to the beam pipe, silicon microstrip detectors, which are surrounding silicon pixel detectors, and transition radiation detectors, which are at the outside of silicon microstrip detectors. The inner detector covers $|\eta| < 2.5$ and measures charged particles produced in $|\eta| < 2.5$. The MBTS detector [76] consists of segmented plastic scintillator detectors. The inner ring of the MBTS detector consists of four segmented detectors with equal angle coverages for each segment, and measures particles in $2.76 < |\eta| < 3.86$. The outer ring of the MBTS detector consists of eight segmented detectors and covers $2.07 < |\eta| < 2.76$.

The LHCf-Arm1 and Arm2 detectors [75, 77] are zero degree calorimeters and were installed at 140 m away from IP1. Each detector covers each side of IP1. The LHCf-Arm1 detector consists of two sampling calorimeter towers. One tower covered 20×20 mm regions around the projected beam center, which corresponds to $\eta > 10$. The other tower covered 40×40 mm regions at off-axis, which corresponds to $8.5 < \eta < 9.5$. Each calorimeter tower consists of tungsten plates, GSO scintillator plates, and GSO bar hodoscopes for position-sensitive layers. The thickness of detectors corresponds to 44 radiation lengths and 1.4 interaction lengths. Energy and position resolutions for photons were $< 5\,\%$ and $< 200\,\mu$m,

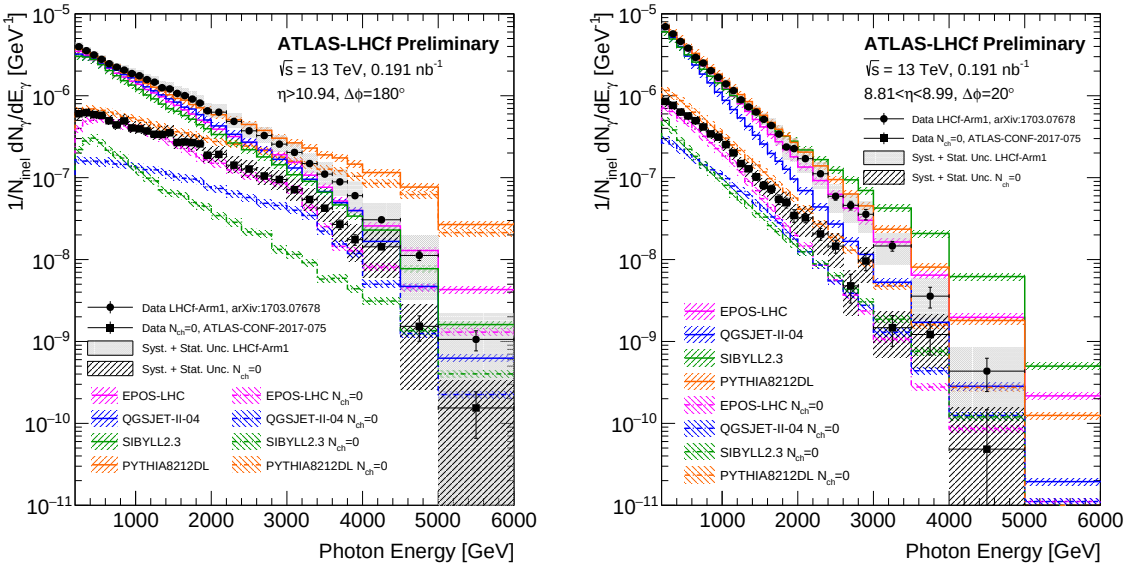

Fig. 6.1: Energy spectra of inclusive very forward photon and very forward photons with $N_{\rm ch} = 0$ selections. Very forward inclusive photon spectrum measured by the LHCf detector [73] is illustrated with black circle for $\eta > 10.94$ (left) and $8.81 < \eta < 8.99$ (right). Photons with $N_{\rm ch} = 0$ selections measured by ATLAS and LHCf detectors [72] is also illustrated with black square. Predictions by EPOS-LHC, QGSJET II-04, SIBYLL2.3, and PYTHIA8 DL are shown in magenta, blue, green, and orange lines, respectively. Solid and dot-dashed lines are predictions for inclusive and $N_{\rm ch} = 0$, respectively. These figures are taken from Ref. [72].

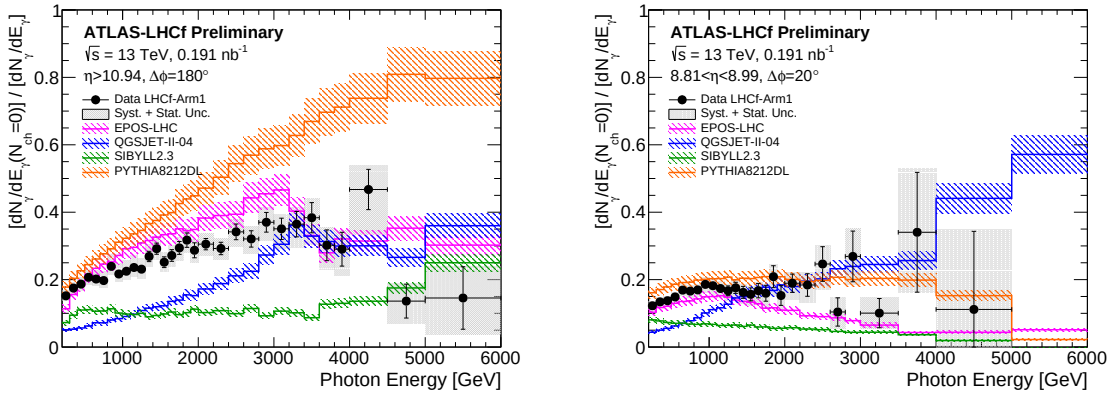

Fig. 6.2: Ratio of energy spectrum of very forward photons with $N_{\rm ch} = 0$ to inclusive energy spectrum of very forward photons for $\eta > 10.94$ (left) and $8.81 < \eta < 8.99$ (right) [72].

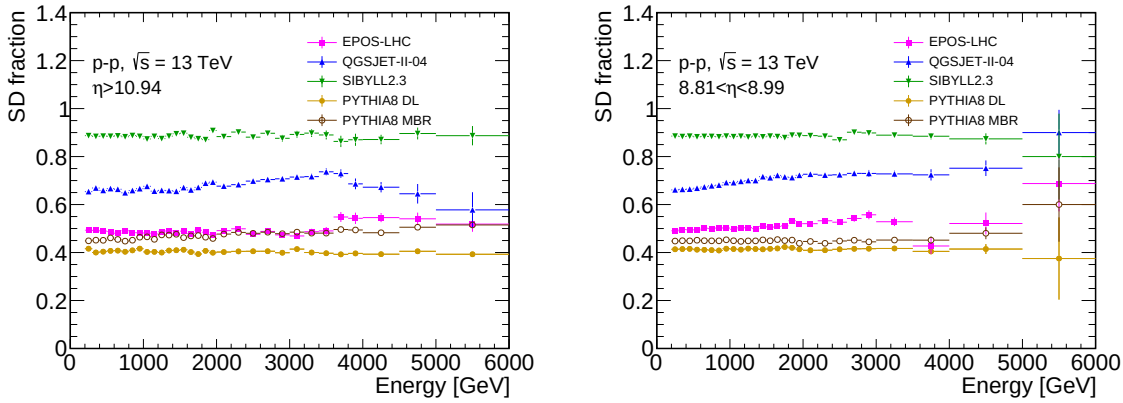

Fig. 6.3: Fractions of photons from SD in photons with $N_{\rm ch} = 0$ selections predicted by hadronic interaction models for Region A(left) and Region B(right).

respectively.

6.3 Data set

Data for the analysis in this chapter were taken in 2015 June 12-13, 22:32-1:30 (CEST), which corresponds to LHC Fill3855. It was a low luminosity run with $\beta^* = 19\,\mathrm{m}$ and with 145 μrad half crossing angles at IP1 in vertical down-going direction. The number of collisions per bunch crossing was 0.007 to 0.012. The integrated luminosity was 0.191 nb^{-1} for LHCf-Arm1. Trigger signals from the LHCf and the ATLAS were exchanged to record all events triggered by the LHCf detector. Delay of the LHCf trigger signals was measured and corrected in the commissioning phase using a very low luminosity beam. The trigger efficiency for photons above 200 GeV was 100%. Approximately 50% of the triggered events were recorded by the LHCf data acquisition system. Details were summarized in Ref. [72, 78]. This data set was identical to that analyzed in Ref. [73, 72].

6.4 MC simulations

Since there were no common simulations for ATLAS and LHCf detectors, we adopted simulations without detector simulations. The LHCf-Arm1 response function and response functions for ATLAS detectors were applied to emulate the detector responses. We prepared MC sample (a) and (b) as listed in Tab. 6.1. CRMC version 1.6 was adopted for event generations with EPOS-LHC, QGSJET II-04, and SIBYLL 2.3. PYTHIA8 version 8.212 was also adopted for event generations. DL and MBR tunes of PYTHIA8 [79, 50] discussed in Sec. 3.2 were adopted in this analysis. Hereafter, we call them PYTHIA8 DL and PYTHIA8 MBR, respectively. PYTHIA8 MBR was adopted only for comparison with data. Decay, effects of magnets, and transport in the beam pipe were simulated with Cosmos-Epics interface [80]. DPMJET III[81] was adopted for hadronic interaction in the Cosmos-Epics interface. In sample (c), for performance test of the LHCf-Arm1 response function, particle transport and detector response was simulated in Cosmos-Epics interface [80] with DPMJET III [81]. The size of sample (c) was 10^8 for QGSJET II-04 and 5×10^8 for EPOS-LHC

in the event generator. The beam test of the LHCf-Arm1 detector was performed using electron and muon beams at the Super Proton Synchrotron at CERN [77]. Using the electron and muon beams up to 250 GeV, it was confirmed that the simulation well reproduces the measured data.

The detector response of the LHCf-Arm1 detector was emulated by the response function. Since only the number of hits in the LHCf-Arm1 detector were considered in this analysis, the function only emulated hits in the detector. The function emulated photon-like hits based on the energy, position, particle type, and the number of hits in each calorimeter tower of the LHCf-Arm1 detector. For the case with one particle hit in the calorimeter tower (single-hit), the function considered trigger efficiency and particle identification. Since the thickness of the detector corresponds to 1.4 interaction lengths, particle showers induced by hadrons typically developed deeper parts of the detector, whereas particle showers induced by photons developed in early parts of the detector. Moreover, part of the hadrons did not make signals. Particle identification of the LHCf detectors was based on the longitudinal development of particle showers in the detector. In particle identification, 90% of photons passed these selections at high energy. Moreover, some contamination of hadrons hit in the detector was expected. These effects were considered by the empirical function in the response function. For the case with more than one particle hit in the calorimeter tower (multi-hit), most cases were rejected by the selection to reject these multi-hit events. However, if two particles hit close to each other or the energy of one particle was much larger than the other one, the event was mistakenly considered as a single-hit. Moreover, if a photon and a hadron hit in the detector and the hadron did not make signals in the detector, signals in the event were identical to the single-photon hit. These effects were emulated in the response function.

The response functions for ATLAS detectors were calculated using ATLAS full detector simulations based on GEANT4 [82, 83]. The response of the inner detector was emulated with detection efficiency. The detection efficiency was calculated for six particles, p, $\bar{p}$, K^+, K^-, π^+, π^-, as functions of p_{T}, where p_{T} was the transverse momentum of particles, and η of the incident particle. The similar parameterization was adopted in Ref. [84]. Figures 6.4 illustrate detection efficiencies. These efficiencies were applied for each particle hit in the inner detector. For the particles other than these six types, efficiency for the particle with the same charge and the closest mass was utilized.

Detection efficiency for the MBTS detector were calculated for ND and diffractive dissociation separately. For diffractive dissociation after $N_{\mathrm{ch}} = 0$ selections in the inner detector, detection efficiency was calculated as a function of $\log_{10}\xi$. Left and right plots of Fig. 6.5 illustrate detection efficiency for LHCf-Arm1-side and LHCf-Arm2-side MBTS detectors, respectively. Detection efficiency was 100% for $\log_{10}\xi > -5.5$ and decreased to 0 at $\log_{10}\xi \approx -7.0$. For ND events after $N_{\mathrm{ch}} = 0$ selections in the inner detector, detection efficiency was larger than 80% and mostly 100%. In the analysis, detection efficiency for ND events was assumed as 100%. Systematic uncertainty caused by this assumption was estimated by changing efficiency from 100% to 80%.

6.5 Event reconstruction and selections

In this analysis, event reconstruction and selections in the LHCf-Arm1 and the inner detector were identical to the analysis in Ref. [72]. Following event reconstructions and selections

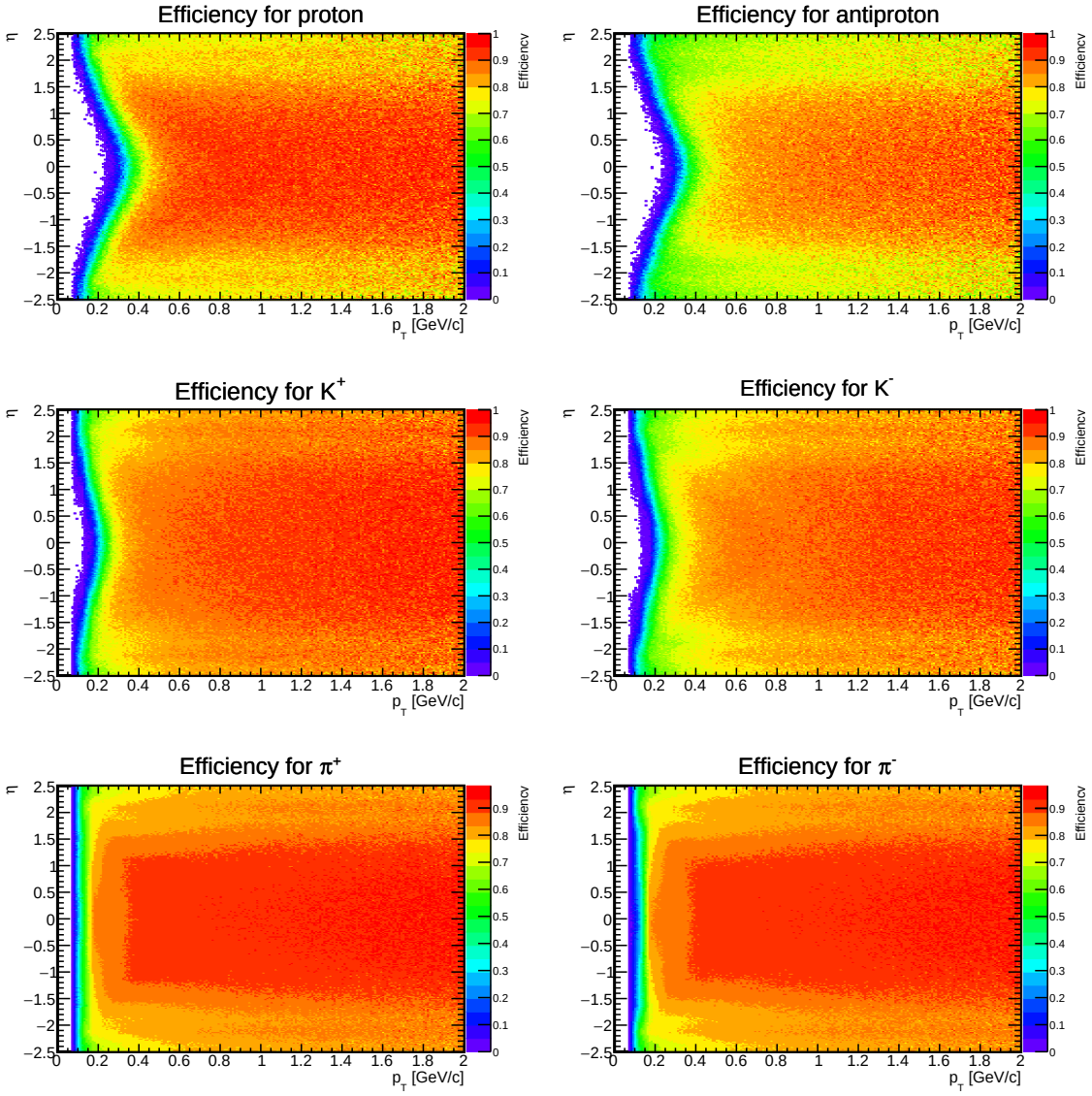

Fig. 6.4: Detection efficiency of the inner detector for p (upper left), $\bar{p}$ (upper right), K^+ (middle left), K^- (middle right), π^+ (bottom left), and π^- (bottom right) calculated by ATLAS full simulation.

Sample	Event Generator	Particle transport	detector	sample size
(a)	CRMC v1.6	Cosmos-Epics	response functions	10^8 collisions
PYTHIA8 in (a)	PYTHIA8 interface	Cosmos-Epics	response functions	10^8 collisions
(b)	CRMC v1.6	no	no	10^8 collisions
PYTHIA8 in (b)	PYTHIA8 interface	no	no	10^8 collisions
(c)	CRMC v1.6	Cosmos-Epics	Cosmos-Epics	10^8 or 5×10^8

Table 6.1: MC samples prepared for this study. For each sample, EPOS-LHC, QGSJET II-04, SIBYLL 2.3, and PYTHIA8 with DL tune (PYTHIA8 DL) are adopted. EPOS-LHC, QGSJET II-04, and SIBYLL 2.3 are produced with CRMC v1.6, whereas PYTHIA8 DL is produced with its own interface.

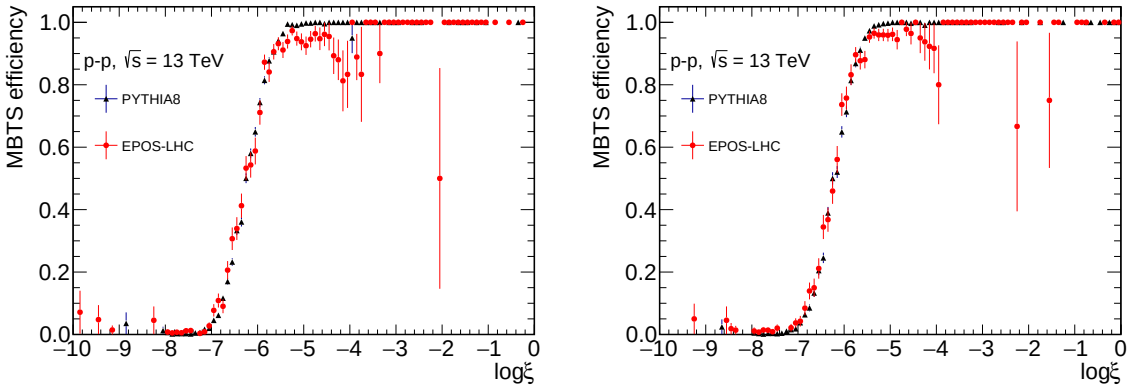

Fig. 6.5: Efficiency of the MBTS detector for Arm1 side (left) and Arm2 side (right) with inner detector veto and photon hits in the LHCf-Arm1 detector.

were applied; for the LHCf-Arm1 detector, energy was reconstructed from the sum of energy deposited in the 2nd to 13th scintillator layers and using the empirical function. Hit positions were reconstructed from lateral hit distributions in GSO bar hodoscopes. Hit position dependency and leakages of particles from a calorimeter were corrected in the energy reconstruction. Details were summarized in Ref. [77]. Photon-like events were selected by the $L_{90\%} < L_{thres}$, where $L_{90\%}$ was the depth that 90% of energy are deposited in the detector in units of the radiation length. Photons typically show smaller $L_{90\%}$ values than hadrons in the LHCf-Arm1 detector. Roughly 90% of all photons passed the criterion. Events that were reconstructed as multi-hit were rejected due to the poor performance of the energy reconstruction for multi-hit events [85]. The energy threshold was 200 GeV in reconstructed energy. Photons on the LHCf-Arm1 detector hit in fiducial regions were selected. The fiducial regions were $r < 5$ mm and $-135°$ to $45°$ in azimuth angle for Region A and $38 < r < 42$ mm and $80°$ to $100°$ in azimuth angle for Region B, where r was the distance from projected beam center on the detector. Region A and Region B correspond to $\eta > 10.94$ and $8.99 > \eta > 8.81$, respectively.

In the inner detector, charged particle tracks with at least one-pixel hit and $|d_0| < 1.5$ mm, where d_0 was the transverse impact parameter from the LHC beamline, were reconstructed using silicon pixel detectors and silicon microstrip detectors of the inner detector. The events that the number of charged-particle tracks was zero were selected. The threshold for the particles was set to $p_{\mathrm{T}} > 100\,\mathrm{MeV}$ in this analysis. For the MBTS detector, the threshold was set to $0.15\,\mathrm{pC}$. If one of the plastic scintillator segments detects a signal above the threshold, the MBTS detector on the side was considered with a hit. If a signal above $0.15\,\mathrm{pC}$ were detected, at least one particle was detected since the threshold was set to be well above the electrical noise [86].

Events selected by the LHCf-Arm1 and the inner detector were categorized into SD-rich, DD-rich, and the others by the hit information in the MBTS detector on both sides. Figure 6.6 (a) illustrates the schematic view of the detector coverage in pseudo-rapidity. Since events with a photon-like hit in the LHCf-Arm1 detector and no charged tracks in the inner detector were selected, events with the large rapidity gap were already selected. Events with MBTS hit on the LHCf-Arm1 side but without any signals in MBTS on the opposite side were categorized into the SD-rich sample. Events with MBTS hit on the opposite side were

categorized into the DD-rich sample. No selections using MBTS on the LHCf-Arm1 side were applied for the DD-rich sample. DD and ND were mainly included in the DD-rich sample. The other events were not used for the SD fraction measurements. Figures 6.6 (b)-(h) illustrate schematic views of categories using these detectors for each collision type. Figures 6.6 (b), (e), and (f) illustrate schematic view of events included in the DD-rich sample. As discussed in the previous section, most ND events make signals in MBTS. Figures 6.6 (c) and (g) illustrate schematic view of events included in the SD-rich sample. After these event selections, the number of events in SD-rich and DD-rich samples with photon-like hits in LHCf-Arm1 Region A was 1441 and 1325, respectively.

6.6 Analysis method

The fraction of SD for the very forward photon samples was measured from the number of events in SD-rich and DD-rich samples using an MC-driven response matrix. The analysis procedure was as follows. Hereafter, the subscript $N_{\rm track} = 0$ donates the number of events in MC samples (a) after applying the LHCf-Arm1 response function, the inner detector efficiency, and the MBTS efficiency. The subscript $N_{\rm ch} = 0$ donates the number of events in MC samples (b) with true photons above $200\ \mathrm{GeV}$ in the analysis region.

(i) Subtraction of ND contamination in SD-rich and DD-rich samples

Before the conversion using an MC-driven response matrix, we subtracted ND contamination for the simple and stable analysis. The efficiency of the MBTS detector for ND events was at least 80% and mostly 100% in the $N_{\rm track} = 0$ sample. Thus, we assumed efficiency as 100%. The systematic uncertainty was calculated by changing the efficiency from 100% to 80%. With 100% efficiency, all ND events were contaminated in the DD-rich sample. Therefore, the number of the DD-rich sample after subtraction, $N^{'}_{\rm DD-rich}$, was

$$N^{'}_{\rm DD-rich} = N_{\rm DD-rich} - N^{\rm data}_{N_{\rm track}=0} \times \frac{N^{\rm ND,MC}_{N_{\rm track}=0}}{N^{\rm SD,MC}_{N_{\rm track}=0} + N^{\rm DD,MC}_{N_{\rm track}=0} + N^{\rm ND,MC}_{N_{\rm track}=0}}, \tag{6.1}$$

where $N^{\rm data}_{N_{\rm track}=0}$ was the number of events of experimental data in the $N_{\rm track} = 0$ sample. $N^{i,\rm MC}_{N_{\rm track}=0}$ was the number of events predicted for collision type i by simulation in the $N_{\rm track} = 0$ sample. Collision type i can be SD, DD, or ND.

(ii) Unfolding using the MC-driven response matrix

For the number of events after subtraction of ND contamination, the number of SD-rich and DD-rich samples can be written as,

$$\begin{pmatrix} N_{\rm SD-rich} \\ N^{'}_{\rm DD-rich} \end{pmatrix} = R^{\rm MBTS} \begin{pmatrix} N^{\rm SD}_{N_{\rm ch}=0} \\ N^{\rm DD}_{N_{\rm ch}=0} \end{pmatrix}, \tag{6.2}$$

where $R^{\rm MBTS}$ was a 2×2 detector response matrix calculated from MC simulation. With an inverse matrix of $R^{\rm MBTS}$, we can calculate the number of SD and DD events in $N_{\rm ch} = 0$ samples,

$$\begin{pmatrix} N^{\rm SD,Data}_{N_{\rm ch}=0} \\ N^{\rm DD,Data}_{N_{\rm ch}=0} \end{pmatrix} = (R^{\rm MBTS})^{-1} \begin{pmatrix} N_{\rm SD-rich,Data} \\ N^{'}_{\rm DD-rich,Data} \end{pmatrix}, \tag{6.3}$$

where $N^{\mathrm{SD,Data}}_{N_{\mathrm{ch}}=0}$ and $N^{\mathrm{DD,Data}}_{N_{\mathrm{ch}}=0}$ were the number of SD and DD events in the $N_{\mathrm{ch}} = 0$ sample calculated from experimental data. The fraction of SD without ND contamination $C^{\mathrm{SD,Data}}_{\mathrm{step\,(ii)}}$ was calculated as $C^{\mathrm{SD,Data}}_{\mathrm{step\,(ii)}} = N^{\mathrm{SD,Data}}_{N_{\mathrm{ch}}=0}/(N^{\mathrm{SD,Data}}_{N_{\mathrm{ch}}=0} + N^{\mathrm{DD,Data}}_{N_{\mathrm{ch}}=0})$. We subtracted ND contamination in Step (i) to avoid the 3×3 response matrix with very small factors related to ND contamination.

(iii) ND contamination in the $N_{\mathrm{ch}} = 0$ sample

Contamination of ND was not considered in the fraction $C^{\mathrm{SD,Data}}_{\mathrm{step\,(ii)}}$. The ND contamination was corrected using MC predictions as,

$$C^{\mathrm{SD,Unfolded}} = C^{\mathrm{SD,Data}}_{\mathrm{step\,(ii)}} \times \frac{N^{\mathrm{SD,MC}}_{N_{\mathrm{ch}}=0} + N^{\mathrm{DD,MC}}_{N_{\mathrm{ch}}=0}}{N^{\mathrm{SD,MC}}_{N_{\mathrm{ch}}=0} + N^{\mathrm{DD,MC}}_{N_{\mathrm{ch}}=0} + N^{\mathrm{ND,MC}}_{N_{\mathrm{ch}}=0}}. \tag{6.4}$$

One should note that the calculation was performed for the sample with photon hits in Region A ($\eta > 10.94$) of LHCf-Arm1.

(iv) $C^{\mathrm{SD,Unfolded}}$ calculated in Step (iii) were equal to the fraction of SD in the sample with $N_{\mathrm{ch}} = 0$ and a photon hit in Region A. We introduced a parameter X defined as,

$$X = C^{\mathrm{SD,unfolded}} \times \frac{\int N^{all}_{N_{\mathrm{ch}}=0,\mathrm{RegionA}}}{\int N^{SD}_{N_{\mathrm{ch}}=0,\mathrm{RegionA}}}. \tag{6.5}$$

By applying the parameter X to predictions of the SD fraction, we can calculate the energy-dependent SD fraction,

$$C^{\mathrm{SD,Region\,A}}(E) = \frac{X N^{\mathrm{SD,Region\,A}}(E)}{N^{\mathrm{all,Region\,A}}(E)}. \tag{6.6}$$

The fractions for photon hits in LHCf Region B ($8.81 < \eta < 8.99$) can be calculated in the same way using the common X,

$$C^{\mathrm{SD,Region\,B}}(E) = \frac{X N^{\mathrm{SD,Region\,B}}(E)}{N^{\mathrm{all,Region\,B}}(E)}. \tag{6.7}$$

Hereafter, we call the mean value of the SD fraction for photon hits in Region A as $C^{\mathrm{SD,Region\,A}}$. $C^{\mathrm{SD,Region\,A}}$ was calculated as

$$C^{\mathrm{SD,Region\,A}} = \frac{X \int N^{\mathrm{SD,Region\,A}}(E)dE}{\int N^{\mathrm{all,Region\,A}}(E)dE}, \tag{6.8}$$

and

$$C^{\mathrm{SD,Region\,B}} = \frac{X \int N^{\mathrm{SD,Region\,B}}(E)dE}{\int N^{\mathrm{all,Region\,B}}(E)dE}. \tag{6.9}$$

The energy-dependent value of the SD fraction for photon hits in Region A was called $C^{\mathrm{SD,Region\,A}}(E)$.

Calculations in this method depend on MC simulations utilized in the calculation of R^{MBTS} and the number of MC events. Diffractive mass dependencies of cross-sections and photon productions in diffractive dissociation affected R^{MBTS}. Thus, the hadronic interaction model utilized in this calculation should reproduce experimental data. The validation of hadronic interaction models was performed in Sec. 6.7.2.

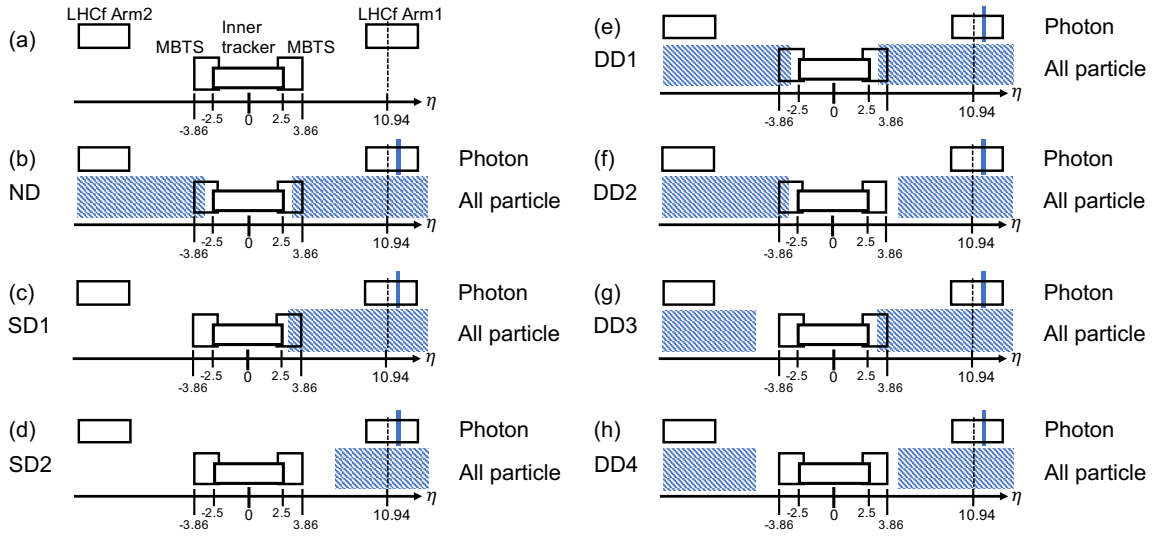

Fig. 6.6: (a) Schematic view of detector coverage of the inner detector, the MBTS detectors, and LHCf detectors. (b-h) Schematic views of particle distributions with inner detector veto. (b)-(d) illustrate particle distributions for SD. (e-h) illustrate particle distributions for DD. Hatched regions represent regions with particle productions in pseudo-rapidity. (b), (e), and (f) are included in the DD-rich sample, and (c) and (g) are included in the SD-rich sample.

6.7 Validation of method and simulations

6.7.1 Validation of method using simulations

Validation of the method described in Sec. 6.6 was performed with substituting simulations for experimental data. $N_{\mathrm{SD-rich}}$, $N_{\mathrm{DD-rich}}$, and $N^{\mathrm{data}}_{N_{\mathrm{track}}=0}$ in Step (i) were simulated using a hadronic interaction model instead of data. The SD fraction $C^{\mathrm{SD,Unfolded}}$ in Step (iii) was calculated using another hadronic interaction model for fraction calculations. This performance test was performed for four hadronic interaction models instead of experimental data (dummy data) and for four hadronic interaction models for fraction calculations.

The results are shown in Tab. 6.2. The original fraction for each hadronic interaction model is also shown in these tables. Calculated results depend on the hadronic interaction models adopted for fraction calculations, whereas differences between calculated results and the original fraction were less than 0.1 in $C^{\mathrm{SD,Unfolded}}$. For example, if PYTHIA8 DL is used for the dummy data as shown in the third row in Tab. 6.2, calculated results using four models show fractions from 0.404 to 0.487, whereas the true fraction for PYTHIA8 DL is 0.404. The difference between true and calculated fractions is 0.083 at maximum for PYTHIA8 DL. Hereafter, we refer to these differences between true and calculated fractions as "biases of the method". These biases are mainly caused by model dependencies in R^{MBTS} and ND subtractions.

$C^{\mathrm{SD,Region\,B}}$ is also calculated with substituting simulations for experimental data. Table 6.3 illustrates calculated results. Biases of the method are similar with $C^{\mathrm{SD,Unfolded}}$ even though the common X was calculated only from results for Region A and applied in calculations of $C^{\mathrm{SD,Region\,B}}$. For example, for PYTHIA8 DL for the dummy data, calculated $C^{\mathrm{SD,Region\,B}}$ are 0.413 to 0.491, whereas the true fraction for PYTHIA8 DL is 0.413. The bias of the method is 0.078. In consequence, this method works well with some systematic

	model for the calculation				the original
	PYTHIA8 DL	EPOS-LHC	QGSJET II-04	SIBYLL 2.3	SD fraction
model for dummy data					
PYTHIA8 DL	0.404	0.444	0.487	0.488	0.404
EPOS-LHC	0.436	0.484	0.530	0.517	0.484
QGSJET II-04	0.591	0.641	0.670	0.649	0.670
SIBYLL 2.3	0.862	0.891	0.906	0.883	0.883

Table 6.2: SD fractions $C^{\mathrm{SD,Unfolded}}$ estimated using predictions by hadronic interaction models instead of experimental data. Fractions are calculated for four hadronic interaction models for the calculation.

	model for the calculation				the original
	PYTHIA8 DL	EPOS-LHC	QGSJET II-04	SIBYLL 2.3	SD fraction
model for dummy data					
PYTHIA8 DL	0.413	0.452	0.491	0.487	0.413
EPOS-LHC	0.445	0.493	0.535	0.516	0.493
QGSJET II-04	0.604	0.653	0.676	0.648	0.676
SIBYLL 2.3	0.880	0.908	0.914	0.882	0.882

Table 6.3: SD fractions for Region B $C^{\mathrm{SD,Region\,B}}$ estimated using predictions by hadronic interaction models instead of experimental data. Fractions are calculated for four hadronic interaction models for the calculation.

uncertainty owing to the bias of the method.

6.7.2 Validation of detector simulations using experimental data

The result of the analysis depends on hadronic interaction models. There were not enough experimental data for $\log_{10}\xi < -5.0$ to tune hadronic interaction models. Therefore, it was important to validate hadronic interaction models in the region. In the analysis, events with no tracks in $|\eta| < 2.5$ of the inner detector, a photon-like hit above 200 GeV in Region A of the LHCf-Arm1 detector were selected. Hit information in the MBTS detector was used to select SD-rich and DD-rich samples. Using no tracks in $|\eta| < 2.0$ of the inner detector and counting tracks in $|\eta| > 2.0$, where the inner detector and the MBTS detector were overlapped, we can partially validate particle distributions in SD-rich and DD-rich samples.

Figures 6.7 and 6.8 illustrate particle distributions in the inner detector with a photon-like hit in Region A of the LHCf-Arm1 detector. Without selections using charged particles in the inner detector, where contributions of ND are dominant, QGSJET II-04 shows good agreements with data. By contrast, without any charged tracks in $|\eta| < 2.0$ of the inner detector, where contributions from diffractive dissociation are dominant, PYTHIA8 DL and EPOS-LHC show better agreements than QGSJET II-04 and SIBYLL 2.3.

Figures 6.9 illustrate the number of hits in $2.0 < \eta < 2.5$ (left) and $-2.5 < \eta < 2.5$ (right) without any charged tracks in $|\eta| < 2.0$ and a photon-like hit in Region A of the LHCf-Arm1 detector. The left plot corresponds to a mixture of SD-rich and DD-rich samples. The right plot corresponds to the DD-rich sample. EPOS-LHC shows good agreements for the number of hits less than 2. PYTHIA8 DL shows better agreements for the number of hits larger than 2. From these plots, QGSJET II-04 and SIBYLL 2.3 show worse performance for SD-rich and DD-rich samples.

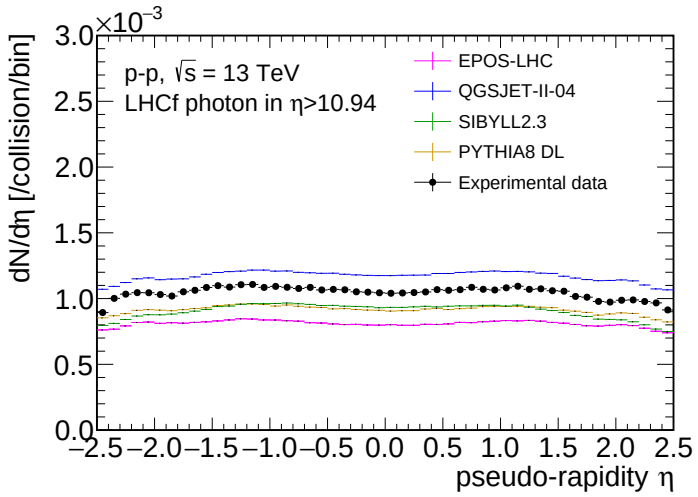

Fig. 6.7: $dN/d\eta$ in the inner detector with photons above $E_\gamma > 200$ GeV in LHCf Region A.

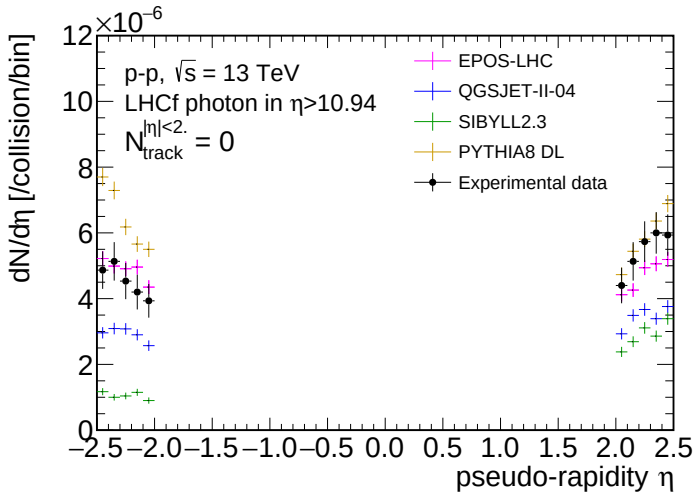

Fig. 6.8: $dN/d\eta$ in the inner detector with veto in $|\eta| < 2.0$ and a photon-like hit above $E_\gamma > 200$ GeV in LHCf Region A.

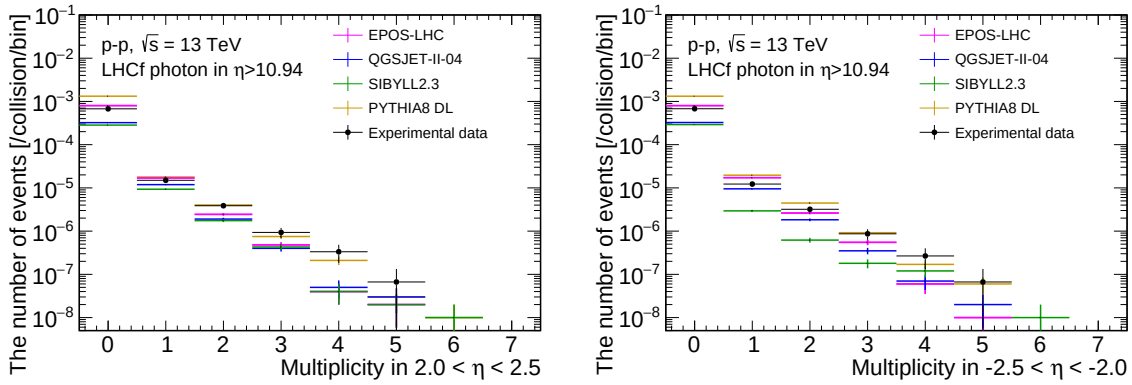

Fig. 6.9: The number of hits in $2.0 < \eta < 2.5$ (left) and $-2.5 < \eta < 2.0$ (right) with veto in $|\eta| < 2.0$ and a photon-like hit above $E_\gamma > 200$ GeV in LHCf Region A.

	model for the calculation of the response matrix	
	PYTHIA8 DL	EPOS-LHC
$C^{\mathrm{SD,unfolded}}_{N_{\mathrm{ch}}=0}$	0.452 ± 0.018	0.502 ± 0.020
X	1.12 ± 0.04	1.04 ± 0.04

Table 6.4: $C^{\mathrm{SD,unfolded}}_{N_{\mathrm{ch}}=0}$ and X calculated with four hadronic interaction models for the calculation.

	model for ND subtraction in Step (i)			
	PYTHIA8 DL	EPOS-LHC	QGSJET II-04	SIBYLL 2.3
$C^{\mathrm{SD,unfolded}}_{N_{\mathrm{ch}}=0}$	0.485 ± 0.018	0.502 ± 0.020	0.527 ± 0.019	0.493 ± 0.020

Table 6.5: $C^{\mathrm{SD,unfolded}}_{N_{\mathrm{ch}}=0}$ calculated with EPOS-LHC for calculations in step (ii) and (iii) and four hadronic interaction models for calculations of ND subtraction in step (i).

6.8 The result of SD fraction

The SD fraction in the very forward photon sample with $N_{\mathrm{ch}} = 0$ are measured using the method in Sec. 6.6. For fraction calculations in the method, we adopt EPOS-LHC and PYTHIA8 DL for hadronic interaction models, since they show better agreements with data as discussed in Sec. 6.7.2. The number of events in SD-rich and DD-rich samples is 1441 and 1325, respectively. Calculations in Step (i) to (iii) are applied using these numbers. Results of Step (iii) are illustrated in Tab. 6.4. The SD fraction for very forward photons with $N_{\mathrm{ch}} = 0$ selections calculated in Step (iv) is illustrated in Fig. 6.10.

6.9 Systematic uncertainty

The systematic uncertainties for the SD fraction in the sample are caused by the detector simulations, treatments of contamination of non-diffraction, hadronic interaction models, and the bias of the method.

- Treatments of contamination of non-diffraction

  The efficiency of the MBTS detector for ND events is estimated to be 80-100% using ATLAS full simulation. In step (i), ND contamination is subtracted with assuming 100% efficiency for ND events. Systematic uncertainty due to this efficiency is estimated by varying the efficiency for ND from 100% to 80%; 80% of ND events hit in one side of the MBTS detector. With 80% efficiency, 80% and 16% of ND events are included in the DD-rich sample and the SD-rich sample, respectively. In Eq. (6.1) in step (i), the estimated number of ND events are subtracted from the DD-rich sample. In the calculation of this systematic uncertainty, 80% and 16% of ND events are subtracted from the DD-rich and SD-rich samples, respectively, as following equations,

$$N'_{\mathrm{DD-rich}} = N_{\mathrm{DD-rich}} - 0.80 \times N^{\mathrm{Estimated\,ND}}_{N_{\mathrm{track}}=0},, \tag{6.10}$$

$$N'_{\mathrm{SD-rich}} = N_{\mathrm{SD-rich}} - 0.16 \times N^{\mathrm{Estimated\,ND}}_{N_{\mathrm{track}}=0},, \tag{6.11}$$

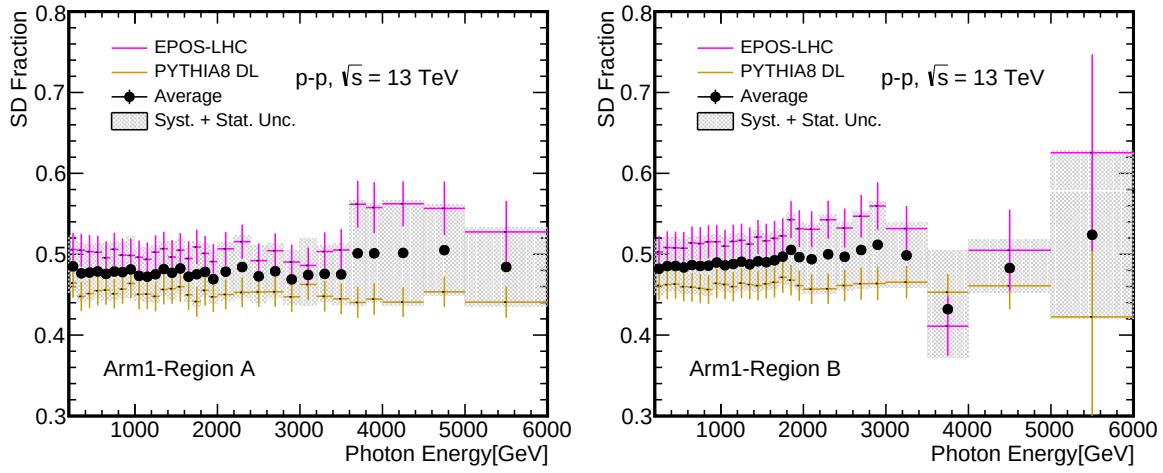

Fig. 6.10: Energy dependent SD fractions calculated in step (iv). Calculations using EPOS-LHC and PYTHIA8 DL are shown in magenta and yellow markers, respectively. The average value and bias uncertainty are shown in black markers and hatched regions, respectively.

where $N^{\text{Estimated ND}}_{N_{\text{track}}=0}$ is calculated as,

$$N^{\text{Estimated ND}}_{N_{\text{track}}=0} = N^{\text{data}}_{N_{\text{track}}=0} \times \frac{N^{\text{ND,MC}}_{N_{\text{track}}=0}}{N^{\text{SD,MC}}_{N_{\text{track}}=0} + N^{\text{DD,MC}}_{N_{\text{track}}=0} + N^{\text{ND,MC}}_{N_{\text{track}}=0}}. \tag{6.12}$$

$N'_{\text{SD}-\text{rich}}$ and $N'_{\text{DD}-\text{rich}}$ calculated by Eqs. (6.11) and (6.10) are adopted in the calculations after step (ii). The results of this sytematic uncertainty are shown in Tab. 6.10. The size of normalized systematic uncertainty is -1.79% for the SD fraction with EPOS-LHC for fraction calculations.

- LHCf detector response function

  The LHCf detector response function is utilized to emulate the detector response. The performance of the response function was evaluated using the LHCf MC sample (c). The performance parameter κ is defined as,

$$\kappa = \frac{N^{\text{response}} - N^{\text{full simulation}}}{N^{\text{response}}}, \tag{6.13}$$

  where N^{response} is the number of events from outputs of the response function. $N^{\text{full simulation}}$ is the number of events from the full detector simulation in sample (c). The parameter κ is calculated for each particle-hit type at the detector as shown in Tab. 6.6. Systematic uncertainty due to this response function is estimated with shifting outputs of response functions according to the parameter κ shown in Tab. 6.6. The results of systematic uncertainty are less than $\pm 0.7\%$, as shown in Tab. 6.9.

- Threshold of the MBTS detector

  Systematic uncertainty from differences of MBTS efficiency between data and MC is considered by changing the threshold of the MBTS detector as discussed in Ref. [62]. With changing the threshold from 0.07 pC to 0.27 pC in MC, predictions by MC match

model for full simulation	The parameter κ			
	QGSJET II-04		EPOS-LHC	
photon hit region	$\eta > 10.94$	$8.81 < \eta < 8.99$	$\eta > 10.94$	$8.81 < \eta < 8.99$
particle-hit type				
single-hit, photon	-0.0057	-0.0169	-0.0003	-0.0108
single-hit, hadron	-0.0059	0.3785	0.0478	0.0766
multi-hit, two photon	-0.0057	0.0321	-0.0057	-0.0175
multi-hit, photon and hadron	-0.0537	0.0219	0.1964	-0.0376

Table 6.6: The performance of the LHCf-Arm1 response function, κ.

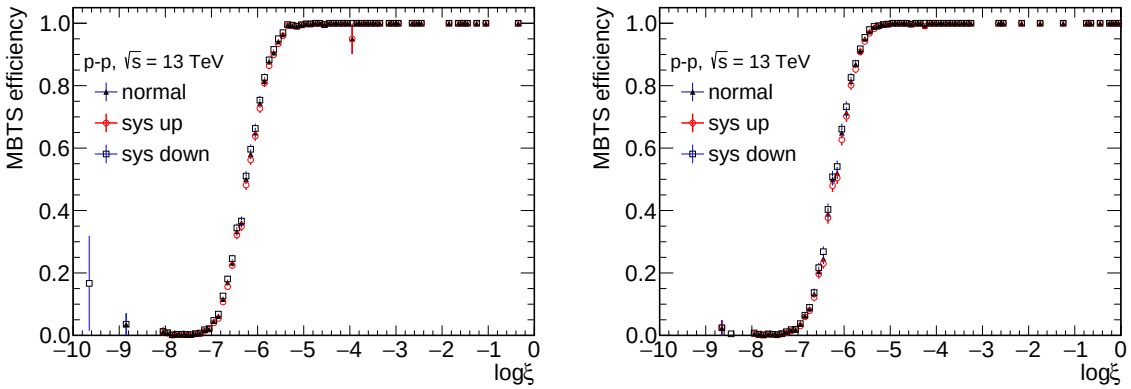

Fig. 6.11: Efficiency of the MBTS detector for Arm1 side (left) and Arm2 side (right) with inner detector veto and photon hits in the LHCf-Arm1 detector. For systematic uncertainty, the threshold of MBTS detector is changed to 0.07 pC (sys down) and 0.27 pC (sys up) in ATLAS full simulation.

the experimental data. Thus, this uncertainty is estimated using two MBTS efficiencies with 0.07 pC (sys down) and 0.27 pC (sys up) thresholds in ATLAS full simulation. Figures 6.11 illustrate the MBTS efficiency with two thresholds. $C_{N_{\rm ch}=0}^{\rm SD,unfolded}$ is calculated with these two efficiencies for systematic uncertainty of threshold of the MBTS detector. Results are summarized in Tab. 6.7.

- Hadronic interaction models for MBTS detector simulation

  MBTS efficiency is calculated from ATLAS full simulation with PYTHIA 8. To consider uncertainty in hadronic interaction models, efficiency is also calculated with EPOS-LHC. Results using MBTS efficiency with these two interaction models are compared to calculate systematic uncertainty. Systematic uncertainty from this effect is estimated to be 2.62 % for the SD fraction with EPOS-LHC for the fraction calculations. Results are summarized in Tab. 6.8.

- Hadronic interaction models for fraction calculations

  Calculations in steps (i) to (iv) are performed with two hadronic interaction models, PYTHIA8 DL and EPOS-LHC. The average of two estimated results is considered as the center value of the results. Differences between the two results are treated as systematic uncertainty due to interaction models in calculations.

- Bias of the method

$C^{\mathrm{SD,unfolded}}_{N_{\mathrm{ch}}=0}$	model for calculations	
	PYTHIA8 DL	EPOS-LHC
normal	0.4523	0.5018
up	0.4517	0.4995
difference in %	-0.13	-0.45
down	0.4519	0.5035
difference in %	-0.08	0.33

Table 6.7: Systematic uncertainty for the SD fraction owing to the threshold of the MBTS detector

$C^{\mathrm{SD,unfolded}}_{N_{\mathrm{ch}}=0}$	model for the calculation	
	PYTHIA8 DL	EPOS-LHC
model for MBTS efficiency		
PYTHIA 8	0.452	0.502
EPOS	0.460	0.515
difference to PYTHIA8 [%]	1.78	2.62

Table 6.8: $C^{\mathrm{SD,unfolded}}_{N_{\mathrm{ch}}=0}$ for two MBTS efficiencies calculated with PYTHIA 8 and EPOS.

From the validation of the method in Sec. 6.7.1, the biases of the method are observed. Bias ,Δ, defined as

$$\Delta = \frac{C^{\mathrm{estimated}} - C^{\mathrm{MC\ true}}}{C^{\mathrm{MC\ true}}} \times 100 \tag{6.14}$$

is calculated for each case and summarized in Tabs. 6.12 and 6.13 for the SD fraction in Region A and Region B, respectively.

These uncertainties except for bias-related uncertainties are summarized in Tab. 6.11. The uncertainties from hadronic interaction models for fraction calculations and bias, hereafter we call them bias uncertainty, are calculated as follows; two values are calculated for each model in calculations: the result of step (iv) and the value calculated by shifting the result of step (iv) by Δ. Since two models are considered in calculations, four values are calculated for each case. The center value is calculated from the average of the results of step (iv). In four values, the farthest values for the canter value in the upper and the lower direction are treated as the upper and lower limit of the bias uncertainty.

The result of the fraction C^{SD} is

$$C^{\mathrm{SD}}_{N_{\mathrm{ch}}=0,\mathrm{Region\ A}} = 0.477 \pm 0.019(\mathrm{stat.})^{+0.013}_{-0.009}(\mathrm{syst.(resp.)}) \pm 0.025(\mathrm{syst.(bias)}). \tag{6.15}$$

With considering conversions from Region A to Region B using the factor X, SD fraction with photons in Region B is calculated as,

$$C^{\mathrm{SD}}_{N_{\mathrm{ch}}=0,\mathrm{Region\ B}} = 0.487 \pm 0.019(\mathrm{stat.})^{+0.013}_{-0.009}(\mathrm{syst.(resp.)}) \pm 0.025(\mathrm{syst.(bias)}). \tag{6.16}$$

The uncertainty for energy-dependent fractions is calculated for each bin considering uncertainties propagated from the factor X and bias uncertainty. These uncertainties are illustrated in Fig. 6.12. In Fig. 6.12, yellow dashed lines labeled as "Csd(X stat)" and magenta dashed lines labeled as "Csd (X syst.)" correspond to statistical and systematic uncertainties propagated from calculations in step (i) to (iii), respectively. Green dash lines labeled as "Csd(Model)" corresponds to the bias uncertainty. The SD fraction and its predictions by hadronic interaction models are illustrated in Fig. 6.13. EPOS-LHC shows good agreements with data and PYTHIA8 DL agrees with data. QGSJET II-04 and SIBYLL 2.3 show much larger SD fractions than measured results.

$C_{N_{\rm ch}=0}^{\rm SD,unfolded}$	model for the calculation	
	PYTHIA8 DL	EPOS-LHC
normal	0.448	0.508
systematic (EPOS-LHC)	0.447	0.505
difference in %	-0.20	-0.66
systematic (QGSJET II-04)	0.448 0.509	
difference in %	0.06	0.18

Table 6.9: Systematic uncertainty of $C_{N_{\rm ch}=0}^{\rm SD,unfolded}$ owing to the LHCf-Arm1 response function.

$C_{N_{\rm ch}=0}^{\rm SD,unfolded}$	model for the calculation	
	PYTHIA8 DL	EPOS-LHC
efficiency 100%	0.452	0.502
efficiency 80%	0.449	0.493
difference in %	-0.67	-1.79

Table 6.10: Systematic uncertainty of $C_{N_{\rm ch}=0}^{\rm SD,unfolded}$ owing to assumption in the ND subtraction.

source of uncertainty	model for the calculation	
	PYTHIA8 DL	EPOS-LHC
MBTS threshold		
up	-0.12	-0.45
down	-0.08	0.33
MBTS model	1.78	2.62
LHCf response function		
systematic (EPOS-LHC)	-0.20	-0.66
systematic (QGSJET II-04)	0.06	0.18
ND subtraction	-0.67	-1.79
total systematic uncertainty		
upper	1.78	2.67
lower	-0.70	-1.94

Table 6.11: Summary of systematic uncertainty for $C_{N_{\rm ch}=0}^{\rm SD,unfolded}$.

	The size of bias Δ [%] model for the calculation	
	PYTHIA8 DL	EPOS-LHC
Dummy data sample		
PYTHIA8 DL	0.0	-9.1
EPOS-LHC	11.0	0.0

Table 6.12: The size of bias Δ calculated from the Tab. 6.2 for SD fractions with photon hits in Region A.

	The size of bias Δ [%] model for the calculation	
	PYTHIA8 DL	EPOS-LHC
Dummy data sample		
PYTHIA8 DL	0.0	-8.8
EPOS-LHC	10.7	0.0

Table 6.13: The size of bias Δ calculated from the Tab. 6.2 for SD fractions with photon hits in Region B.

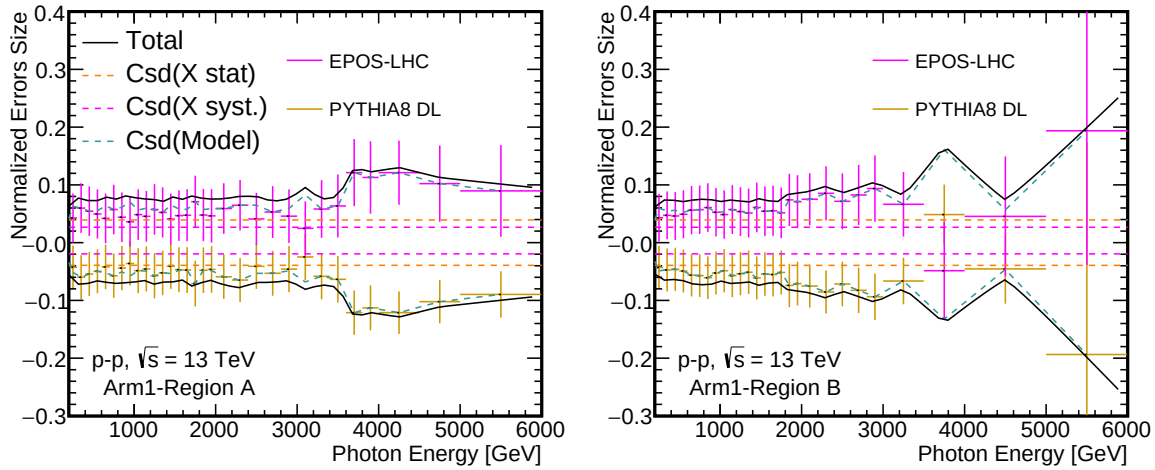

Fig. 6.12: Normalized systematic uncertainty for SD fractions. Yellow and magenta dashed lines show statistical and systematic uncertainties from calculations in step (i)-(iii), respectively. Green dashed line shows the bias uncertainty.

6.10 The spectrum of very forward photons from SD

Very forward photon spectra from SD are obtained by applying correction factors of the SD faction to the $N_{\rm ch} = 0$ spectrum. Correction factors applied for very forward photon spectra with $N_{\rm ch} = 0$ are the SD fraction calculated in the previous sections and the correction factor to convert definitions from $N_{\rm ch} = 0$ to $\log_{10}(\xi) < -5.0$, $C^{N_{\rm ch}=0\to\log_{10}(\xi)<-5.0}$. Therefore, very forward photon spectra from SD are driven by the following equations;

$$\frac{d\sigma_\gamma^{\rm SD}}{dE_\gamma} = C^{N_{\rm ch}=0\to\log_{10}(\xi)<-5.0} C^{SD} \frac{d\sigma^{N_{\rm ch}=0}}{dE}, \tag{6.17}$$

where $\frac{d\sigma^{N_{\rm ch}=0}}{dE}$ is the photon spectrum presented in Ref. [72] with some updates. $C^{N_{\rm ch}=0\to\log_{10}(\xi)<-5.0}$ is calculated from simulations as illustrated in Fig. 6.14.

Figures 6.15 illustrate $\frac{d\sigma_\gamma^{\rm SD}}{dE_\gamma}$ obtained in this analysis. Figures 6.16 illustrate ratios of MC predictions to data for Figs. 6.15. EPOS-LHC shows good agreements with data for both Region A and B. PYTHIA8 DL and MBR agree with data for $E_\gamma < 3$ TeV in Region A, whereas they overestimate for high energy. QGSJET II-04 underestimates for low energy: $E_\gamma < 3$ TeV for Region A and $E_\gamma < 2$ TeV for Region B. SIBYLL 2.3 underestimates for $1 < E_\gamma < 4.5$ TeV in Region A. We discuss details of differences between data and predictions in the next chapter.

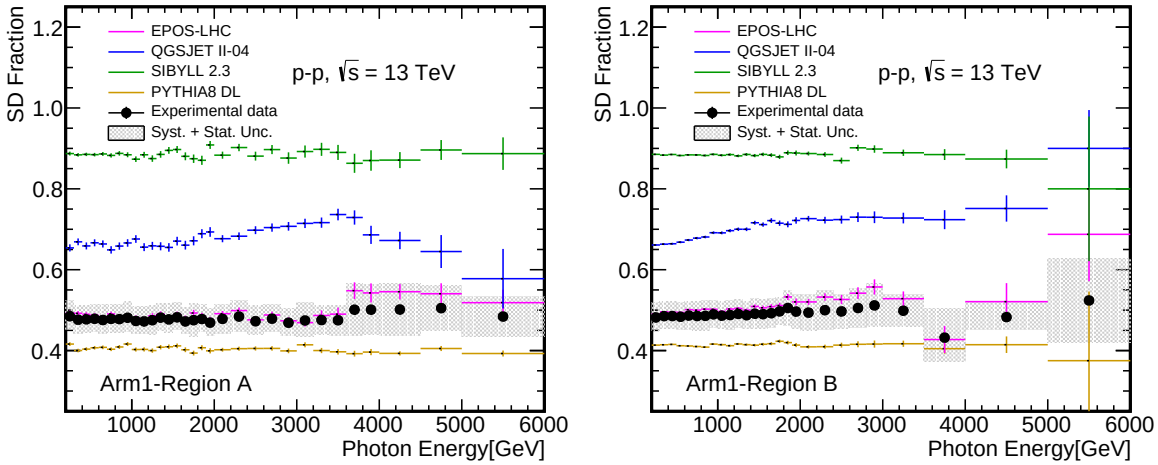

Fig. 6.13: SD fractions measured by ATLAS and LHCf detectors and predicted by hadronic interaction models.

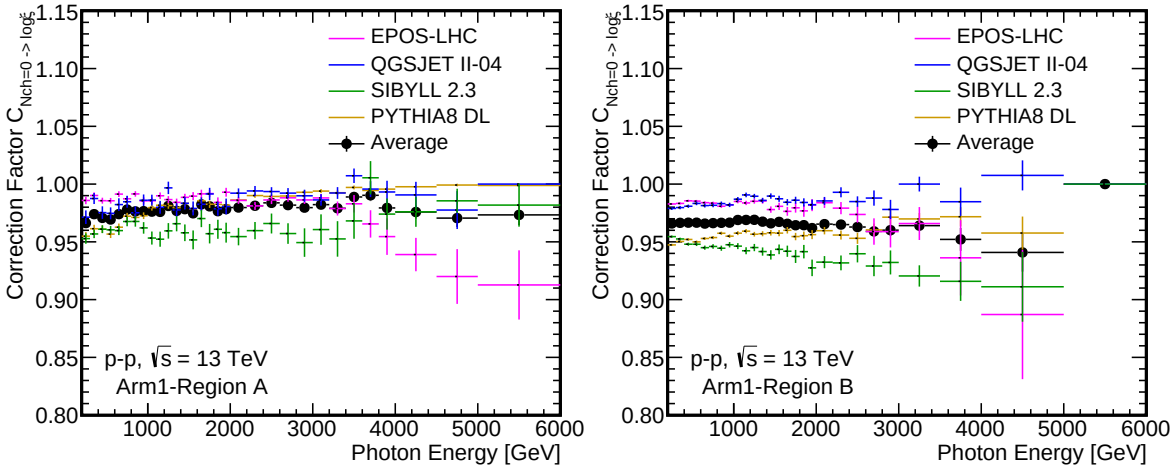

Fig. 6.14: Correction factor $C^{N_{\mathrm{charged}}=0\to\log_{10}(\xi)<-5.}$ for SD spectrum.

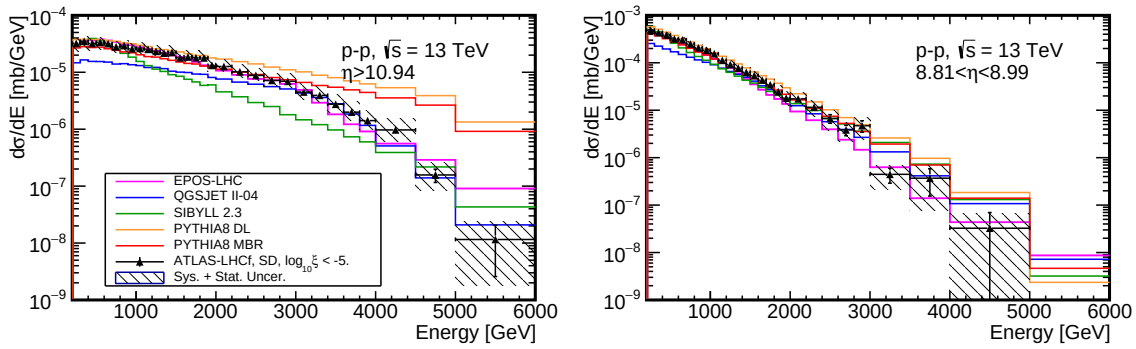

Fig. 6.15: $\frac{d\sigma_\gamma^{\mathrm{SD}}}{dE_\gamma}$ for photons hit in Ration A (left) and Region B (right).

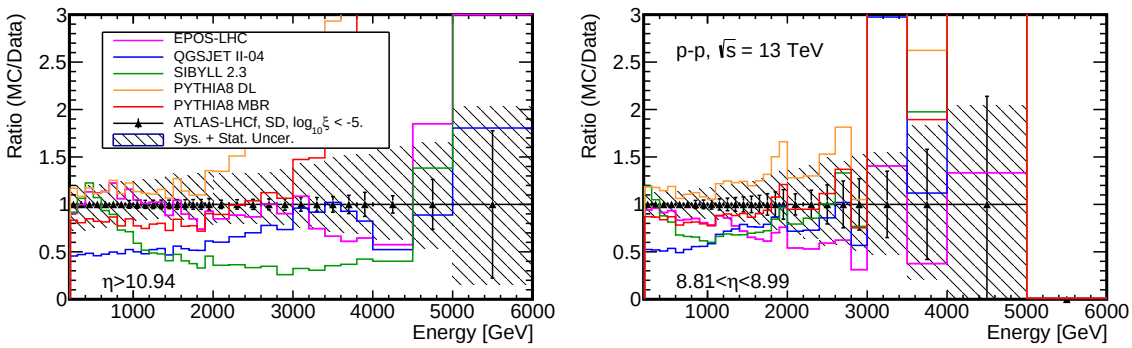

Fig. 6.16: Ratios of MC to data for Figs. 6.15

Chapter 7

Discussion

7.1 Low diffractive-mass events and very forward photons measured by ATLAS-LHCf joint analysis

Large systematic uncertainty in cross-section measurements of SD and DD by the CMS and ALICE experiments [29, 30] was mainly caused by the fact that $d\sigma/d\log_{10}\xi$ for low diffractive-mass regions was not measured so far. In these experiments, extrapolation for low diffractive-mass regions were performed based on the measurements of $d\sigma/d\log_{10}\xi$ for higher diffractive-mass regions and hadronic interaction models. To reduce the systematic uncertainty, direct measurements of very forward photons produced in $\log_{10}\xi < -5.0$ of SD were performed in Chap. 6. In this section, we discuss $d\sigma/d\log_{10}\xi$ for low diffractive-mass regions using results obtained in Chap. 6.

Firstly, we focus on diffractive-mass dependencies of very forward photons from SD. Figures 7.1 illustrate spectra of very forward photon from SD for three diffractive-mass regions predicted by EPOS-LHC. Photons from SD with $\log_{10}\xi < -7.5$ produced in $\eta > 10.94$ show harder spectrum than other diffractive-mass regions and are dominant contributions. Photons from SD with $\log_{10}\xi > -7.5$ are dominant above 2 TeV for $8.81 < \eta < 8.99$. There are no clear differences in the shape between spectra for $-7.5 < \log_{10}\xi < -6.5$ and $-6.5 < \log_{10}\xi < -5.0$. These features suggest the possibility of measurements of $d\sigma^{\mathrm{SD}}/d\log_{10}\xi$ for low diffractive-mass regions from the energy spectrum of very forward photon.

Particle productions in diffractive dissociation affect very forward photon productions from SD. For measurements of $d\sigma^{\mathrm{SD}}/d\log_{10}\xi$ from the photon energy spectrum, the rate of photon productions per diffractive dissociation and the shape of the energy spectrum is important, since this rate and shape can change the energy spectrum for each diffractive-mass region. There are, however, large differences in predictions of particle productions among hadronic interaction models. Figures 7.2 illustrate spectra of very forward photon predicted by QGSJET II-04. From comparison between Figs. 7.1 and 7.2, we can find differences in the shape of spectra due to predictions of particle productions. There are large differences in the rate of photon production. The left plot of Fig. 7.3 illustrates the number of SD events with $\mathrm{N_{ch}} = 0$. The right plot illustrates the one with additionally requiring one photon with $E_\gamma > 200$ GeV in the LHCf-Arm1 Region A. By requiring photon productions in LHCf-Arm1 Region A, a number of events are significantly changed; QGSJET II-04 predicts the largest number of events in $-7.5 < \log_{10}\xi < -6.5$ of the left plot, whereas the number

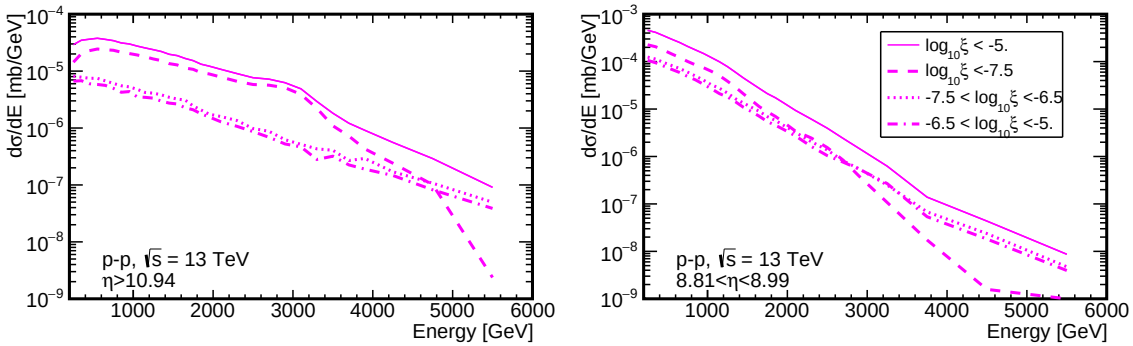

Fig. 7.1: Photon spectrum from SD with $\log_{10}\xi < -5.$ (solid line), $\log_{10}\xi < -7.5$ (dashed line), $-7.5 < \log_{10}\xi < -6.5$ (dotted line), $-6.5 < \log_{10}\xi < -5.$ (dash-dotted line) for EPOS-LHC.

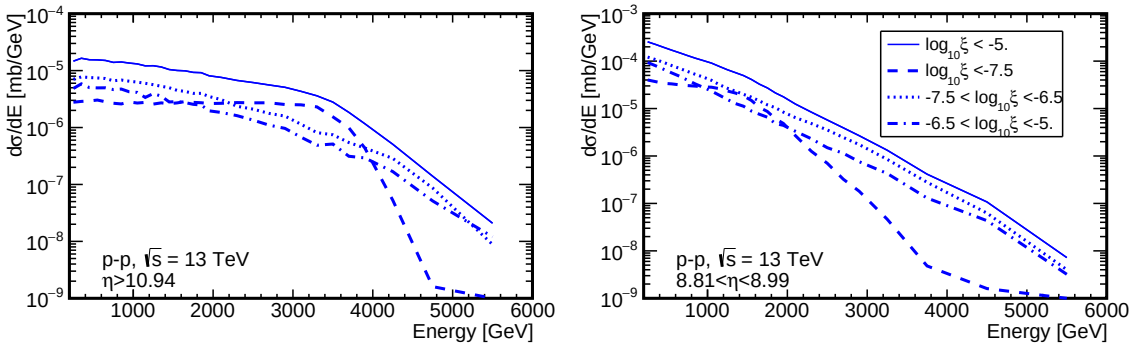

Fig. 7.2: Photon spectrum from SD with $\log_{10}\xi < -5.$ (solid line), $\log_{10}\xi < -7.5$ (dashed line), $-7.5 < \log_{10}\xi < -6.5$ (dotted line), $-6.5 < \log_{10}\xi < -5.$ (dash-dotted line) for QGSJET II-04.

of events predicted by QGSJET II-04 is much smaller than those by PYTHIA8 DL in the right plot. In consequence, we would be able to measure $d\sigma^{\rm SD}/d\log_{10}\xi$ for low diffractive-mass regions from the energy spectrum of very forward photons, whereas the discussion strongly depends on the modeling of particle productions. In other words, large systematic uncertainty is expected to measurements of cross-sections for SD by the very forward photon spectrum, due to uncertainty in the photon production mechanism.

By assuming one particular model for particle productions, we can validate $d\sigma^{\rm SD}/d\log_{10}\xi$ for low diffractive-mass regions using results in Chapt. 6. In particular, we focus on PYTHIA8 MBR, since it was adopted for extrapolation of low diffractive mass regions by the CMS experiment [29]. In the next section, we discuss the validity of PYTHIA8 MBR. PYTHIA8 has parameters for particle productions. Moreover, the MBR parameterization in PYTHIA8 has two parameters to change the cross-sections and its diffractive-mass dependencies. In this chapter, we firstly tune a parameter for particle productions using the ratio of photon spectrum with $N_{\rm ch} = 0$ to inclusive spectrum illustrated in Fig. 6.2. Secondary, we tune two parameters for diffractive dissociation to reproduce photon spectrum from SD by the ATLAS and LHCf experiments discussed in Chap. 6. Finally, we discuss the effects on $\langle X_{\rm max}\rangle$ and future prospects in Sec. 7.3 and 7.4, respectively.

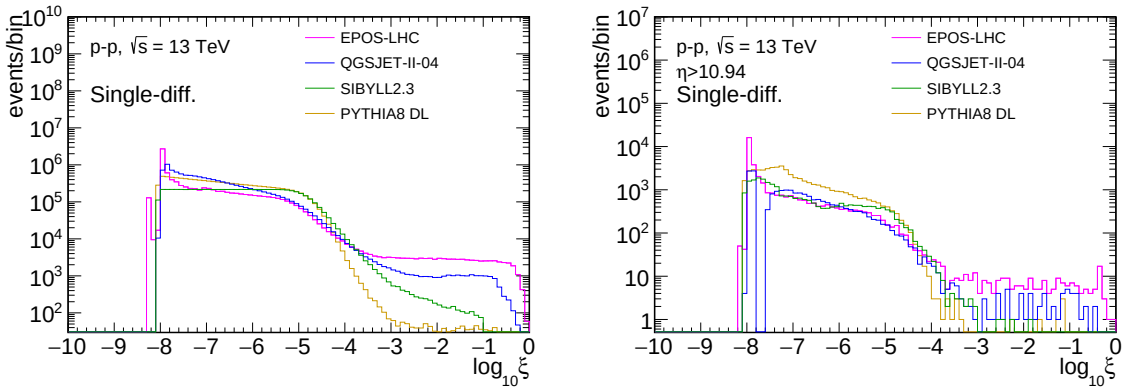

Fig. 7.3: (left) Diffractive mass dependencies of the number of SD events with $\mathrm{N_{ch}} = 0$. (right) Diffractive mass dependencies with additionally requiring one photon with $E_\gamma > 200$ GeV in the LHCf-Arm1 Region A to the left plot.

7.2 Validation of PYTHIA8 MBR using results by ATLAS-LHCf common analysis

7.2.1 Tuning of particle productions in PYTHIA8 MBR.

Large differences in the shape of photon spectrum between measurements and predictions by PYTHIA8 MBR were found in Fig. 6.15. These large differences in shape are caused by the photon production mechanism in PYTHIA8 MBR. In this section, tuning of a parameter related to photon production is performed. The parameter $\mathrm{StringFlav :: popcornRate}$ is the parameter to control the popcorn model [87], the mechanism to produce high-energy meson efficiently. To have a better modeling of particle productions, the parameter are changed into 0.0, 0.1, 0.2, 0.3, and 0.4, where default value of $\mathrm{popcornRate}$ is 0.5. Figure 7.4 illustrates the ratio of photon spectrum with $N_{\mathrm{ch}} = 0$ to inclusive photon spectrum. Predictions of PYTHIA8 MBR with several cases of $\mathrm{StringFlav :: popcornRate}$ are also shown. A kink structure in measurements of the ratio is mainly caused by the shape of the photon spectrum by diffractive dissociation. Only the spectrum with $\mathrm{StringFlav :: popcornRate} = 0.0$ reproduces the kink structure. Therefore, $\mathrm{StringFlav :: popcornRate} = 0.0$ is the best value of the parameter for very forward photon productions. Hereafter, we utilize PYTHIA8 with $\mathrm{popcornRate} = 0.0$.

7.2.2 Tuning of the pomeron trajectory parameters in PYTHIA8 MBR

Pomeron trajectory parameters ϵ and α', parameters in Eq. (3.8) in the modeling of PYTHIA8, in PYTHIA8 MBR affect $d\sigma/d\log_{10}\xi$. In this section, we compare several parametrization of pomeron trajectory parameters with assuming $\mathrm{popcornRate} = 0.0$. Table 7.1 illustrates parameters for prepared samples. The default vale of PYTHIA8 MBR is $\mathrm{popcornRate} = 0.5$, $\epsilon = 0.104$, and $\alpha' = 0.25$ GeV^{-2}. Comparison of the photon spectrum with $N_{\mathrm{ch}} = 0$ and from SD with $\log_{10}\xi < -5.0$ are illustrated in Figs. 7.5 and 7.6, respectively. With $\mathrm{popcornRate} = 0.0$, predictions of PYTHIA8 MBR with larger ϵ show better agreements with data. Differences between green and yellow lines are very small. Thus, the effect of

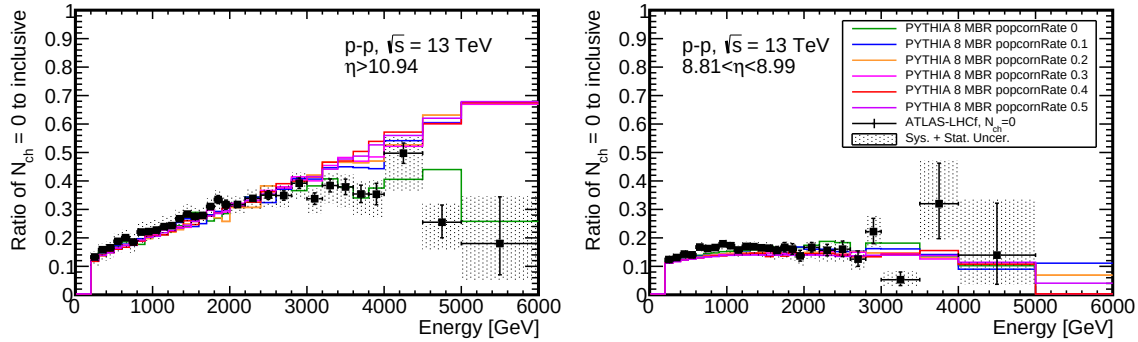

Fig. 7.4: The ratio of photon spectrum with $N_{\rm ch} = 0$ to inclusive photon spectrum for $\eta > 10.94$ (left) and $8.81 < \eta < 8.99$ (right). Predictions by PYTHIA8 MBR with several StringFlav :: popcornRate cases are also shown. Experimental results are taken from Ref. [72] with some update.

change of the parameter α' from $0.25\ \mathrm{GeV}^{-2}$ to $0.125\ \mathrm{GeV}^{-2}$ is small. Larger ϵ corresponds to larger cross-sections for low diffractive-mass events with $\log_{10}\xi < -7.0$. Therefore, large low diffractive-mass cross-sections are preferred.

To have agreements with data for photon spectrum from SD, the parameter ϵ is increased as much as possible in PYTHIA8 MBR. The results are illustrated in Figs. 7.7 and 7.8. Ratios of MC predictions to data are illustrated in Figs. 7.9 and 7.10. The upper limit of ϵ in PYTHIA8 MBR is 0.15. To check differences between data and predictions, reduced χ^2 was calculated as follows,

$$\chi^2/n = \frac{1}{n}\sum \frac{(N^{\rm data} - N^{\rm PYTHIA\ MBR})^2}{(\sigma^{\rm data})^2 + (\sigma_{stat}^{\rm PYTHIA\ MBR})^2}, \tag{7.1}$$

where n is the number of degree of freedom. $N^{\rm data}$ and $N^{\rm PYTHIA\ MBR}$ are the number of events of experimental data and predictions by PYTHIA8 MBR in each bin. $\sigma^{\rm data}$ is the total error of experimental data. $\sigma_{stat}^{\rm PYTHIA\ MBR}$ is the statistical error of simulation. The reduced χ^2 calculated for each prediction by PYTHIA8 MBR in Fig. 7.6 and 7.8 is shown in Tab. 7.2. For $8.81 < \eta < 8.99$, MBR with $\epsilon = 0.140$ shows the smallest reduced χ^2 and, therefore, good agreement. For $\eta > 10.94$, predictions with $\epsilon = 0.140$ or 0.150 are, however, still smaller than the measurements, especially for $2 < E_\gamma < 4$ TeV in photon energy. We cannot reproduce the very forward photon spectra from SD with changing of parameters ϵ, α' and popcornRate. According to the spectrum with diffractive-mass selections illustrated in Fig. 7.11, events in $\log_{10}\xi < -7.5$ are dominant for 1.5 to 4 TeV in $\eta > 10.94$, whereas events in $\log_{10}\xi > -7.5$ show dominant contributions for $8.81 < \eta < 8.99$. Thus, this result suggests that the number of SD events with $\log_{10}\xi < -7.5$ predicted by PYTHIA8 MBR with parametrization discussed here are not enough to reproduce the photon spectrum from SD measured in Chap. 6.

To check the performance of several cases of PYTHIA8 MBR in higher diffractive-mass regions, comparisons between experimental data by ATLAS and CMS experiments [37, 29] at $\sqrt{s} = 7$ TeV and predictions by PYTHIA8 MBR are performed using the Rivet tool version 3.1 [88]. Figures 7.12, 7.13, and 7.14 illustrate comparison between data and predictions by PYTHIA8 tunes. For all cases, PYTHIA8 MBR with $\epsilon = 0.08$ and popcornRate $= 0.0$ show better agreements with data than PYTHIA8 MBR with $\epsilon = 0.150$

	popcornRate	ϵ	α'
MBR default	0.5	0.104	0.25
MBR default popcornRate 0	0.0	0.104	0.25
MBR popcornRate 0.1	0.1	0.104	0.25
MBR popcornRate 0.2	0.2	0.104	0.25
MBR popcornRate 0.3	0.3	0.104	0.25
MBR popcornRate 0.4	0.4	0.104	0.25
MBR $\epsilon = 0.08$	0.0	0.08	0.25
MBR $\alpha' = 0.125$	0.0	0.104	0.125
MBR $\epsilon = 0.14$	0.0	0.14	0.25
MBR $\epsilon = 0.15$	0.0	0.15	0.25
DL default	0.5	0.085	0.25
DL popcornRate 0	0.0	0.085	0.25
DL $\epsilon = 0.15$	0.0	0.15	0.25

Table 7.1: Tunes of PYTHIA8 prepared for the discussion.

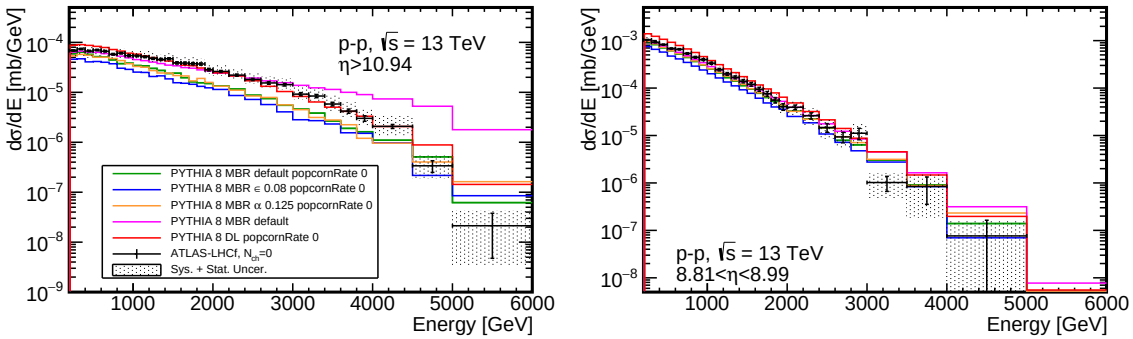

Fig. 7.5: ATLAS-LHCf very forward photon spectrum with $N_{\mathrm{ch}} = 0$ and predictions by PYTHIA 8.2 MBR tunes.

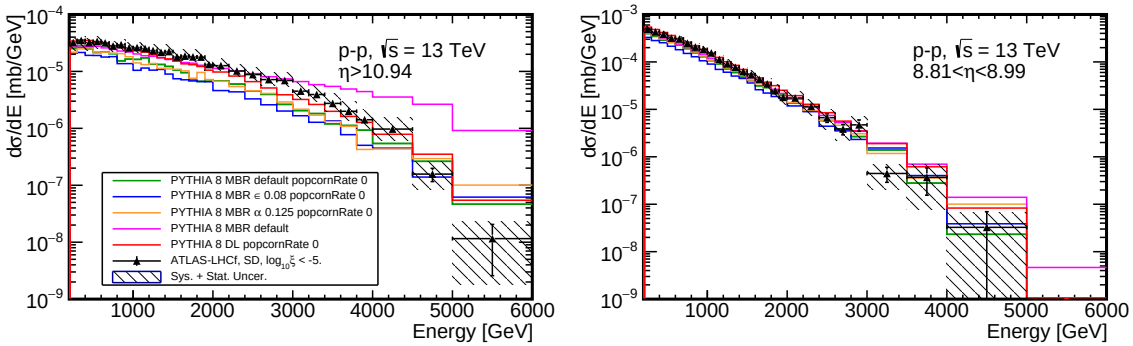

Fig. 7.6: Very forward photon spectrum from SD for $\log_{10}\xi < -5$. measured by ATLAS and LHCf detectors and predictions by PYTHIA 8.2 MBR tunes.

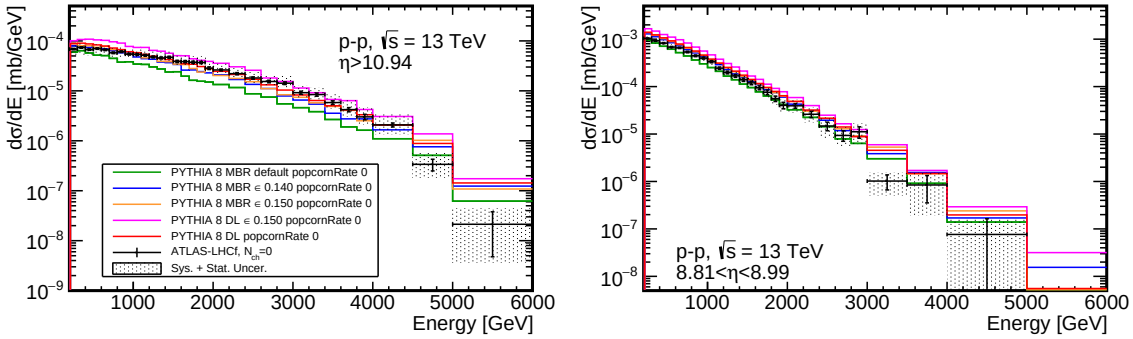

Fig. 7.7: ATLAS-LHCf very forward photon spectrum with $N_{\mathrm{ch}} = 0$ and predictions by PYTHIA 8.2 MBR tunes for very large ϵ.

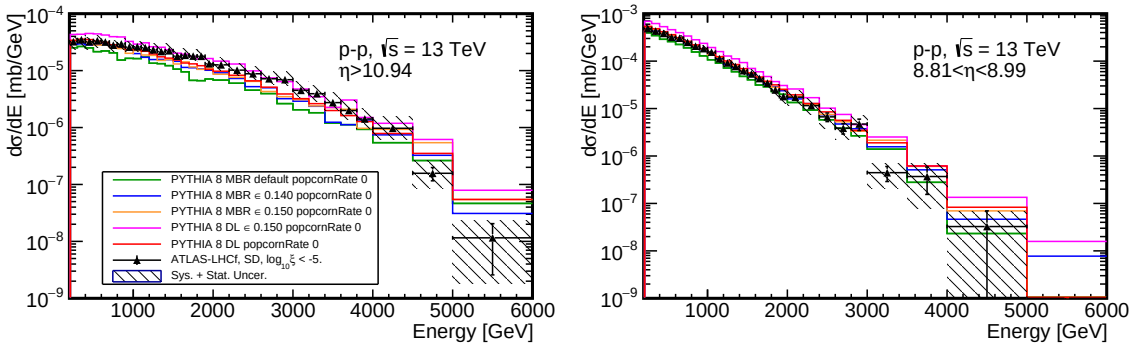

Fig. 7.8: Very forward photon spectrum from SD for $\log_{10}\xi < -5$. measured by ATLAS and LHCf detectors and predictions by PYTHIA 8.2 MBR tunes for very large ϵ.

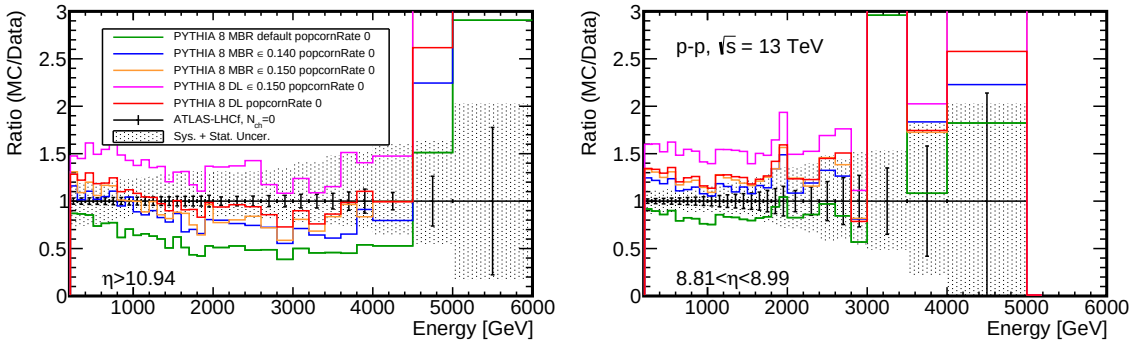

Fig. 7.9: Ratios of MC predictions to data for Fig. 7.7

	reduced χ^2	
	$\eta > 10.94$	$8.81 < \eta < 8.99$
MBR $\epsilon = 0.08$	7.06	3.98
MBR $\alpha' = 0.125$	4.69	1.45
MBR default popcornRate0	4.37	1.88
MBR $\epsilon = 0.14$	2.03	0.69
MBR $\epsilon = 0.15$	1.87	1.39

Table 7.2: Reduced χ^2 between predictions and experimental data which are shown in Figs. 7.6 and 7.8.

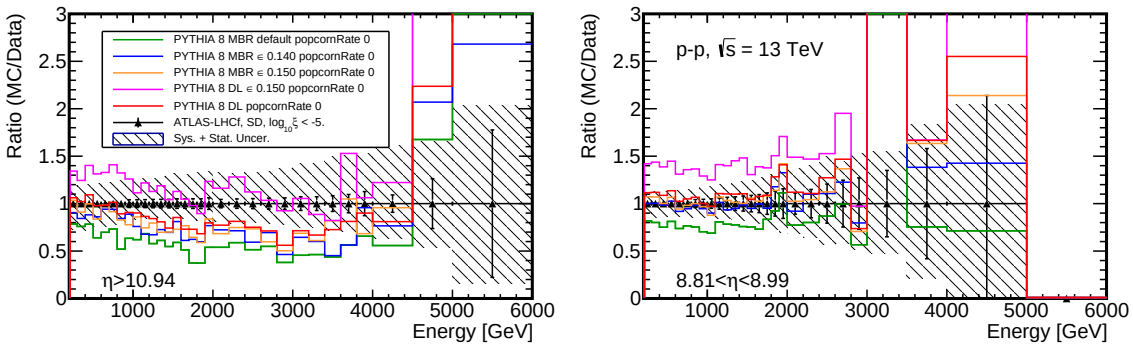

Fig. 7.10: Ratios of MC predictions to data for Fig. 7.8.

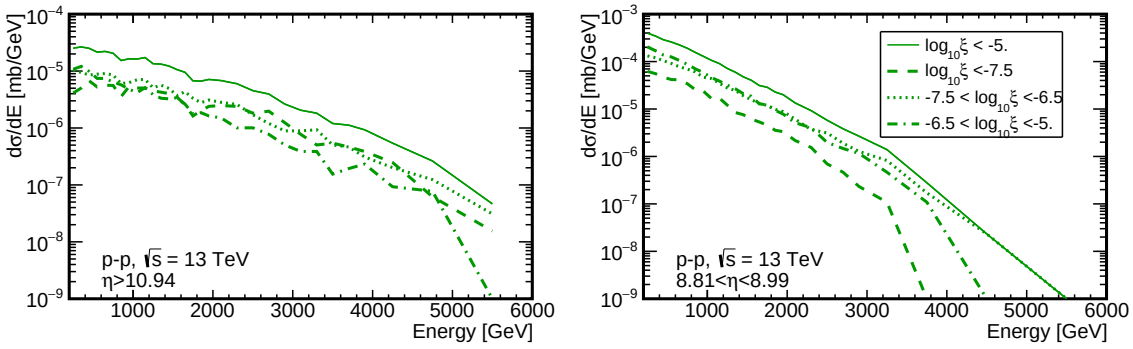

Fig. 7.11: Photon spectrum from SD with $\log_{10}\xi < -5.$ (solid line), $\log_{10}\xi < -7.5$ (dashed line), $-7.5 < \log_{10}\xi < -6.5$ (dotted line), $-6.5 < \log_{10}\xi < -5.$ (dash-dotted line) for PYTHIA8 MBR with $\epsilon = 0.104$ and $\mathrm{popcornRate} = 0.0$.

and $\mathrm{popcornRate} = 0.0$. Moreover, from comparison between PYTHIA 8.2 MBR $\epsilon = 0.08$ with $\mathrm{popcornRate} = 0.0$ (red lines) and with $\mathrm{popcornRate} = 0.5$ (green lines), the $\mathrm{popcornRate}$ parameter does not affect rapidity gaps nor cross-sections in central regions measured by the ATLAS and CMS experiments.

Figures 7.15 illustrate $d\sigma/d\log_{10}\xi$ predicted by PYTHIA8 MBR with several parametrization discussed in this section for proton-proton collisions with $\sqrt{s} = 13$ TeV (left plot) and 7 TeV (right plot). Measurements by ATLAS and LHCf detectors are sensitive to $\log_{10}\xi < -5.0$ in the left plot of Fig. 7.15. PYTHIA8 MBR with $\epsilon \leq 0.14$ and EPOS-LHC are preferred as discussed above. Measurements by ATLAS and CMS experiments are sensitive to $\log_{10}\xi > -5.5$ in the right plot of Fig. 7.15. PYTHIA8 MBR with $\epsilon = 0.08$ is preferred. Any parametrization in PYTHIA8 MBR cannot reproduce all the experimental results with assuming $\mathrm{popcornRate} = 0.0$ in particle production. A steep increase of $d\sigma^{\mathrm{SD}}/d\log_{10}\xi$ at low diffractive-mass regions is preferred. We should note that the center-of-mass energy is different between the result in the previous chapter and results by the CMS experiment discussed above, so energy dependence may also affect it.

7.3 Discussions for effects on uncertainty in $\langle X_{\mathrm{max}} \rangle$

As discussed in the previous section, predictions by PYTHIA8 MBR with $\epsilon \leq 0.104$ underestimate the measured photon spectrum by ATLAS and LHCf detectors, whereas PYTHIA8 MBR with $\epsilon = 0.08$, 0.104, and 0.07 were considered in extrapolation for cross-section measurements of SD and DD by the CMS experiment [29]. It suggests that the cross-section extrapolated by these parametrizations of PYTHIA8 MBR may be underestimated. By contrast, EPOS-LHC shows good agreements with all forward photon spectra of diffractive dissociation measured by ATLAS and LHCf detectors.

Finally, we discuss the uncertainty on $\langle X_{\mathrm{max}} \rangle$ from measurements of the CMS experiment [29] if the model which shows good agreements with measurements by ATLAS and LHCf detectors are considered. In the measurements, cross-sections for $\log_{10}\xi < -5.5$ were extrapolated for SD. Cross-sections for $\log_{10}\xi_{\mathrm{X}} < -5.5$ and $\log_{10}\xi_{\mathrm{Y}} < -6.7$ or $\log_{10}\xi_{\mathrm{X}} < -6.7$ and $\log_{10}\xi_{\mathrm{Y}} < -5.5$ were extrapolated for DD. Differences in cross-sections of SD and DD between predictions by EPOS-LHC and PYTHIA8 MBR with $\epsilon = 0.08$ for these extrapolated regions are 2.27 mb for SD and 2.24 mb for DD. Predictions of EPOS-LHC are larger than that of PYTHIA8 MBR. If we consider these differences as additional uncertainties in extrapolation of cross-sections, the uncertainty of $\langle X_{\mathrm{max}} \rangle$ estimated in Sec. 5.2.1 becomes $694.5^{+2.7}_{-1.2}$ g/cm^2. The uncertainty from results by the CMS experiment becomes 1.0 g/cm^2 larger than the value estimated in Sec. 5.2.1 if EPOS-LHC are considered in extrapolations of low diffractive-mass events.

7.4 Future prospects

Large uncertainty in particle productions of diffractive dissociation makes it challenging to measure cross-sections of SD for low diffractive-mass regions from the photon spectrum of SD discussed in Chap. 6. The uncertainty in particle productions can be constrained by future measurements. In Chap. 6, the number of events with $\mathrm{N_{ch}} = 0$, hits in the MBTS detector, and photon-like hits in the LHCf-Arm1 detector is considered. $O(10^3)$ events are measured.

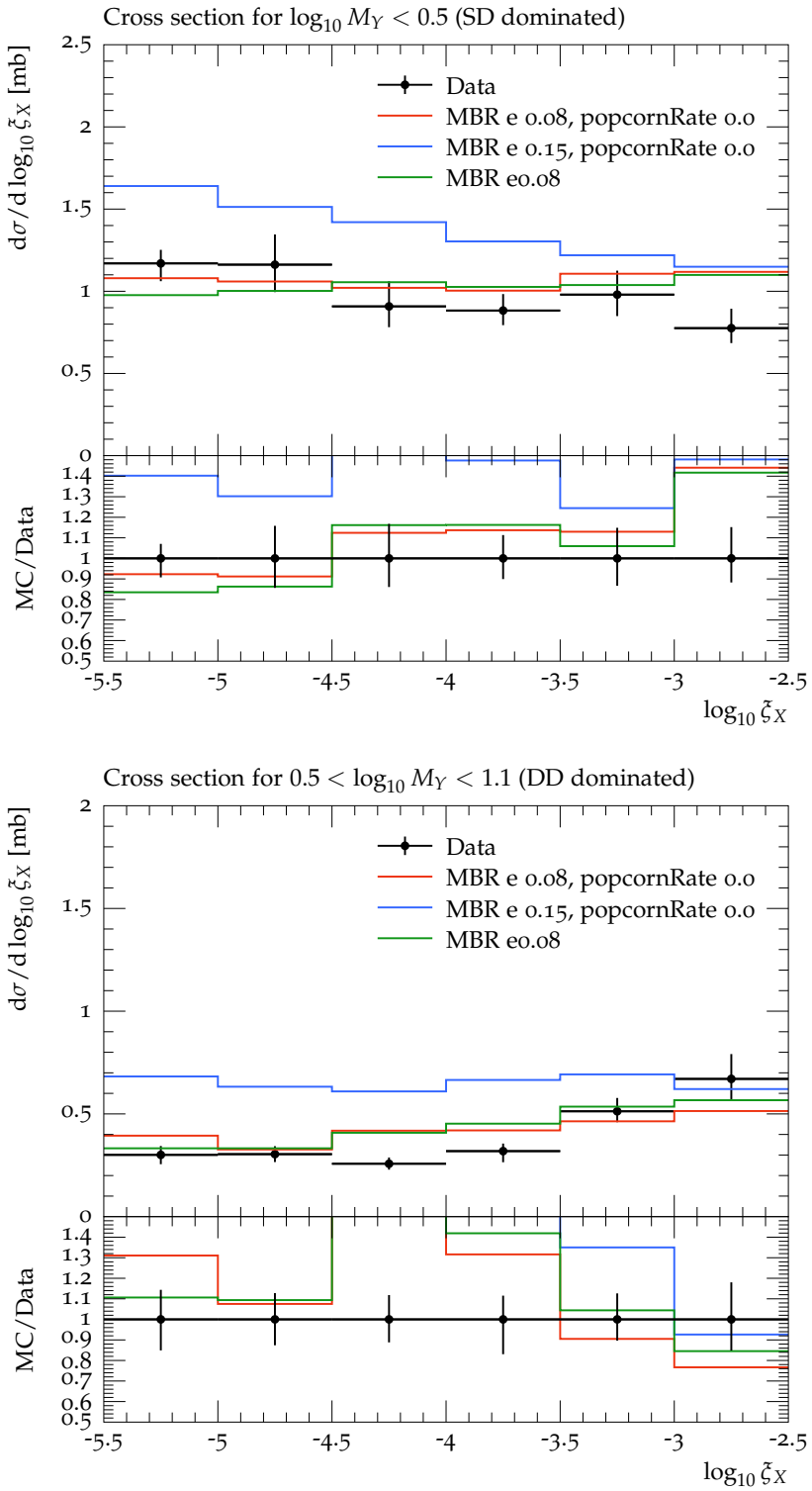

Fig. 7.12: Cross-sections for (top) $-5.5 < \log_{10}\xi < -2.5$ with $\log_{10} M_Y < 0.5$ and (bottom) $0.5 < \log_{10} M_Y < 1.1$ measured by the CMS experiment [29] and predictions by PYTHIA8 MBR with $\epsilon = 0.08$ (green line), PYTHIA8 MBR with $\epsilon = 0.08$ and $\mathrm{popcornRate} = 0.0$ (red line), and with $\epsilon = 0.15$ and $\mathrm{popcornRate} = 0.0$ (blue line). These Figures are produced with Rivet [88].

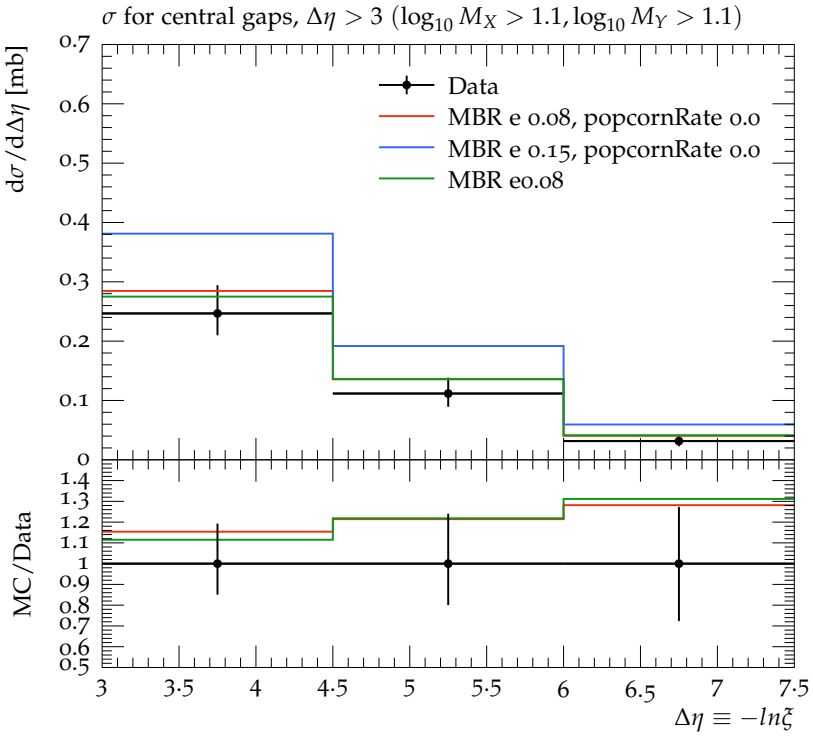

Fig. 7.13: Cross-sections for $3 < \Delta\eta < 7.5$ with $\log_{10} M_X > 1.1$ and $\log_{10} M_Y > 1.1$ measured by the CMS experiment [29] and predictions by PYTHIA8 MBR with $\epsilon = 0.08$ (green line), PYTHIA8 MBR with $\epsilon = 0.08$ and $\mathrm{popcornRate} = 0.0$ (red line), and with $\epsilon = 0.15$ and $\mathrm{popcornRate} = 0.0$ (blue line). The figure is produced with Rivet [88].

interaction model	Cross-sections for diffractive-mass region [mb] $\log_{10}\xi < -5.5$
MBR $p = 0.0, \epsilon = 0.08$	3.35
MBR $p = 0.0, \epsilon = 0.15$	5.65
EPOS-LHC	5.62
QGSJET II-04	6.79

Table 7.3: Cross-sections of SD for low diffractive-mass collisions. Proton-proton collisions with $\sqrt{s} = 7$ TeV are considered.

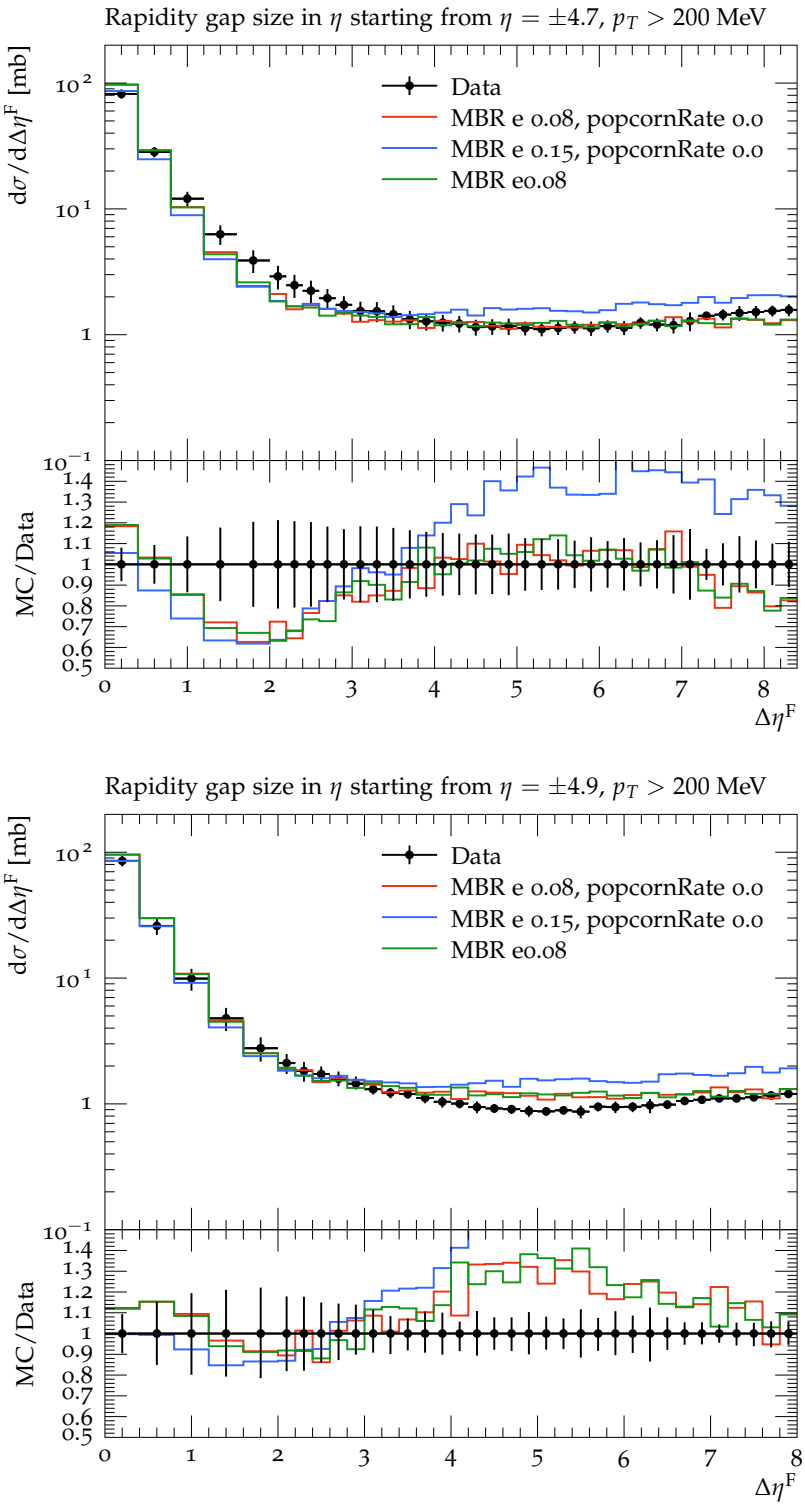

Fig. 7.14: Rapidity gap cross-sections measured by (top) the CMS experiment [29] and (bottom) the ATLAS experiment [37] Predictions by PYTHIA8 MBR with $\epsilon = 0.08$ (green line), PYTHIA8 MBR with $\epsilon = 0.08$ and $\mathrm{popcornRate} = 0.0$ (red line), and with $\epsilon = 0.15$ and $\mathrm{popcornRate} = 0.0$ (blue line) are also illustrated. These figures are produced with Rivet [88].

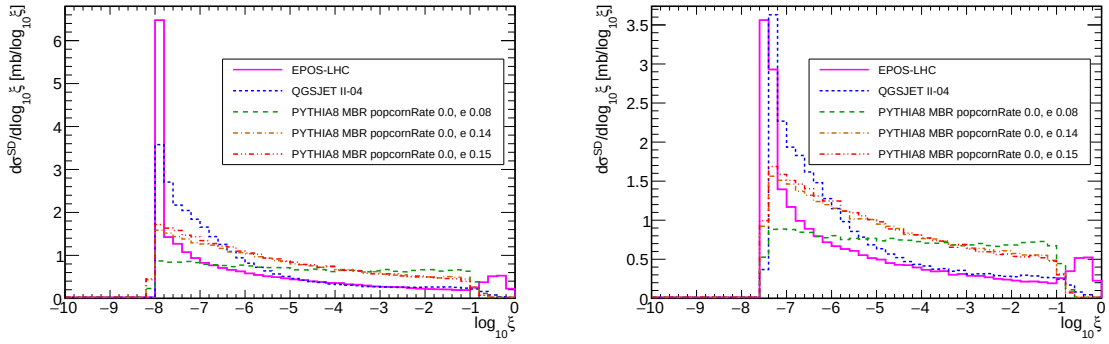

Fig. 7.15: SD ($pp \to Xp$) cross-sections $d\sigma/d\log_{10}\xi$ predicted by PYTHIA8 MBR with several parametrization discussed in this section for $\sqrt{s} = 13$ TeV (left) and $\sqrt{s} = 7$ TeV (right).

With increasing the number of events in LHC-Run3, we can measure the very forward photon spectra with $\mathrm{N_{ch}} = 0$ and hits in the MBTS detector with much larger statistics. With $\mathrm{N_{ch}} = 0$ and hits in the MBTS detector, we can select events with $\log_{10}\xi \approx -6.0$. Thus, from the measurements with higher statistics, we can constrain both the shape of the very forward photon spectrum and the photon production rate for $\log_{10}\xi \approx -6.0$. Another possibility is using the calorimeter of the ATLAS experiment. The rapidity gap cross-sections up to $\Delta\eta^{\mathrm{gap}} = 8$ are measured using the inner detector and the calorimeter of the ATLAS experiment in Ref. [37]. By combining the rapidity gap information, we can also constrain both the shape of the very forward photon spectrum and the photon production rate for different diffractive-mass regions. To constrain particle productions in $\log_{10}\xi < -7.0$, the measurement of forward neutrons in LHCf detectors with $\mathrm{N_{ch}} = 0$ by the inner detector is another possibility. By combining information of very forward photons and very forward hadrons in the same diffractive-mass regions, we can reduce uncertainty in particle productions.

With constraining the shape of spectrum and photon production rate by future experiments, we can evaluate cross-sections of $\log_{10}\xi < -7.0$ from very forward photon spectra discussed in Chap. 6. It will reduce uncertainty in diffractive dissociation and finally uncertainty in the $\langle X_{\mathrm{max}}\rangle$ prediction.

Chapter 8

Conclusion

The mass composition of UHECRs is the key information to understand their origin. There are many theoretical scenarios for the source of UHRCRs. The energy spectrum of UHECRs measured at the Earth has information of the acceleration mechanism at the sources and is modified by interactions in the propagation of UHECRs from the sources to the Earth. To understand the information of the sources, the mass composition is important information, since interactions during propagation depend on the mass composition. The energy spectrum and the mass composition of UHECRs are measured by using air showers. The mass composition is estimated by comparing measurements of $X_{\rm max}$ or N_μ with their predictions. Predictions of $X_{\rm max}$ or N_μ, however, depend on the hadronic interaction models adopted in the simulation of the air shower. For the mean of $X_{\rm max}$, differences in predictions among hadronic interaction models are approximate $\pm 14\ {\rm g/cm^2}$ for 10^{19} eV UHECRs, whereas the systematic uncertainty in measurements by the Pierre Auger Observatory is $^{+8.0}_{-7.6}\ {\rm g/cm^2}$ at the energy. This $\pm 14\ {\rm g/cm^2}$ uncertainty approximately corresponds to ± 0.5 in the mean of $\ln A$. Furthermore, the uncertainty of hadronic interactions may be underestimated by considering differences in predictions of hadronic interaction models and should be considered from the uncertainty in accelerator experiments. Due to the large uncertainty of hadronic interactions, it is challenging to interpret the mass composition from measurements of $X_{\rm max}$ or N_μ.

Hadronic interaction models have been improved using measurements at accelerator experiments. However, some measurements show very large experimental uncertainty. Due to the limitations of Quantum Chromodynamics, phenomenological models are adopted in hadronic interaction models. These phenomenological models are tuned using available experimental data measured by accelerator experiments. The latest hadronic interaction models are partially tuned with data taken at the Large Hadron Collider. Meanwhile, experimental results in cross-sections of diffractive dissociation show very large uncertainty or relay on the extrapolation by one hadronic interaction model. They affect uncertainty in hadronic interaction models. Large effects of diffractive dissociation on $X_{\rm max}$ or N_μ are discussed in the previous studies. However, the effects of SD, DD, and diffractive mass were not separated. Moreover, the definition of diffractive dissociation adopted in each experiment was not considered in these discussions. Thus, it is unclear how the uncertainties in cross-section measurements of diffractive dissociation affect predictions of $X_{\rm max}$ or N_μ.

We studied the effects of SD, DD, and diffractive mass on $X_{\rm max}$ or N_μ in air shower experiments comprehensively. The range of possible uncertainty in each characteristic of diffractive dissociation was estimated from the accelerator measurements and their uncer-

tainties. The effects of each characteristic on $X_{\rm max}$ or N_μ were estimated using the range of the uncertainty. In the estimation, we considered three observables in the air shower experiments, $X_{\rm max}$, $X^\mu_{\rm max}$, and N_μ, and two characteristics of diffractive dissociation, *i.e.* fractions of collision types in diffractive dissociation and diffractive-mass dependencies in cross-sections. We found that effects of the fraction of diffractive dissociation in inelastic collisions are $6.7 - 9.1$ g/cm^2 and $7.3 - 10.4$ g/cm^2 at maximum on $\langle X_{\rm max}\rangle$ and $\langle X^\mu_{\rm max}\rangle$, respectively. These sizes of the effects correspond to one-third of current differences in predictions among hadronic interaction models. Effects of both diffractive mass and fractions between SD and DD are less than 2 g/cm^2 on $X_{\rm max}$ and $X^\mu_{\rm max}$ and a few % on N_μ. Diffractive dissociation is not the source of the muon deficit problem.

Uncertainty in $\langle X_{\rm max}\rangle$ from experimental uncertainty in cross-sections measurements of SD and DD was estimated by focusing on the fraction of diffractive dissociation in inelastic collisions. Simulated air showers were categorized by the definition of each experiment. The uncertainty from experimental uncertainty in cross-section measurements in $\langle X_{\rm max}\rangle$ was estimated using the categorized simulated samples. The uncertainty propagated from cross-section measurements of SD and DD by the CMS and ALICE experiments was estimated to be $^{+1.7}_{-1.2}$ g/cm^2 and $^{+4.0}_{-5.6}$ g/cm^2, respectively. Substantially large uncertainty in $\langle X_{\rm max}\rangle$ was caused by measurements by the ALICE experiment. For the CMS experiment, estimated uncertainty in $\langle X_{\rm max}\rangle$ was not so large, whereas this result is valid if PYTHIA8 MBR adopted in extrapolations for low diffractive-mass events is valid. The main source of uncertainty in experiments is cross-sections of low diffractive-mass events. This result is the first clarification of the relations between experimental uncertainty of cross-section measurements and uncertainty in $\langle X_{\rm max}\rangle$. The size of these uncertainties propagated from cross-section measurements of diffractive dissociation is comparable with one of the dominant sources of systematic uncertainty in measurements by PAO. Therefore, cross-section measurements of diffractive dissociation are one of the dominant sources of uncertainty in interpretations of the mass composition. The uncertainty caused by these cross-section measurements should be reduced to less than ± 3.0 g/cm^2 to avoid effects on interpretations of mass composition.

Measurements of very forward photons produced from diffractive dissociation using ATLAS and LHCf detectors were discussed to reduce uncertainty in very low diffractive-mass events. Very low diffractive-mass events have not been measured by the ALICE and CMS experiments. In the measurements by the two experiments, these missed events were estimated by extrapolations using models. To reduce uncertainty, measurements of these missed events are crucial. In the previous study, the very forward photons produced in diffractive dissociation were measured by ATLAS and LHCf detectors. In this study, by adding signals from the minimum bias trigger scintillator of the ATLAS experiment, the SD fraction for the very forward photon sample was measured to be $0.477 \pm 0.019({\rm stat.})^{+0.013}_{-0.009}({\rm syst.(resp.)}) \pm 0.025({\rm syst.(bias)})$ for the photons in $\eta > 10.94$ selected by $N_{\rm charged} = 0$ for charged particles with $p_T > 100$ MeV/c^2 in $|\eta| < 2.5$. By applying the SD fraction, the energy spectrum of very forward photons produced in SD was measured.

We verified predictions by PYTHIA8 MBR using the energy spectrum measured above. The spectrum for photons in $\eta > 10.94$ from SD is sensitive to $\log_{10}\xi < -7.5$, whereas that for photons in $8.81 < \eta < 8.99$ is sensitive to $\log_{10}\xi > -7.5$. Therefore, we can validate predictions of very low diffractive-mass events if we rely on calculations of particle productions in the hadronic interaction model. Validation of PYTHIA8 MBR was performed by changing three parameters, ${\rm popcornRate}$, ϵ, and α'. Within the limitations of parameters

in PYTHIA8 MBR, we failed to reproduce the photon spectrum in $\eta > 10.94$ produced by SD, whereas other spectra were well reproduced with $\epsilon = 0.14$. This result suggests that the production of very low diffractive-mass events for SD in PYTHIA8 MBR is not enough, even if low diffractive-mass events are increased by the parameter ϵ. By contrast, EPOS-LHC shows good agreement with the measured spectra. These results suggest that uncertainty in cross-section measurements of SD and DD by the CMS experiment might be underestimated. By considering EPOS-LHC in estimation of the extrapolation uncertainty of the CMS result, the uncertainty in $\langle X_{\rm max} \rangle$ was estimated to be $^{+2.7}_{-1.2}$ g/cm^2.

Particle production mechanism in diffractive dissociation can be studied in future experiments. The uncertainty in particle productions makes it challenging to understand cross-sections of very low diffractive-mass events from the very forward photon spectrum measured by ATLAS and LHCf detectors. In future measurements using the ATLAS and LHCf detectors, we can measure a very forward photon spectrum for $\log_{10}\xi \approx 6$ with higher statistics. Moreover, very forward neutrons from diffractive dissociation can be measured by the ATLAS and LHCf detectors. These measurements will reduce modeling uncertainty in particle productions. By combining the photon spectra presented in this thesis and the results of future experiments, we can determine cross-sections for very low diffractive-mass events from very forward photon measurements. Finally, they will reduce uncertainty in cross-sections measurements of diffractive dissociation and uncertainty in $\langle X_{\rm max} \rangle$ coming from the uncertainty in experimental results.

Appendix A

LHCf-Arm1 response function

The LHCf-Arm1 response function was a function to emulate event selections adopted in Chap.6. Since the number of hits in detectors was only considered in Chap.6, this function categorizes events into two cases: the case that events passed the event selections and the case that events were rejected.

In event selections in Chap.6, most of the photons passed the selections, whereas parts of the photons were rejected and parts of the neutrons passed. Moreover, more than one particle is sometimes hit in a calorimeter tower (multi-hit). The multi-hit event was sometimes reconstructed as single-hit and passed the event selection, even though most events were reconstructed as multi-hit and rejected in the selection. Decay and transportation in the beam pipe were considered by the simulation using Cosmos-Epics interface [80]. In this response function, the events were categorized into three types based on the number of hits and particle types at the true level. The function for each type was applied for the events in each type. Three types were a photon hit in a calorimeter tower (single photon hit), a hadron hit in a calorimeter tower (single neutron hit), and more than one particle hit in a calorimeter tower (multi-hit).

In this function, reconstruction of hit position was emulated by the gaussian smearing. The reconstructed hit position and true position were evaluated in the full simulation. The difference between the two positions was fitted by the gaussian function. X and Y positions were considered separately. The mean and sigma of the fitted gaussian function were shown in Tab. A.1. The fitted gaussian function for each type and each axis was applied.

The detector response for the single-photon hit case was emulated by the efficiency function after the gaussian smearing of the hit position. The efficiency function emulates the

	X		Y	
	mean	sigma	mean	sigma
Small tower, photon	0.002010	0.050276	0.007811	0.050511
Large tower, photon	0.000397	0.062535	-0.006376	0.062718
Small tower, hadron	0.005961	0.109144	0.018548	0.103526
Large tower, hadron	-0.000501	0.173052	-0.018955	0.168093

Table A.1: Mean and sigma for the gaussian function to emulate hit position. The difference between true and reconstructed position was fitted by the gaussian function for each fiducial region and each particle type.

performance of the particle identification using the $L_{90\%}$ parameter and event selections by energy threshold. The efficiency of the particle identification using the $L_{90\%}$ parameter was roughly 90%. Sometimes, the reconstructed energy of photons above $200\ \mathrm{GeV}$ was calculated as less than $200\ \mathrm{GeV}$ at low energy. Therefore, the efficiency decreases for low energy. The efficiency evaluated for each fiducial region by full detector simulation was fitted by the following function,

$$f(x) = \frac{p_0}{1 - exp(-p_1 + p_2 E_\gamma)}, \tag{A.0.1}$$

where p_0, p_1, and p_2 were free parameters. E_γ is the energy of photon in the fiducial region. For region A, these parameters are $p_0 = 0.9047$, $p_1 = 0.0578$, and $p_2 = 214.6$. For region B, these parameters are $p_0 = 0.9033$, $p_1 = 0.0603$, and $p_2 = 216.2$. The fitted function was used as the efficiency function.

The detector response for the single neutron hit case was emulated by the efficiency function for single hit neutron. Most of the hadrons hit in a calorimeter tower were rejected by the particle identification. However, approximately 0.5% of hadrons passed this selection. Equation A.0.1 was also used for the single neutron hit. The energy of neutron was used instead of E_γ For region A, parameters are $p_0 = 0.0071$, $p_1 = 0.0131$, and $p_2 = 365.5$. For region B, parameters are $p_0 = 0.0056$, $p_1 = 0.1572$, and $p_2 = 345.2$.

Multi-hit events sometimes make signals similar to single-photon hit events. These cases were emulated by the multi-hit response function. In the reconstruction, the number of hits in a calorimeter tower was estimated from lateral distributions in GSO bar hodoscope layers. However, if two particles hit very closely or the energy of one particle was much larger than the others, signals in GSO bar hodoscopes were very similar with single-hit cases. These events were reconstructed as single-hit and passed the event selection. Moreover, because the calorimeter was 1.4 interaction lengths, if a photon and a hadron hit a calorimeter tower, hadron sometimes does not make signals in a calorimeter. Sometimes more than two particles hit a tower, whereas the probability for these events was very small. Thus, only two particles hit cases were considered in this function. The procedures of this function are as follows;

- **Two-photon hits**

  If the distance of hit positions between two photons was smaller than $3\ \mathrm{mm}$, the detector response was emulated using the function for the single-photon hit. If the energy of one of the photons was less than $200\ \mathrm{GeV}$, the hit position of the larger energy photon and the sum of photon energy was assumed in the function for the single-photon hit. If the energy of both photons is larger than $200\ \mathrm{GeV}$, the weighted average of hit position and sum of photon energy was assumed.

  If the distance of hit positions was larger than $3\ \mathrm{mm}$, the ratio of energy E_2/E_1, where E_1 and E_2 were the energy of the larger and smaller energy photon, respectively, was considered. If E_2/E_1 was smaller than 32% for the small tower and 18% for the large tower, the detector response was estimated using the function for the single-photon hit. The sum of energy of two photons and the hit position of the larger energy photon were considered in the function for the single-photon hit. If E_2/E_1 was larger than the threshold, the event was considered to be rejected by the single-hit selection in reconstruction.

- **A photon and a hadron hit**

If a hadron makes no interaction in the detector, the event was reconstructed as single-photon hit events. The rate of hadron events with no interaction was fixed to 32% of all hadron events in the function. The detector response was emulated using the function for the single-photon hit.

The performance of the LHCf-Arm1 response function was estimated using LHCf-Arm1 detector simulations. Performance was estimated for each type. The performance parameter κ was estimated as shown in Tab.6.6. We should note that the number of multi-hit events and single neutron hit events that pass the event selection is very small. Thus, the relatively worse performance of the function for multi-hit events does not affect the analysis.

References

[1] J. Linsley "Evidence for a Primary Cosmic-Ray Particle with Energy 10^{20} eV," Phys. Rev. Lett., Vol. 10 (1963) 146–148, February, DOI: 10.1103/PhysRevLett.10.146.

[2] M. Nagano and A. A. Watson "Observations and implications of the ultrahigh-energy cosmic rays," Rev. Mod. Phys., Vol. 72 (2000) 689–732, July, DOI: 10.1103/RevModPhys.72.689.

[3] R. U. Abbasi, M. Abe, T. Abu-Zayyad et al. "The Cosmic Ray Energy Spectrum between 2 PeV and 2 EeV Observed with the TALE Detector in Monocular Mode," The Astrophysical Journal, Vol. 865 (2018) 74, September, DOI: 10.3847/1538-4357/aada05.

[4] C. Jui "Summary of Results from the telescope Array Experiment," in *Proceedings of The 34th International Cosmic Ray Conference — PoS(ICRC2015)* 035, Trieste, Italy: Sissa Medialab, August (2016) , DOI: 10.22323/1.236.0035.

[5] R. Abbasi, M. Abe, T. Abu-Zayyad et al. "The energy spectrum of cosmic rays above $10^{17.2}$ eV measured by the fluorescence detectors of the Telescope Array experiment in seven years," Astroparticle Physics, Vol. 80 (2016) 131–140, July, DOI: 10.1016/j.astropartphys.2016.04.002.

[6] F. Fenu "The cosmic ray energy spectrum measured using the Pierre Auger Observatory," in *Proceedings of 35th International Cosmic Ray Conference — PoS(ICRC2017)* 486, Trieste, Italy: Sissa Medialab, August (2017) , DOI: 10.22323/1.301.0486.

[7] K. Greisen "END TO THE COSMIC-RAY SPECTRUM?" Phys. Rev. Lett., Vol. 16 (1966) 748–750.

[8] G. T. Zatsepin and V. A. Kuzmin "Upper Limit of the Spectrum of Cosmic Rays," JETP Lett., Vol. 4 (1966) 78–.

[9] K.-H. Kampert and M. Unger "Measurements of the cosmic ray composition with air shower experiments," Astroparticle Physics, Vol. 35 (2012) 660–678, DOI: 10.1016/j.astropartphys.2012.02.004.

[10] D. Allard, E. Parizot, and A. Olinto "On the transition from galactic to extra-galactic cosmic-rays: Spectral and composition features from two opposite scenarios," Astroparticle Physics, Vol. 27 (2007) 61-75, DOI: https://doi.org/10.1016/j.astropartphys.2006.09.006.

[11] D. Allard "Extragalactic propagation of ultrahigh energy cosmic-rays," Astroparticle Physics, Vol. 39-40 (2012) 33-43, DOI: https://doi.org/10.1016/j.astropartphys.2011.10.011, Cosmic Rays Topical Issue.

[12] E. G. Berezhko "Composition of cosmic rays accelerated in active galactic nuclei," Astrophysical Journal, Vol. 698 (2009) 138–141, DOI: 10.1088/0004-637X/698/2/L138.

[13] H. Tokuno, Y. Tameda, M. Takeda et al. "New air fluorescence detectors employed in the Telescope Array experiment," Nuclear Instruments and Methods in Physics Research, Section A: Accelerators, Spectrometers, Detectors and Associated Equipment, Vol. 676 (2012) 54–65, DOI: 10.1016/j.nima.2012.02.044.

[14] T. Abu-Zayyad, R. Aida, M. Allen et al. "The surface detector array of the Telescope Array experiment," Nuclear Instruments and Methods in Physics Research, Section A: Accelerators, Spectrometers, Detectors and Associated Equipment, Vol. 689 (2012) 87–97, DOI: 10.1016/j.nima.2012.05.079.

[15] A. Aab, P. Abreu, M. Aglietta et al. "The Pierre Auger Cosmic Ray Observatory," Nuclear Instruments and Methods in Physics Research, Section A: Accelerators, Spectrometers, Detectors and Associated Equipment, Vol. 798 (2015a) 172–213, DOI: 10.1016/j.nima.2015.06.058.

[16] A. Yushkov "Mass Composition of Cosmic Rays with Energies above $10^{17.2}$ eV from the Hybrid Data of the Pierre Auger Observatory," in *Proceedings of 36th International Cosmic Ray Conference — PoS(ICRC2019)* 482, Trieste, Italy: Sissa Medialab, August (2019) , DOI: 10.22323/1.358.0482.

[17] T. Pierog, I. Karpenko, J. M. Katzy, E. Yatsenko, and K. Werner "EPOS LHC: Test of collective hadronization with data measured at the CERN Large Hadron Collider," Physical Review C - Nuclear Physics, Vol. 92 (2015) 1–15, DOI: 10.1103/PhysRevC.92.034906.

[18] S. Ostapchenko "Monte Carlo treatment of hadronic interactions in enhanced Pomeron scheme: QGSJET-II model," Physical Review D - Particles, Fields, Gravitation and Cosmology, Vol. 83 (2011) 1–27, DOI: 10.1103/PhysRevD.83.014018.

[19] F. Riehn, H. Dembinski, R. Engel, A. Fedynitch, T. Gaisser, and T. Stanev "The hadronic interaction model Sibyll 2.3c and Feynman scaling," in *Proceedings of 35th International Cosmic Ray Conference —PoS(ICRC2017)* 301, Trieste, Italy: Sissa Medialab, August (2017) , DOI: 10.22323/1.301.0301.

[20] A. Aab, P. Abreu, M. Aglietta et al. "Depth of maximum of air-shower profiles at the Pierre Auger Observatory. I. Measurements at energies above $10^{17.8}$ eV," Phys. Rev. D, Vol. 90 (2014) 122005, December, DOI: 10.1103/PhysRevD.90.122005.

[21] S. Ostapchenko "QGSJET-II: towards reliable description of very high energy hadronic interactions," Nuclear Physics B - Proceedings Supplements, Vol. 151 (2006) 143–146, January, DOI: 10.1016/j.nuclphysbps.2005.07.026.

[22] A. Aab, P. Abreu, M. Aglietta et al. "Muons in air showers at the Pierre Auger Observatory: Mean number in highly inclined events," Phys. Rev. D, Vol. 91 (2015b) 032003, February, DOI: 10.1103/PhysRevD.91.032003.

[23] L. Cazon et al. "Working Group Report on the Combined Analysis of Muon Density Measurements from Eight Air Shower Experiments," in *Proceedings of 36th International Cosmic Ray Conference — PoS(ICRC2019)*: Sissa Medialab, August (2019) .

[24] K. Akiba, M. Akbiyik, M. Albrow et al. "LHC forward physics," Journal of Physics G: Nuclear and Particle Physics, Vol. 43 (2016) 110201, November, DOI: 10.1088/0954-3899/43/11/110201.

[25] T. Pierog "Connecting accelerator experiments and cosmic ray showers," EPJ Web of Conferences, Vol. 53 (2013) 01004, Jun, DOI: 10.1051/epjconf/20135301004.

[26] Tamás Csörgő, G. Antchev, P. Aspell et al. "Elastic Scattering and Total Cross-Section in p+p Reactions: As Measured by the LHC Experiment TOTEM at $\sqrt{}$ s = 7 TeV," Progress of Theoretical Physics Supplement, Vol. 193 (2012) 180-183, 03, DOI: 10.1143/PTPS.193.180.

[27] K. Werner, F.-M. Liu, and T. Pierog "Parton ladder splitting and the rapidity dependence of transverse momentum spectra in deuteron-gold collisions at the BNL Relativistic Heavy Ion Collider," Physical Review C, Vol. 74 (2006) 044902, October, DOI: 10.1103/PhysRevC.74.044902.

[28] V. Khachatryan, A. M. Sirunyan, A. Tumasyan et al. "Transverse-Momentum and Pseudorapidity Distributions of Charged Hadrons in pp Collisions at $\sqrt{s} = 7$ TeV," Phys. Rev. Lett., Vol. 105 (2010) 022002, July, DOI: 10.1103/PhysRevLett.105.022002.

[29] V. Khachatryan, A. M. Sirunyan, A. Tumasyan et al. "Measurement of diffractive dissociation cross sections in pp collisions at $\sqrt{}$ s =7 TeV," Physical Review D, Vol. 92 (2015) 012003, July, DOI: 10.1103/PhysRevD.92.012003.

[30] B. Abelev, J. Adam, D. Adamová et al. "Measurement of inelastic, single- and double-diffraction cross sections in proton − proton collisions at the LHC with ALICE," The European Physical Journal C, Vol. 73 (2013) 2456, Jun, DOI: 10.1140/epjc/s10052-013-2456-0.

[31] F. V. Riehn "Hadronic multiparticle production with Sibyll," Ph.D. dissertation, Karlsruhe (2015) , DOI: 10.5445/IR/1000052699.

[32] N. Amos, C. Avila, W. Baker et al. "Diffraction dissociation in collisions at $\sqrt{}$ s=1.8 TeV," Physics Letters B, Vol. 301 (1993) 313–316, March, DOI: 10.1016/0370-2693(93)90707-O.

[33] O. Adriani, E. Berti, L. Bonechi et al. "Measurement of energy flow, cross section and average inelasticity of forward neutrons produced in $\sqrt{s}$ = 13 TeV proton-proton collisions with the LHCf Arm2 detector," Journal of High Energy Physics, Vol. 2020 (2020) 16, July, DOI: 10.1007/JHEP07(2020)016.

[34] Y. Makino "Measurement of the very-forward photon production in 13 TeV proton-proton collisions at the LHC," Ph.D. dissertation (2017) , URL: https://cds.cern.ch/record/2266968.

[35] O. Adriani, E. Berti, L. Bonechi et al. "LHCf plan for proton-oxygen collisions at LHC," in *Proceedings of 37th International Cosmic Ray Conference — PoS(ICRC2021)* 348, Trieste, Italy: Sissa Medialab, July (2021) , DOI: 10.22323/1.395.0348.

[36] S. Ostapchenko "LHC data on inelastic diffraction and uncertainties in the predictions for longitudinal extensive air shower development," Physical Review D, Vol. 89 (2014) 074009, April, DOI: 10.1103/PhysRevD.89.074009.

[37] G. Aad, B. Abbott, J. Abdallah et al. "Rapidity gap cross sections measured with the ATLAS detector in pp collisions at $\sqrt{}$ s =7 TeV," European Physical Journal C, Vol. 72 (2012) 1926, DOI: 10.1140/epjc/s10052-012-1926-0.

[38] G. Antchev, P. Aspell, I. Atanassov et al. "Measurement of proton-proton inelastic scattering cross-section at $\sqrt{s} = 7\,\mathrm{TeV}$," EPL (Europhysics Letters), Vol. 101 (2013a) 21003, January, DOI: 10.1209/0295-5075/101/21003.

[39] L. B. Arbeletche, V. P. Gonçalves, and M. A. Müller "Investigating the influence of diffractive interactions on ultrahigh-energy extensive air showers," International Journal of Modern Physics A, Vol. 33 (2018) 1850153, September, DOI: 10.1142/S0217751X18501531.

[40] T. K. Gaisser, R. Engel, and E. Resconi *Cosmic Rays and Particle Physics*, Cambridge: Cambridge University Press (2016) , DOI: 10.1017/CBO9781139192194.

[41] R. Ulrich, R. Engel, and M. Unger "Hadronic multiparticle production at ultrahigh energies and extensive air showers," Physical Review D, Vol. 83 (2011) 054026, March, DOI: 10.1103/PhysRevD.83.054026.

[42] J. Matthews "A Heitler model of extensive air showers," Astroparticle Physics, Vol. 22 (2005) 387–397, DOI: 10.1016/j.astropartphys.2004.09.003.

[43] J. R. FORSHAW and D. A. ROSS *Quantum Chromodynamics and the Pomeron*: Cambridge University Press (1997) .

[44] R. K. Ellis, W. J. Stirling, and B. R. Webber *QCD and Collider Physics*: Cambridge University Press (2003) .

[45] G. Antchev, P. Aspell, I. Atanassov et al. "Measurement of proton-proton elastic scattering and total cross-section at $\sqrt{s} = 7\,TeV$," EPL (Europhysics Letters), Vol. 101 (2013b) 21002, January, DOI: 10.1209/0295-5075/101/21002.

[46] K. Goulianos "Diffractive interactions of hadrons at high energies," Physics Reports, Vol. 101 (1983) 169–219, December, DOI: 10.1016/0370-1573(83)90010-8.

[47] A. V. Barnes, D. J. Mellema, A. V. Tollestrup, R. L. Walker, O. I. Dahl, R. A. Johnson, R. W. Kenney, and M. Pripstein "Pion Charge-Exchange Scattering at High Energies," Physical Review Letters, Vol. 37 (1976) 76–79, July, DOI: 10.1103/PhysRevLett.37.76.

[48] L. Jenkovszky, R. Schicker, and I. Szanyi "Elastic and diffractive scattering in the LHC era," February, DOI: 10.1142/S0218301318300059.

[49] K. Ohashi, H. Menjo, Y. Itow, T. Sako, and K. Kasahara "Simulation study on the effects of diffractive collisions on the prediction of the observables in ultra-high-energy cosmic-ray experiments," Progress of Theoretical and Experimental Physics, Vol. 2021 (2021) 033F01, March, DOI: 10.1093/ptep/ptab013, Discussions related to the number of muons are shown in the version 1 in the preprint server only. You can find the version in the following page, https://arxiv.org/abs/2005.12594v1.

[50] T. Sjöstrand, S. Ask, J. R. Christiansen et al. "An introduction to PYTHIA 8.2," Computer Physics Communications, Vol. 191 (2015) 159–177, DOI: 10.1016/j.cpc.2015.01.024.

[51] A. Donnachie and P. Landshoff "Elastic scattering and diffraction dissociation," Nuclear Physics B, Vol. 244 (1984) 322–336, October, DOI: 10.1016/0550-3213(84)90315-8.

[52] R. CIESIELSKI "MBR Monte Carlo Simulation in PYTHIA8," in *Proceedings of 36th International Conference on High Energy Physics —PoS(ICHEP2012)*, Vol. 2012-July 301, Trieste, Italy: Sissa Medialab, August (2013) , DOI: 10.22323/1.174.0301.

[53] K. Goulianos "Diffraction in QCD," March, URL: http://arxiv.org/abs/hep-ph/0203141.

[54] F. Riehn, R. Engel, A. Fedynitch, T. K. Gaisser, and T. Stanev "Hadronic interaction model sibyll 2.3d and extensive air showers," Physical Review D, Vol. 102 (2020) 063002, September, DOI: 10.1103/PhysRevD.102.063002.

[55] M. L. Good and W. D. Walker "Diffraction Dissociation of Beam Particles," Physical Review, Vol. 120 (1960) 1857–1860, December, DOI: 10.1103/PhysRev.120.1857.

[56] R. Ulrich, T. Pierog, and C. Baus "Cosmic Ray Monte Carlo Package, CRMC," Zenodo (2021) , https://doi.org/10.5281/zenodo.4558705.

[57] R. Covolan, J. Montanha, and K. Goulianos "A new determination of the soft pomeron intercept," Physics Letters B, Vol. 389 (1996) 176-180, DOI: https://doi.org/10.1016/S0370-2693(96)01362-7.

[58] G. Aad, B. Abbott, D. C. Abbott et al. "Measurement of differential cross sections for single diffractive dissociation in $\sqrt{s} = 8$ TeV pp collisions using the ATLAS ALFA spectrometer," Journal of High Energy Physics, Vol. 2020 (2020) 042, DOI: 10.1007/JHEP02(2020)042.

[59] G. Antchev, P. Aspell, I. Atanassov et al. "Luminosity-independent measurements of total, elastic and inelastic cross-sections at $\sqrt{s} = 7$ TeV," EPL (Europhysics Letters), Vol. 101 (2013c) 21004, January, DOI: 10.1209/0295-5075/101/21004.

[60] G. Aad, B. Abbott, J. Abdallah et al. "Measurement of the total cross section from elastic scattering in pp collisions at $\sqrt{}$ s=7 TeV with the ATLAS detector," Nuclear Physics B, Vol. 889 (2014) 486–548, DOI: 10.1016/j.nuclphysb.2014.10.019.

[61] A. M. Sirunyan, A. Tumasyan, W. Adam et al. "Measurement of the inelastic proton-proton cross section at $\sqrt{s} = 13$ TeV," Journal of High Energy Physics, Vol. 2018 (2018) 161, July, DOI: 10.1007/JHEP07(2018)161.

[62] M. Aaboud, G. Aad, B. Abbott et al. "Measurement of the Inelastic Proton-Proton Cross Section at $\sqrt{}$ s=13 TeV with the ATLAS Detector at the LHC," Physical Review Letters, Vol. 117 (2016a) 182002, DOI: 10.1103/PhysRevLett.117.182002.

[63] G. Aad, B. Abbott, J. Abdallah et al. "Measurement of the inelastic proton − proton cross-section at $\sqrt{}$ s=7 TeV with the ATLAS detector," Nature Communications, Vol. 2 (2011) 463, September, DOI: 10.1038/ncomms1472.

[64] G. Antchev, P. Aspell, I. Atanassov et al. "First measurement of elastic, inelastic and total cross-section at $\sqrt{s} = 13$ TeV by TOTEM and overview of cross-section data at LHC energies," The European Physical Journal C, Vol. 79 (2019) 103, February, DOI: 10.1140/epjc/s10052-019-6567-0.

[65] M. Mallamaci et al. "Measurements of the depth of maximum muon production and of its fluctuations in extensive air showers above 1.5×10^{19} eV at the Pierre Auger Observatory," August, DOI: 10.22323/1.301.0509.

[66] T. Bergmann, R. Engel, D. Heck, N. N. Kalmykov, S. Ostapchenko, T. Pierog, T. Thouw, and K. Werner "One-dimensional hybrid approach to extensive air shower simulation," Astroparticle Physics, Vol. 26 (2007) 420–432, DOI: 10.1016/j.astropartphys.2006.08.005.

[67] S. A. Bass, M. Belkacem, M. Bleicher et al. "Microscopic Models for Ultrarelativistic Heavy Ion Collisions," Progress in Particle and Nuclear Physics, Vol. 41 (1998) 255–369, DOI: 10.1016/s0146-6410(98)00058-1.

[68] M. Bleicher, E. Zabrodin, C. Spieles et al. "Relativistic hadron-hadron collisions in the ultra-relativistic quantum molecular dynamics model," Journal of Physics G: Nuclear and Particle Physics, Vol. 25 (1999) 1859–1896, September, DOI: 10.1088/0954-3899/25/9/308.

[69] T. K. Gaisser and A. M. Hillas "Reliability of the Method of Constant Intensity Cuts for Reconstructing the Average Development of Vertical Showers," in *Proceedings of 15th International Cosmic Ray Conference* (1977) .

[70] C. Meurer, J. Blümer, R. Engel, A. Haungs, and M. Roth "Muon production in extensive air showers and its relation to hadronic interactions," Czechoslovak Journal of Physics, Vol. 56 (2006) A211–A219, September, DOI: 10.1007/s10582-006-0156-9.

[71] S. Ostapchenko and M. Bleicher "Constraining pion interactions at very high energies by cosmic ray data," Physical Review D, Vol. 93 (2016) 051501, March, DOI: 10.1103/PhysRevD.93.051501.

[72] "Measurement of contributions of diffractive processes to forward photon spectra in pp collisions at $\sqrt{}$ s = 13 TeV,"Technical report, CERN, Geneva (2017) , URL: https://cds.cern.ch/record/2291387.

[73] O. Adriani, E. Berti, L. Bonechi et al. "Measurement of forward photon production cross-section in proton − proton collisions at $\sqrt{s} = 13\,\mathrm{TeV}$ with the LHCf detector," Physics Letters B, Vol. 780 (2018) 233–239, May, DOI: 10.1016/j.physletb.2017.12.050.

[74] G. Aad, E. Abat, J. Abdallah et al. "The ATLAS Experiment at the CERN Large Hadron Collider," Journal of Instrumentation, Vol. 3 (2008) S08003–S08003, August, DOI: 10.1088/1748-0221/3/08/S08003.

[75] O. Adriani, L. Bonechi, M. Bongi et al. "The lhcf detector at the cern large hadron collider," Journal of Instrumentation, Vol. 3 (2008) , DOI: 10.1088/1748-0221/3/08/S08006.

[76] A. Sidoti "Minimum bias trigger scintillators in ATLAS run II," Journal of Instrumentation, Vol. 9 (2014) , DOI: 10.1088/1748-0221/9/10/C10020.

[77] Y. Makino, A. Tiberio, O. Adriani et al. "Performance study for the photon measurements of the upgraded LHCf calorimeters with Gd2SiO5 (GSO) scintillators," Journal of Instrumentation, Vol. 12 (2017) , DOI: 10.1088/1748-0221/12/03/P03023.

[78] Q.-d. Zhou "Study of contributions of diffractive processes to forward neutral particle production in p-p collisions at $\sqrt{s}$ = 13 TeV with the ATLAS-LHCf detector.," Ph.D. dissertation (2018) , URL: https://cds.cern.ch/record/2306650, Presented 22 Feb 2018.

[79] T. Sjöstrand, L. Lönnblad, S. Mrenna, and P. Skands "PYTHIA 6.3 Physics and Manual," URL: http://arxiv.org/abs/hep-ph/0308153.

[80] K. Kasahara https://cosmos.n.kanagawa-u.ac.jp/EPICSHome/index.html (Accessed 20 Oct 2021) .

[81] J. Ranft "Dual parton model at cosmic ray energies," Physical Review D, Vol. 51 (1995) 64–84, January, DOI: 10.1103/PhysRevD.51.64.

[82] S. Agostinelli, J. Allison, K. Amako et al. "Geant4—a simulation toolkit," Nuclear Instruments and Methods in Physics Research Section A: Accelerators, Spectrometers, Detectors and Associated Equipment, Vol. 506 (2003) 250–303, July, DOI: 10.1016/S0168-9002(03)01368-8.

[83] The ATLAS Collaboration, G. Aad, B. Abbott et al. *The ATLAS Simulation Infrastructure*, Vol. 70 823–874 (2010) , DOI: 10.1140/epjc/s10052-010-1429-9.

[84] M. Aaboud, G. Aad, B. Abbott et al. "Charged-particle distributions at low transverse momentum in $\sqrt{}$ s=13 TeV pp interactions measured with the ATLAS detector at the LHC," European Physical Journal C, Vol. 76 (2016b) 502, DOI: 10.1140/epjc/s10052-016-4335-y.

[85] O. ADRIANI, L. BONECHI, M. BONGI et al. "LHCf DETECTOR PERFORMANCE DURING THE 2009 – 2010 LHC RUN," International Journal of Modern Physics A, Vol. 28 (2013) 1330036, DOI: 10.1142/S0217751X13300366.

[86] L. Tompkins "Performance of the ATLAS Minimum Bias Trigger in pp collisions at the LHC,"Technical report (2010) , URL: https://cds.cern.ch/record/1296152.

[87] B. Andersson, G. Gustafson, and T. Sjöstrand "Baryon Production in Jet Fragmentation and γ-Decay," Physica Scripta, Vol. 32 (1985) 574–580, December, DOI: 10.1088/0031-8949/32/6/003.

[88] C. Bierlich, A. Buckley, J. Butterworth et al. "Robust Independent Validation of Experiment and Theory: Rivet version 3," SciPost Physics, Vol. 8 (2020) 026, February, DOI: 10.21468/SciPostPhys.8.2.026.